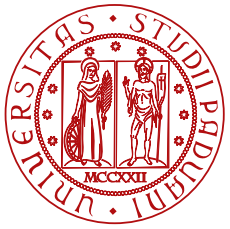

Università degli Studi di Padova

Dipartimento di Fisica e Astronomia Galileo Galilei

Master Thesis in Astrophysics and Cosmology

Observational biases in SEL metallicity measurements of extragalactic H II regions

Master Candidate

Carla Tovo

Student ID 2045250

Supervisor

Prof. Stefano Ciroi

University of Padova

Co-supervisor

Dott. Enrico Congiu

European Southern Observatory

Academic Year
2023/2024

To my boyfriend,
whose birthday appeared in the name of the randomly selected test galaxy—
because the universe knows how much I love you.

Abstract

Measuring the chemical composition of the ISM in galaxies holds significant importance in astrophysics, as it influences stellar, galaxy, and cosmological evolution. According to the baryon cycle, the abundance of heavy elements should consistently rise over cosmic time, linking the metallicity of a galaxy to its evolutionary stage. Indeed, researchers have identified several relationships between metallicity and other galaxies' parameters, such as mass and luminosity. We are reaching the moment where inaccurate metallicity measurements are becoming the limiting factors in extragalactic studies, in particular when comparing observations with simulations. Our study aims to investigate potential observational biases in the strong emission line methods used to estimate metallicities in nearby galaxies, focusing our attention on estimating the relevance of the DIG contamination and the influence of the aperture's size in the computation.

Contents

1

Introduction

Measuring the chemical composition of the Interstellar Medium (ISM) in galaxies is fundamental to understand stellar, galaxy, and cosmological evolution. According to the baryon cycle, galaxies process the ISM gas, condensing it into stars that synthesize heavier elements from hydrogen and helium. Subsequently, these elements are released back into the ISM through stellar winds and supernova explosions.

Theoretically, the abundance of elements heavier than Helium (typically referred to as "metals") should consistently rise over cosmic time. This trend hinges on factors such as the efficiency of gas-to-star conversion and the dynamics of gas interaction within systems, encompassing processes of accretion, enrichment, recycling, and ejection.

Given these intricacies, researchers have explored diverse relationships between the abundance of metals (also known as "metallicity") and other parameters, such as mass and luminosity, within the literature (e.g., Larson, 1974; Lequeux et al., 1979; Tremonti et al., 2004; Dalcanton et al., 2004; Dalcanton, 2007; Köppen et al., 2007; Finlator & Davé, 2008; Zahid et al., 2014, to just name a few of the many studies). These studies not only demonstrate the correlation between metallicity and the evolutionary stage of galaxies — with higher metallicities typically observed in more evolved galaxies — but also reveal spatial dependencies. Notably, galaxies exhibit abundance gradients, with metallicity decreasing farther from the center, which represents the oldest and densest region of the galaxy (Searle, 1971; Cioni, 2009; Haschke et al., 2012; Pilyugin et al., 2015). Moreover, recently more subtle, azimuthal metallicity variations

have been detected in some nearby systems (Sánchez-Menguiano et al., 2016; Vogt et al., 2017; Ho et al., 2017, 2018; Kreckel et al., 2019). These properties offer insights into the evolutionary trajectories of galaxies. Therefore, obtaining precise measurements of the ISM chemical composition is critical to identify and understand them.

Metallicity is typically expressed using the ratio of oxygen to hydrogen atoms, being oxygen one of the most common "metals" in the universe, and it can be measured using different approaches, each with its own advantages and limitations.

In this work, we will focus on the metallicity derived through Strong Emission Lines (SELs) Methods, which will be discussed in detail in Section 2. In particular, we investigate potential observational biases associated with the SELs method when used to compute metallicities in nearby galaxies using single H II regions as a proxy.

1.1 The ISM Structure

The ISM refers to the matter and radiation that exist in the space between star systems within a galaxy. This medium is composed primarily of gas, with small amounts of dust particles and cosmic rays interspersed throughout. The gas component is dominated by hydrogen, which constitutes the majority of the ISM's mass. Helium, the second most abundant element, typically accounts for about 10% of the hydrogen abundance. Trace amounts of heavier elements, such as carbon, nitrogen, and oxygen, are also present, with fractional abundances relative to hydrogen of approximately 4×10^{-4}, 9×10^{-5}, and 7×10^{-4}, respectively (Herbst, 1995).

The ISM exists in different phases, distinguished primarily by their physical state (atomic, molecular, or ionized), temperature, and density.

Atomic Gas Phase

The atomic gas phase of the ISM is largely composed of neutral hydrogen (HI) and traces of other elements in atomic form. This phase is further divided into cold and warm components.

- **Cold Neutral Medium (CNM)**: The CNM consists of atomic hydrogen at temperatures around 100 K, with densities typically ranging from 10

to 100 particles per cubic centimeter. This phase can partially obscure background starlight, particularly in the ultraviolet (UV) and optical wavelengths, where it produces absorption lines. Most of a galaxy's gas reservoir is found in this form (Carilli & Walter, 2013).

- **Warm Neutral Medium (WNM)**: The WNM exists at higher temperatures, around 10^4 K, and has lower densities, typically between 0.1 and 1 particle per cubic centimeter (Draine, 2011). The WNM is more diffuse and generally transparent to most wavelengths of light, although it can still contribute to absorption in the UV range.

Molecular Gas Phase

The molecular gas phase is predominantly composed of molecular hydrogen (H_2), along with trace molecules such as carbon monoxide (CO). This phase is found in the densest and coldest regions of the ISM.

- **Cold Molecular Medium (CMM)**: The CMM is characterized by temperatures as low as 10-20 K and high densities, often exceeding 10^2 particles per cubic centimeter. These regions are typically found in giant molecular clouds (GMCs) and are heavily obscured in optical wavelengths due to the high concentration of dust. However, they are observable in the infrared and radio wavelengths, where molecular emission lines are prominent (Ferrière, 2001).

Ionized Gas Phase

The ionized gas phase of the ISM is composed of ionized hydrogen (HII) and other elements in various stages of ionization. This phase is subdivided based on temperature:

- **Warm Ionized Medium (WIM)**: The WIM exists at temperatures around 10^4 K and densities ranging from 0.01 to 1 particle per cubic centimeter. This phase is often found in H II regions, which are associated with regions of active star formation and are illuminated by the UV radiation from young, hot stars. The WIM is a significant source of emission lines across a wide range of wavelengths, particularly in the optical and UV (Haffner et al., 2009).

- **Hot Ionized Medium (HIM)**: The HIM is found at temperatures of approximately 10^6 K, with much lower densities, typically around 10^{-4} particles per cubic centimeter. This phase is primarily heated by supernova explosions, which inject energy into the ISM, creating large cavities filled with hot, ionized gas. The HIM is best observed in the X-ray spectrum, where it contributes to the diffuse X-ray background (McKee & Ostriker, 1977).

The distribution of these phases within the ISM is highly non-uniform. Atomic and molecular gas represent the majority of the gas in a galaxy. The molecular gas typically is located on a thin disk, where it forms the raw material of the star formation, while the atomic one is distributed on a thicker and larger disk, serving mostly as a reservoir of material. In contrast, ionized gas is more diffusely distributed and is found both in star-forming regions and throughout the galactic halo.

Among the various phases of ISM gas, the warm photoionized gas is the most frequently studied for analyzing the chemical composition of the ISM. This preference arises from its distinct emission spectrum, which is dominated by strong recombination and forbidden lines, facilitating reliable chemical abundance measurements. The photoionization processes that govern this gas phase are well-understood, allowing for accurate modeling and interpretation of observational data (Osterbrock & Ferland, 2006). If possible, the chemical abundance of ionized gas is measured using specific type of gas structures: H II regions and Planetary Nebulae (PNe).

1.1.1 H II Regions

H II regions are vast clouds of gas that have been photoionized by the intense UV radiation emitted by hot, massive stars. These regions are associated with areas of recent massive star formation, where one or more O-type or B-type stars have formed. The energetic photons from these stars ionize the surrounding gas (mostly hydrogen), stripping electrons from the atoms and producing a characteristic emission spectrum. This process creates a glowing region of ionized gas that can be observed across various wavelengths, particularly in the optical and radio bands (Spitzer, 1978; Osterbrock & Ferland, 2006).

The size and morphology of H II regions vary significantly, depending on the number and distribution of the ionizing stars, as well as the properties of the surrounding ISM. It is possible to find compact regions with radii as small

as 1 parsec, often referred to as ultra-compact H II regions, as well as giant H II regions that can extend beyond 100 parsecs in radius (Churchwell, 2002; McKee & Ostriker, 2007). Ultra-compact H II regions are typically found within dense molecular clouds and are associated with very young, still-forming stars, while giant H II regions can encompass entire star-forming complexes and are often associated with older stellar populations.

The gas density in H II regions also spans a wide range, from approximately 10^4 particles per cubic centimeter in ultra-compact H II regions to around 10^2 particles per cubic centimeter in giant H II regions. The lower density observed in larger H II regions is often attributed to the inclusion of diffuse material within these regions, which lowers the average density of the cloud. Additionally, the expansion of the ionized gas into the surrounding ISM contributes to the decreasing density as the region evolves (Garay & Lizano, 1999).

H II regions frequently exhibit clumpy and filamentary appearances, a reflection of the turbulent and inhomogeneous nature of their parent molecular clouds. These complex structures, often highlighted by bright rims and dark pillars, are shaped by the interaction between the ionizing radiation and the surrounding dense gas (Peters et al., 2010; Dale, 2015).

1.1.2 Planetary Nebulae (PNe)

PNe represent a distinct type of emission nebula, formed during the late evolutionary stages of intermediate-mass stars (typically 1-8 solar masses). As these stars exhaust the nuclear fuel in their cores, they evolve off the Asymptotic Giant Branch (AGB) and shed their outer layers into space, creating an expanding shell of ionized gas. This material, enriched with elements such as carbon, nitrogen, and oxygen, is ionized by the intense UV radiation from the hot remnant core of the star, which eventually becomes a white dwarf.

The ionizing source of PNe, a hot white dwarf with surface temperatures ranging from 30,000 K to over 100,000 K, plays a crucial role in determining the morphology and structure of the nebula. The temperatures of these central stars are much higher than those found in H II regions, where the ionizing stars usually range between 20,000 K and 50,000 K. This higher temperature in PNe results in a higher degree of ionization within the nebula, allowing for the ionization of heavy elements to higher states. Consequently, PNe often exhibit stronger and more varied emission lines, including prominent lines from highly

ionized species like doubly or triply ionized oxygen ([O III]), nitrogen ([N II]), and neon ([Ne III]), which reflect the presence of higher energy photons emitted by the central white dwarf (Osterbrock & Ferland, 2006). This ionization structure provides key insights into the physical conditions within the nebula, such as electron temperatures and densities, and can be used to infer the chemical abundances of the progenitor star.

The size of planetary nebulae is much smaller than that of H II regions, with typical radii not exceeding 1 parsec. As PNe evolve, their densities gradually decrease over time due to the expansion of the gas envelope. The brightest PNe, observed in the early stages of their evolution, exhibit relatively high densities, ranging from approximately 10^3 to 10^5 particles per cubic centimeter. These high-density PNe are compact and show strong emission lines in their spectra, making them prominent objects in astrophysical studies.

As the nebula expands and the central star cools, the density of the gas decreases, and the nebula becomes more diffuse. Fainter PNe, observed in later stages of evolution, possess lower densities, sometimes dropping below 10^2 particles per cubic centimeter. This decrease in density correlates with a corresponding decline in brightness, making older PNe more challenging to detect and study. In any case, PNe provide valuable insights into the processes of stellar evolution, nucleosynthesis, and the chemical enrichment of galaxies.

PNe are also important tracers of the chemical composition and history of their host galaxies. The elemental abundances measured in PNe can reveal information about the original composition of the progenitor stars and the processes that occurred during their lifetimes. By studying PNe in different environments, such as the Milky Way, dwarf galaxies, and globular clusters, astronomers can gain a better understanding of the chemical evolution of galaxies and the distribution of elements in the universe (Stasińska, 2004).

This concise overview of the two distinct types of ionized gas reveals several important aspects. Firstly, it underscores that the ionization mechanisms operating in both types of regions are fundamentally the same, leading to the generation of characteristic emission spectra. Consequently, similar analytical techniques can be applied to study both types of ionized gas regions.

Secondly, it highlights that these two categories of nebulae provide insights into different aspects of the ISM. H II regions offer a window into the physical conditions of the gas during the formation of massive stars, offering valuable

data about the early stages of stellar evolution. In contrast, PNe offer a glimpse into the chemical composition of gas that has been altered by the processes within a star and subsequently expelled into space.

1.2 Expressing the Metallicity

Various methods are employed to report metal abundances, depending on the specific object under study and the tradition of the field.

1.2.1 Mass fraction

Commonly applied in studies of stellar composition, the **mass fraction** is a fundamental concept that characterizes stellar compositions by delineating the proportions of various elements. It is defined by three key parameters: X, representing the mass fraction of hydrogen; Y, the mass fraction of helium; and Z, the mass fraction of metals. Thus, these parameters adhere to the following equation

$$X + Y + Z = 1 \tag{1.1}$$

The hydrogen and the helium mass fractions are generally expressed as follows

$$X \equiv \frac{m_H}{M}; \quad Y \equiv \frac{m_{He}}{M} \tag{1.2}$$

where M is the total mass of the system, and m_H and m_{He} are, respectively, the mass of hydrogen and helium that the system contains. The value of Z is then calculated from equation 1.1 as

$$Z = \sum_{e>He} \frac{m_e}{M} = 1 - X - Y \tag{1.3}$$

1.2.2 Chemical abundance ratios

Another important metallicity indicator is the ratio

$$\left[\frac{Me}{H}\right] = log_{10}\left(\frac{N_{Me}}{N_H}\right)_\star - log_{10}\left(\frac{N_{Me}}{N_H}\right)_\odot \tag{1.4}$$

which indicates the logarithmic ratio of a star's metal abundance in comparison to that of the Sun. This logarithmic scale provides a standardized measure: stars with higher metallicity than the Sun exhibit positive values, indicating an abundance of metals beyond solar levels, whereas those with lower metallicity display negative values, suggesting a dominance of hydrogen and helium.

Traditionally, iron (Fe) serves as the primary reference element for determining metallicity due to its abundance in stellar spectra and the multitude of spectral lines it presents. Another alternative is oxygen, given its status as the most abundant heavy element.

1.2.3 Logarithmic abundance scale

Other than the forms already explained, in most astrophysical disciplines, elemental abundances are expressed using the traditional astronomical logarithmic abundance scale. Hydrogen is universally used as the reference element in spectroscopy. This choice is natural because hydrogen is the most abundant element in the universe and plays a crucial role in providing continuous opacity in the optical and infrared regions of the spectrum through the negative hydrogen ion (H^-) (Asplund et al., 2021).

The logarithmic abundance of an element X, denoted as $\log \epsilon(X)$, is normalized relative to hydrogen and is defined by the equation:

$$\log \epsilon(X) \equiv \log \left(\frac{N_X}{N_H}\right) + 12.00 \tag{1.5}$$

where N_X and N_H represent the number densities of element X and hydrogen, respectively. The constant value of +12.00 was historically chosen to ensure that the logarithmic abundance of hydrogen is exactly 12.00, thereby avoiding negative values for elemental abundances in the Sun (Goldberg et al., 1960).

2

The problem of the abundance determinations in H II regions

Young, massive, and hot stars, which predominantly fall within spectral types O and B, are known to emit an intense UV radiation field that permeate the surrounding ISM. The photons of this radiation field can interact with the atoms of the surrounding gas (mostly hydrogen), providing enough energy to (photo)ionize them and forming, therefore, an H II region. The electron produced by the ionization process can then interact with neighboring atoms or ions within the H II region, leading to the collisional excitation of bound metallic electrons into metastable[1] states. The subsequent decay of these excited states back to their ground states is accompanied by the emission of photons in specific emission lines, often called "Collisionally Excited Lines" (CELs). Electrons can also recombine with the many hydrogen atoms in the gas, producing the so called "Recombination Lines" (RLs). Ratios between forbidden or recombination lines, which can be observed and measured spectroscopically, serves as a diagnostic tool for determining physical conditions and chemical composition of the ionized gas.

The modeling of the emission spectra from H II regions is facilitated by

[1]Metastable states are energy levels in atoms or molecules that cannot be excited by photon absorption due to electric dipole selection rules. As a result, the transitions from these metastable states are often referred to as "forbidden lines", since they occur through mechanisms other than electric dipole transitions, such as magnetic dipole or electric quadrupole transitions.

the low electron density. As a consequence, H II regions are optically thin for optical transitions, which ensures that the emitted photons can escape the region without being reabsorbed or scattered, thereby preserving the information on the physical conditions of the emitting gas.

In this work, we will be focusing in particular on estimating the metallicity of the gas. There are three methods that have been traditionally employed in the literature to estimate the metallicity of photoionized gas within H II regions (Stasińska, 2004; Blanc et al., 2015):

- The Direct Method, which relies on the measurement of electron temperatures and densities to directly calculate abundances.
- The RLs Method, which estimates abundances from the ratio of metals and Hydrogen RLs.
- The SELs Method, which involves using empirical or theoretical calibrations of SELs ratios to infer metallicities.

2.1 The Direct Method

In the **Direct Method**, the metallicity is determined by analyzing the observed intensity ratio between metals' CELs and hydrogen RLs. These lines ratios are corrected for the temperature and density of the gas, since the emissivity, in particular the one of the CELs, is sensitive to both. For instance, in the case of O^{++}/H^{+}, the abundance ratio can be derived from

$$\frac{O^{++}}{H^{+}} = \frac{[\text{O III}]\ \lambda 5007/H\beta}{j_{[\text{O III}](T_e,n_e)}/j_{H\beta(T_e)}} \tag{2.1}$$

where, $j_{[\text{O III}](T_e,n)}$ represents the temperature (T_e) and density (n_e) dependent emission coefficient associated with the [O III] λ5007 line. In contrast, $j_{H\beta(T_e)}$, the emission coefficient for the $H\beta$ line, weakly depends only on T_e.

Therefore, precise measurements of both T_e and n_e are essential to estimate metallicities via the Direct Method. T_e is derived from the ratios of auroral and nebular CELs emitted by the same ion, which exhibit distinct excitation potentials and thus are sensitive to temperature changes. The [O III] λ4363/[O III] λ5007 ratio is the most common temperature sensitive ratio, since it involves relatively bright lines, although alternative ratios like [N II] λ5755/[N II] λ6584

or [S III] λ6312/[S III] λ9532 can also be used. At the same time, density can be inferred from intensity ratios of lines within the same ion possessing identical excitation energies but different collisional de-excitation rates. Prominent examples in the optical range include the [S II] λ6731/[S II] λ6717 and [O II] λ3726/[O II] λ3729 ratios (Osterbrock & Ferland, 2006).

A single line ratio determines only the abundance of a specific ion. To obtain the abundance of a particular element relative to hydrogen, the abundances of all its ions need to be summed. In practice, however, not all ions present in a nebula are observed. An exception to this is oxygen, which can be readily determined in H II regions through[2]:

$$\frac{O}{H} = \frac{O^+}{H^+} + \frac{O^{++}}{H^+} \tag{2.2}$$

In all other cases, adjustments for undetected ions are essential to accurately determine the elemental abundance. These adjustments are made through the application of Ionization Correction Factors (ICFs). In this case, the equation for determining the abundance ratio of element X relative to hydrogen H is given by:

$$\frac{X}{H} = \sum_{obs} \frac{X^{+i}}{H^+} \times ICF \tag{2.3}$$

In this equation, $\sum_{obs}$ represents the sum of all ionic abundances of the element X that can be directly observed.

Despite inherent uncertainties, ICFs often yield more accurate abundance than the simple sum of ionic abundances obtained from different techniques. In the 1970s and 1980s, a common approach to deriving these ICFs involved relying on considerations of ionization potentials and similarities between them. This method led to the development of simple expressions that are still commonly

[2]The presence of neutral oxygen (O^0) should not be included in the determination of oxygen abundance. This is because the reference hydrogen line used in such calculations is emitted by ionized hydrogen (H^+), while neutral oxygen (O^0) is associated with neutral hydrogen (H^0). Including O^0 would lead to an inaccurate abundance measurement, as it reflects a different ionization state that is not directly comparable to H^+. Therefore, only ionized oxygen should be considered when determining oxygen abundance (Stasińska, 2004).

used today (Stasińska, 2004; Delgado-Inglada et al., 2019):

$$\frac{N}{O} = \frac{N^+}{O^+} \tag{2.4}$$

$$\frac{Ne}{O} = \frac{Ne^{++}}{O^{++}} \tag{2.5}$$

$$\frac{C}{O} = \frac{C^{++}}{O^{++}} \tag{2.6}$$

$$\frac{S}{O} = \frac{(S^+S^{++})}{O^+} \tag{2.7}$$

The ionization potentials of N^+, Ne^{++}, and S^{++} are 29.6 eV, 63.4 eV, and 34.8 eV, respectively, while those of O^+ and O^{++} are 35.1 eV and 54.9 eV, respectively. The similarity in ionization potentials between pairs such as N^+ and O^+, Ne^{++} and O^{++}, and S^{++} and O^+ has historically been used to justify these simple ICFs expressions. However, advances in photoionization modeling have shown that these simplistic relations do not always hold true, particularly under varying nebular conditions. As a result, ICFs derived from grids of photoionization models are now considered more reliable. These models take into account the complexities of ionization structures within nebulae, leading to more accurate abundance determinations. Several sets of ICFs specifically for H II regions have been published in recent decades. Notable contributions include those by Mathis and Rosa (1991), Gruenwald and Viegas (1992), Izotov et al. (2006), Dors et al. (2016), Delgado-Inglada et al. (2019), and Amayo et al. (2021).

Direct methods for determining metallicity in galaxies face two significant limitations. Firstly, temperature-sensitive auroral lines are inherently faint, typically about 100 times fainter than their nebular counterparts. This faintness makes them particularly difficult to observe in distant galaxies. However, the recent advent of the James Webb Space Telescope (JWST) is beginning to shift this paradigm. Recent studies, such as those by Curti et al. (2023, 2024), have successfully used JWST data to measure metallicities using Direct Methods, marking a significant advancement in this field. Secondly, the strength of the auroral lines directly depends on the metallicity. As metallicity increases, these lines become fainter, making them increasingly difficult to detect.

Additionally, the accuracy of Direct Methods for determining abundances in nebulae is particularly sensitive to temperature fluctuations within these regions. If these fluctuations are not adequately accounted for, they can result in significant underestimations of the true abundance values. This challenge has

been well-documented in the literature, with early studies by Peimbert (1967) and Peimbert and Costero (1969). More recently, this topic has continued to receive attention, as evidenced by the work of Méndez-Delgado et al. (2023a), who further emphasizes the importance of accounting for temperature variations to ensure accurate abundance measurements. Regardless of these various issues, the Direct Method is still considered by the community as the "gold standard" for estimating metallicities.

2.2 The Recombination Line (RL) Method

Unlike CELs, metals' RLs emissivities exhibit only a subtle dependence on both T_e and n_e, with their intensities relative to hydrogen RLs scaling almost directly with the ionic abundance. As a consequence, the RLs Method is less susceptible to biases arising from temperature. Therefore, to determine total elemental abundances using this method, an ionization correction for unobserved ions remains necessary.

This direct scaling with abundance results in extremely faint lines for metals. If auroral lines are $\sim$ 100 times fainter than their nebular counterparts, metals RLs are typically 10000 times fainter than hydrogen RLs. Consequently, RLs abundance measurements demand exceptionally high Signal-to-Noise (S/N) ratios and high-resolution spectra. For this reason, the RLs Method have been typically applied mostly to Galactic H II regions or in galaxies of the local group.

For decades, it has been observed that RLs in PNe and H II regions indicate higher abundances compared to CELs. Typically, RLs abundances exceed CELs abundances by a factor of approximately 2 across most regions (see Liu, 2002; García-Rojas & Esteban, 2007), with the discrepancies observed for individual elements, such as C, N, O, and Ne, that show approximately the same magnitude. This disparity in abundances is quantified using the so-called Abundance Discrepancy Factor (ADF), defined as:

$$ADF(X^{+i}) = \frac{(X^{+i}/H^{+})_{RLs}}{(X^{+i}/H^{+})_{CELs}} \tag{2.8}$$

The explanations most often invoked for this discrepancy are varied:

i) temperature fluctuations

ii) incorrect atomic data

iii) fluorescent excitation

iv) upward bias in the measurements of weak line intensities

v) blending with other lines

vi) abundance inhomogeneities

The advent of high quantum efficiency, large dynamic range, and large format CCDs now enables the acquisition of high-quality measurements of many faint recombination lines. Consequently, hypothesis iv) regarding the upward bias in weak line intensity measurements can no longer be invoked. With a plethora of faint recombination lines now being accurately measured, the observed relative intensities of permitted transitions from highly ionized ions such as C^{++}, N^{++}, O^{++}, and Ne^{++} are consistent with the predictions of recombination theory. This finding contradicts hypotheses ii), iii), iv), and v).

Simultaneously, the temperature inhomogeneities for each ion, characterized by a particle density N_i within the gas, are quantified by t^2, as proposed by Peimbert (1967):

$$t^2(N_i) = \frac{\int (T_e - T_0(N_i))^2 N_i n_e dV}{T_0(N_i)^2 \int N_i n_e dV} \tag{2.9}$$

where T_e and n_e represent the electron temperature and density, respectively, at a given volume of the nebula, while T_0 denotes the average temperature of the gas, given by:

$$T_0(N_i) = \frac{\int T_e N_i n_e dV}{\int N_i n_e dV} \tag{2.10}$$

In the context of the temperature fluctuation scheme from Peimbert (1967), a value of $t^2 \sim 0.04$ results in an underestimation of metallicity by ~ 0.3 dex. Comparisons of temperature measurements obtained through different methods have consistently shown that temperature fluctuations are common in nebulae, with typical values of t^2 ranging from 0.03 to 0.05 (Stasińska, 1998; Mathis et al., 1998).

These findings suggest that the observed temperature fluctuations are a widespread phenomenon. However, these values of t^2, derived from the [O III] λ4363/[O III] λ5007 ratio and the Balmer jump, are insufficient to explain the higher metallicities derived from RLs. Thus, hypothesis i) regarding temperature fluctuations does not appear to provide a satisfactory explanation either.

Moreover, studies suggest the presence of clumps within the nebulae, characterized by a He/H ratio of 0.4 and elevated abundances of elements such as C, N, O, and Ne, possibly around 400 times higher than those in the diffuse gas (Liu et al., 2000, favours this hypothesis for the case of NGC 6153). A photoionization model incorporating components of different chemical compositions can been constructed to reproduce the observed integrated line ratios satisfactorily (Péquignot et al., 2002). However, reconciling such a model with current theories of element production in intermediate mass stars proves challenging, thus also discounting option vi). Méndez-Delgado et al. (2023b) recently provided general observational evidence supporting the t^2 dependence of the ADF, marking a significant advancement in the field. However, discussions regarding this topic remain ongoing.

2.3 The Strong Emission Lines (SELs) Method

When the electron temperature cannot be determined, for example, due to incomplete observational coverage of the required spectral range or the inability to detect temperature-sensitive lines (such as in the case of faint and distant nebulae), researchers must rely solely on the bright CELs and Balmer lines (collectively known as SELs) as abundance diagnostics. The method, pioneered by Pagel et al. (1979), aims to establish a relationship between the abundance of oxygen, used as a tracer of the general abundance of the ionized gas in an H II region, and a combination of ratios of SELs. This relationship is commonly termed a "calibration" and is essential for converting metallicity-sensitive emission-line ratios into reliable metallicity estimators.

Two distinct approaches have been adopted in the literature to calibrate abundance diagnostics based on SELs. The first approach involves calibrating ratios of SELs against abundances derived from the Direct Method using local samples of H II regions. These calibrations are commonly known as "empirical calibrations." Alternatively, the second approach entails the use of theoretical photoionization models of H II regions, referred to as "theoretical calibrations."

For instance, Pagel et al. (1979) proposed using the four strongest lines of oxygen and hydrogen: $H\alpha$, $H\beta$, [O II] λ3727, and [O III] λ5007. As previously discussed, the relative intensities of these emission lines are primarily governed by three parameters: the electron temperature (T_e), the electron density (n_e), and

the metallicity, represented by the O/H ratio. The $H\alpha/H\beta$ ratio is employed to correct the spectra for reddening, leaving only two independent line ratios, [O II] $\lambda 3727/H\beta$ and [O III] $\lambda 5007/H\beta$, to determine three quantities. Building upon available photoionization model grids, Pagel et al. (1979) demonstrated that the ratio ([O II] $\lambda 3727$+ [O III] $\lambda 5007)/H\beta$, later termed R_{23}, could serve as an indicator of O/H. This calibration was subsequently revisited by Pilyugin and Thuan (2005).

Other examples of empirical calibrations include those of:

- The O_3N_2 = [O III] $\lambda 5007$/[N II] $\lambda 6583$ ratio, calibrated by Alloin et al. (1979), Pettini and Pagel (2004), and Marino et al. (2013).
- The N_2 = [N II] $\lambda 6583/H\alpha$ ratio, calibrated by Denicoló et al. (2002), Marino et al. (2013), and Morales-Luis et al. (2014).
- The S_{23} = ([S II] $\lambda 6717, 6731$+ [S III] $\lambda 9069, 9532)/H\beta$ ratio, calibrated by Vilchez and Esteban (1996) and Díaz and Pérez-Montero (2000).

Additionally, ratios such as Ar_3O_3 = [Ar III] $\lambda 7135$/[O III] $\lambda 5007$ and S_3O_3 = [S III] $\lambda 9069$/[O III] $\lambda 5007$ have been proposed by Stasińska (2006). More sophisticated calibrations using combinations of multiple line ratios have been developed by Pilyugin and Mattsson (2011) and Pilyugin et al. (2012). On the theoretical front, efforts have been made to predict line ratios using full radiative transfer and excitation/ionization calculations for idealized nebulae. Early attempts at theoretical calibrations include works by Shields and Searle (1978), Pagel et al. (1979), Dufour et al. (1980), Edmunds and Pagel (1984), McCall et al. (1985), and Dopita and Evans (1986). Recent theoretical calibrations for individual diagnostics have been provided by McGaugh (1991), Kewley and Dopita (2002), and Kobulnicky and Kewley (2004) for the R_{23} ratio. Kewley and Dopita (2002) have also contributed theoretical calibrations for the O_3N_2, N_2, S_{23}, and N_2O_2 = [N II] $\lambda 6548, 6583$/[O II] $\lambda 3726, 3729$ ratios.

A significant characteristic of all calibrations is the absence of a single, universally applicable relation across the entire range of metallicities found in H II regions. Instead, researchers develop calibration relations tailored to specific ranges of metallicities or distinct calibration relations for different intervals, often at high or low metallicities. Consequently, prior knowledge of the metallicity interval to which an H II region belongs is essential for selecting the appropriate calibration relation (e.g., Kewley & Dopita, 2002; Blanc et al., 2015). Failure to do

so can lead to erroneous calibration choices, resulting in substantial uncertainties in the derived abundances of the H II regions. This challenge becomes particularly pronounced for H II regions situated near the boundary of a calibration relation's applicability.

Despite everything, the SELs Method is practically the only one that can be used to estimate the metallicity of galaxies outside the Local Group and is, consequently, the most common. For this reason, in this thesis, we have focused our attention on this method and on a specific calibration, described in the following section.

2.3.1 R calibration and S calibration

In this study, we focus on the calibration established by Pilyugin and Grebel (2016). These are calibration equations capable of determining oxygen and nitrogen abundances across the entire spectrum of H II region metallicities with relative errors less than 0.1 dex. These equations, known as the "R calibration" and "S calibration," respectively, correlate oxygen abundance with the intensities of three strong lines: R_2, R_3, and N_2 for the former, and S_2, R_3, and N_2 for the latter. The line intensities are defined as follows:

$$R_2 = I_{[\mathrm{O\ II}]\ \lambda3727+\lambda3729}/I_{H\beta} \tag{2.11}$$

$$N_2 = I_{[\mathrm{N\ II}]\ \lambda6548+\lambda6584}/I_{H\beta} \tag{2.12}$$

$$S_2 = I_{[\mathrm{S\ II}]\ \lambda6717+\lambda6731}/I_{H\beta} \tag{2.13}$$

$$R_3 = I_{[\mathrm{O\ III}]\ \lambda4959+\lambda5007}/I_{H\beta} \tag{2.14}$$

Additionally, we employ the notation $(O/H)^* = 12 + \log(O/H)$ in order to write the equations in a more compact way.

In this work we analyze only the S calibration, since it is the most commonly used to recover metallicity from Integral Field Spectroscopy (IFS) with MUSE. In any case, to have a complete view of how empirical calibrations are determined and work, in this section we describe both.

Pilyugin and Grebel (2016) used a dataset comprising 313 H II regions, gathered under the framework of the C method[3] (Pilyugin et al., 2012), and for

[3]Known also as "counterpart method", it relies on the assumption that H II regions exhibiting similar strong-line intensities possess comparable physical properties and chemical

which the absolute differences in oxygen abundances $(O/H)_{C_{ON}} - (O/H)_{T_e}$ and $(O/H)_{C_{NS}} - (O/H)_{T_e}$, as well as nitrogen abundances $(N/H)_{C_{ON}} - (N/H)_{T_e}$ and $(N/H)_{C_{NS}} - (N/H)_{T_e}$, were all less than 0.1 dex (the sample was compiled by Zinchenko et al., 2016).

The nitrogen line N_2 intensity serves as an indicator of electron temperature, as outlined by the authors. This relationship is shown in panel a3 of Figure 2.1, where a clear monotonic relationship between electron temperature and $\log N_2$ is evident across the entire spectrum of electron temperatures within H II regions. Nevertheless, an appreciable difference emerge in this correlation between high and low temperature ranges. Particularly, a notable dependence of the $t - N_2$ relation on the excitation parameter P is observed at elevated electron temperatures, whereas this dependence dissipates at lower temperatures. The transition between these regimes manifests around $\log N_2 \approx -0.6$. Similar behaviors are observed in the nitrogen and oxygen abundances, illustrated in panels a2 and a1, respectively.

At the same time, panel b1 reveals a double-valued relation between the oxygen abundance and strong oxygen line intensities, traditionally categorized into upper (high-metallicity) and lower (low-metallicity) branches. Panels b2 and b3 demonstrate that the overall behavior of the $N/H - R_2$ and $t - R_2$ diagrams mirrors that of the $O/H - R_2$ diagram. Once again, these relations show a dependence on the excitation parameter P, particularly evident at low metallicities (high electron temperatures), yet diminishing at high metallicities (low electron temperatures). Consequently, the analysis of Figure 2.1 implies the necessity for distinct $O/H - R_2$ (and $N/H - R_2$) relations for the upper and lower branches, with the transition occurring approximately at $\log N_2 \sim -0.6$.

In general, the relation between the oxygen abundance in an H II region on the upper (or lower) branch and the oxygen R_2 line intensity in its spectrum is influenced by both electron temperature and excitation level. Thus, Pilyugin

abundances. This method begins with the creation of a reference sample of H II regions, where the abundances are well-measured and accurately determined. For any H II region under study, a suitable counterpart is selected from this reference sample by comparing combinations of strong-line intensities. Once an appropriate counterpart is identified, it is assumed that the oxygen and nitrogen abundances, as well as the electron temperature in the studied H II region, are equivalent to those in the corresponding counterpart. Essentially, this method infers the abundances in H II regions based on the precedent set by previously studied and well-characterized regions.

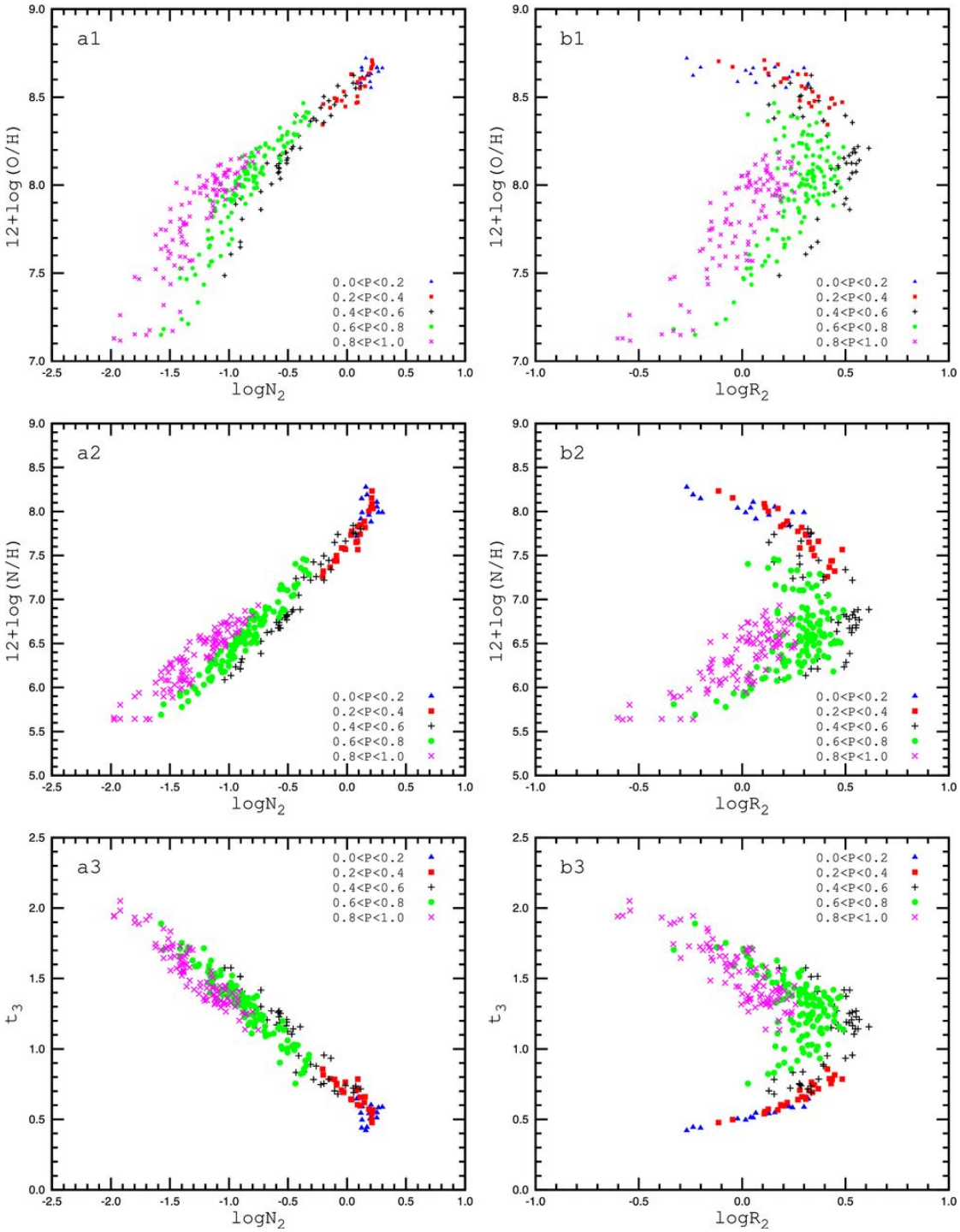

Figure 2.1: Oxygen abundances (panel a1), nitrogen abundances (panel a2), and electron temperatures t_3 (panel a3) as a function of the nitrogen line N_2 intensity for the sample of H II regions used as calibrating data points (from Pilyugin & Grebel, 2016). H II regions with different values of the excitation parameter P are plotted with different symbols and colors. Panels b1, b2, and b3 show the same as panels a1, a2, and a3 but as a function of the oxygen line R_2 intensity.

and Grebel (2016) proposed a straightforward linear expression:

$$12 + \log(O/H) = a(t, P) + b(t, P) \log R_2 \tag{2.15}$$

with the coefficients a and b depending on the electron temperature and the excitation parameter. Subsequently, under the assumption of linear dependence of coefficients a and b on electron temperature and excitation parameter, Equation 2.15 can be reformulated as:

$$\begin{aligned}(O/H)^* = a_1 + a_2 \log(R_3/R_2) + a_3 \log N_2 \\ + (a_4 + a_5 \log(R_3/R_2) + a_6 \log N_2) \times \log R_2\end{aligned} \tag{2.16}$$

In this expression, $(O/H)^*$ represents the oxygen abundance, with a_1, a_2, a_3, a_4, a_5, and a_6 being numerical coefficients. The study uses the value of $\log(R_3/R_2)$ to gauge the excitation level of an H II region and $\log N_2$ as an index of its electron temperature.

R calibration

Equation 2.16 serves as a valid calibration for abundance determinations in H II regions, particularly when the R_2 line is available. This calibration, referred to as "R calibration," is denoted as $(O/H)_R$. The coefficients for this calibration are derived by minimizing the average difference between the oxygen abundances determined through the calibration and the original values for the sample of calibrating data points.

Pilyugin and Grebel (2016) determined the following coefficients for H II regions with $\log N_2 \geq -0.6$ (the upper branch):

$$\begin{aligned}a_1 = 8.589, \quad a_2 = 0.022, \quad a_3 = 0.399 \\ a_4 = -0.137, \quad a_5 = 0.164, \quad a_6 = 0.589\end{aligned} \tag{2.17}$$

Resulting in the calibration expression:

$$\begin{aligned}(O/H)^*_{R,U} = 8.589 + 0.022 \log(R_3/R_2) + 0.399 \log N_2 \\ + (-0.137 + 0.164 \log(R_3/R_2) + 0.589 \log N_2) \times \log R_2\end{aligned} \tag{2.18}$$

While, for H II regions with $\log N_2 < -0.6$ (the lower branch), the coefficients

are:

$$\begin{aligned} a_1 &= 7.932, \quad a_2 = 0.944, \quad a_3 = 0.695 \\ a_4 &= 0.970, \quad a_5 = -0.291, \quad a_6 = -0.019 \end{aligned} \tag{2.19}$$

Resulting in the calibration expression:

$$\begin{aligned} (O/H)^*_{R,L} &= 7.932 + 0.944 \log(R_3/R_2) + 0.695 \log N_2 \\ &+ (0.970 - 0.291 \log(R_3/R_2) - 0.019 \log N_2) \times \log R_2 \end{aligned} \tag{2.20}$$

S calibration

In cases where the R_2 line ratio is unavailable, Pilyugin and Grebel (2016) introduced the sulfur line S_2 intensity as a substitute while retaining the same calibration framework as defined in Equation 2.16. This alternate calibration is referred to as "S calibration," labeled as $(O/H)_S$.

For H II regions in the upper branch ($\log N_2 \geq -0.6$), the coefficients obtained were:

$$\begin{aligned} a_1 &= 8.424, \quad a_2 = 0.030, \quad a_3 = 0.751 \\ a_4 &= -0.349, \quad a_5 = 0.182, \quad a_6 = 0.508 \end{aligned} \tag{2.21}$$

Resulting in the calibration expression:

$$\begin{aligned} (O/H)^*_{S,U} &= 8.424 + 0.030 \log(R_3/S_2) + 0.751 \log N_2 \\ &+ (-0.349 + 0.182 \log(R_3/S_2) + 0.508 \log N_2) \times \log S_2 \end{aligned} \tag{2.22}$$

While, for H II regions in the lower branch ($\log N_2 < -0.6$), the coefficients were:

$$\begin{aligned} a_1 &= 8.072, \quad a_2 = 0.789, \quad a_3 = 0.726 \\ a_4 &= 1.069, \quad a_5 = -0.170, \quad a_6 = 0.022 \end{aligned} \tag{2.23}$$

Resulting in the calibration expression:

$$\begin{aligned} (O/H)^*_{S,L} &= 8.072 + 0.789 \log(R_3/S_2) + 0.726 \log N_2 \\ &+ (1.069 - 0.170 \log(R_3/S_2) + 0.022 \log N_2) \times \log S_2 \end{aligned} \tag{2.24}$$

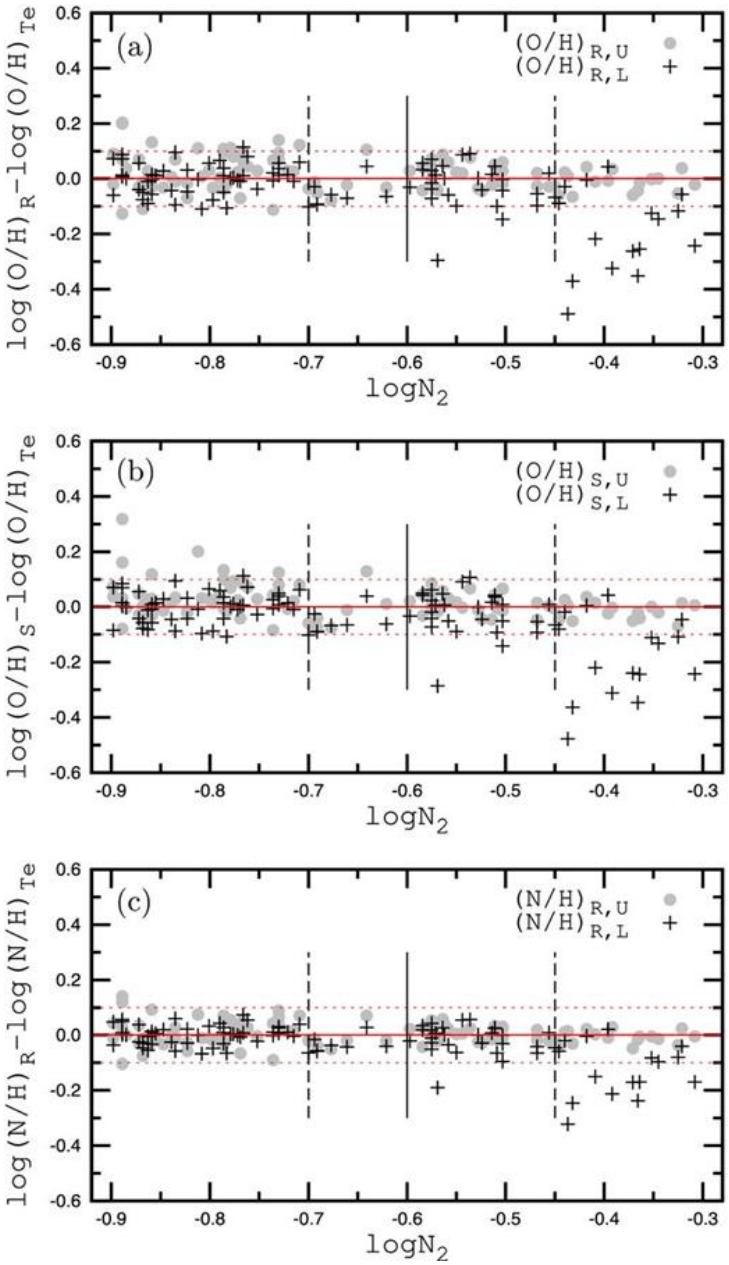

Figure 2.2: Comparison of abundances in H II regions with $\log N_2$ values close to the boundary (from Pilyugin & Grebel, 2016). Panel (a) shows the difference between the oxygen abundances derived from the R calibration for the upper branch and the direct T_e-based oxygen abundance, denoted as $(O/H)_{R,U} - (O/H)_{T_e}$ (circles), as well as the difference $(O/H)_{R,L} - (O/H)_{T_e}$ (plus signs), plotted against the intensity of the nitrogen line N_2. The solid vertical line represents the chosen boundary, while the dashed vertical lines indicate the range of $\log N_2$ where the two relations provide closely matching abundances. Panel (b) presents the same data as in panel (a), but using the S calibration. Panel (c) also follows the format of panel (a), focusing on nitrogen abundances instead.

The boundary region between the upper and the lower branches

The calibration relations used for determining abundances in H II regions are structured around a division into upper and lower branches, delineated by a threshold of $\log N_2 = -0.6$. H II regions with $\log N_2 \geq -0.6$ are classified as belonging to the upper branch, while those with $\log N_2 < -0.6$ are assigned to the lower branch.

However, it's important to note that this division is somewhat arbitrary, as inferred from the examination of Figure 2.1. Consequently, it's crucial to ensure that the abundances derived from the calibration relations for both branches remain consistent in the boundary region separating their applicability ranges.

To assess this, Pilyugin and Grebel (2016) conducted a study focusing on H II regions with nitrogen line N_2 intensities near the established boundary value, ranging from $\log N_2 = -0.9$ to -0.3. They obtained abundances using both the calibration relations for the upper and lower branches.

Their findings, shown in Figure 2.2, indicate that the two calibration methods (R and S calibrations) for the upper branch yield reasonably accurate oxygen abundances for objects with $\log N_2$ below the specified limit, extending up to $\log N_2 \sim -0.7$. Conversely, the calibration methods for the lower branch provide reasonably accurate oxygen abundances for objects with $\log N_2$ higher than the specified limit, up to $\log N_2 \sim -0.45$. As a result, there is an overlap in the ranges of applicability for the R and S calibration relations, spanning from $\log N_2 \sim -0.7$ to -0.45.

This overlap confirms the compatibility of the calibration relations for the lower and upper branches within the boundary region that separates their respective applicability ranges. Furthermore, in cases where H II regions exhibit nitrogen line intensities near the defined boundary value, potential misclassification due to errors in N_2 measurements does not significantly impact accuracy, thanks to the convergence between the two calibration methods.

2.4 Abundance discrepancies in SELs Methods

There exist notable systematic discrepancies among abundance values generated by different published calibrations. Theoretical calibrations tend to yield oxygen abundances that exceed those obtained through the Direct Method or empirical calibrations by factors ranging from 1.5 to 5 (Kewley & Ellison, 2008;

Bresolin et al., 2009; López-Sánchez & Esteban, 2010; Moustakas et al., 2010; López-Sánchez et al., 2012).

Single calibration methods can also produce varying results due to potential additional dependencies that are not always accounted for. This variability has been highlighted by several authors, including McGaugh (1991), Pilyugin (2000, 2001), and Blanc et al. (2015), who have pointed out that oxygen abundances derived using the R_{23} method often involve systematic errors, since it can be influenced by factors such as the excitation and ionization states of the gas. McGaugh (1991), Pilyugin (2000, 2001), and Blanc et al. (2015) have argued that these factors must be considered in metallicity calibrations to reduce discrepancies in R_{23} values observed among H II regions with the same oxygen abundance.

This ongoing discussion suggests that more complex models or additional correction factors may be necessary to improve the accuracy of the R_{23} method in different environments. As the understanding of these dependencies evolves, further research are needed to refine the calibration techniques and achieve more reliable results across diverse H II regions. Consequently, as of the present, there is no universally accepted absolute scale for determining metallicities of H II regions.

In addition to the known challenges, there are other potential sources of error that have not been fully considered or are not yet well understood. One such issue is the possible influence of the diffuse ionezed gas (DIG), a warm, low-density component of ionized gas that permeates the disk of star-forming galaxies, on the metallicity estimates of these regions. This ionized gas components have different properties with respect to those found in H II regions, therefore not correctly accounting for it can affect the metallicity measurements. The magnitude of this effect, however, is still a topic of ongoing discussion and investigation.

Another important aspect to consider is the consistency in the methods used to determine metallicity. Different approaches used to obtain the spectra can produce different results. An example is the specific area of the H II region that is selected by the slits or the fibers used during the observations.

At present, the emission line spectra of H II regions in galaxies have been obtained using various techniques, leading to potential inconsistencies. An extreme example is long slit spectroscopy. These slit spectra are not uniform, as the physical fraction of the H II region captured within the slit can vary

significantly due to several factors:

- differences in slit widths used in different studies,
- variations in the angular sizes of the H II regions, which can be influenced by both their intrinsic physical sizes and the distances to the galaxies,
- the specific part of the H II region (e.g., the center versus the periphery) that is intersected by the slit.

However, despite the limitations, this type of aperture has been employed in numerous studies to obtain spectra from H II regions across many near-by galaxies (e.g., compilations in Pilyugin et al., 2004, 2014; Zurita et al., 2021).

Our research aims to explore these two potential sources of observational biases: the influence of the DIG on metallicity estimates and the impact of varying spectral measurement techniques on the results. By addressing these issues, we hope to improve the accuracy and consistency of metallicity measurements in H II regions.

3

The PHANGS–MUSE Nebular Catalogue

To address the challenges associated with potential observational biases in metallicity estimation, as discussed in Chapter 2, it is crucial to work with a well-characterized catalog of H II regions. Specifically, these regions must have been observed using an integral field spectrograph. This type of observation is essential for extracting the DIG component and simulating different apertures. Additionally, the spectra must include all the emission lines required for metallicity estimation using the S-calibration method, as outlined in Section 2.3.1. The recently published catalog by Congiu et al. (2023) fulfills these criteria. This catalog comprises over 40,000 high-resolution spectra of extragalactic nebulae across 19 galaxies, providing an extensive and reliable dataset for our analysis.

These data are derived from the mosaicked MUSE IFS observations conducted under the Physics as High-Angular resolution in Nearby GalaxieS program (PHANGS-MUSE survey; Emsellem et al., 2022), which are part of a broader multi-wavelength survey of nearby galaxies initiated by the PHANGS collaboration (Leroy et al., 2021). The PHANGS project was conceived with a precise objective in mind: to resolve galaxies into their individual elements of the star-formation process, including molecular clouds, H II regions, and stellar clusters.

The PHANGS survey aimed at building a complete sample of southern-sky accessible ($-75° \leq \delta \leq +25°$), low inclination ($i < 75°$), and high-mass star-forming galaxies (with $\log(M_\star/M_\odot) > 9.75$ and $\log(sSFR/yr^{-1}) > -11$) within

a distance of approximately 5 – 20 Mpc, ensuring a resolution such that $1'' < 100$ pc (Leroy et al., 2021). The PHANGS-MUSE survey, as a component of this larger initiative, is an ESO large program dedicated to spectroscopically mapping the disks of 19 nearby star-forming galaxies. Table 3.1 summarizes the physical properties of these galaxies.

Given that all galaxies are within ~ 20 Mpc, the typical seeing of the MUSE observations allows for the isolation of structures down to 100 pc within the disk environment, with a median physical resolution of ~ 70 pc. Galaxy distances are based on the latest compilation by Anand et al. (2021), incorporating new tip of the red giant branch measurements. The galaxy inclinations and position angles were determined by Lang et al. (2020) through CO rotation curve analysis. The listed stellar masses represent global measures derived from UV and IR photometry (Leroy et al., 2021). Representative disc scale lengths are provided, including the 25th magnitude B-band isophotal radius (R_{25}) from RC3 (Makarov et al., 2014), and the effective radius containing half of the stellar mass of the galaxy (r_{eff}), compiled and computed by Leroy et al. (2021).

Each galaxy in the sample was observed with a varying number of pointings, ranging from 3 to 15, to map a significant fraction of its star-forming disk. All observations were conducted in Wide-Field Mode (WFM). The raw data collected were processed using `pymusepipe`, a Python wrapper for the ESO data reduction pipeline (Weilbacher et al., 2020). This tool was specifically adapted for the reduction of PHANGS data.

After reduction, the individual pointings were combined to produce a single mosaicked datacube for each target galaxy. Other that the mosaics with the original spatial resolution, a homogenized version was also obtained, where the Point-Spread Function (PSF) is consistent both spatially and across different wavelengths.

Following reduction, the data were further processed using the Data Analysis Pipeline (DAP) to extract high-level data products. These include continuum-subtracted cubes and two-dimensional maps of various line properties such as flux, velocity, and velocity dispersion, as well as stellar mass, age, and other parameters. The DAP is a `python`-based software built on the `gist` code (Bittner et al., 2019), enabling the extraction of detailed information from both emission lines and the stellar continuum observed in the data.

However, to compile the new catalogue of nebulae, it was chosen not to use the DAP-generated emission-line maps. This decision stems from a limitation

Table 3.1: General properties of the PHANGS-MUSE galaxies (from Groves et al., 2023).

Name	Distance	v_{sys}	PA	i	$\log_{10} M_\star$	R_{25}	r_{eff}	$E(B-V)_{MW}$	resolution
	Mpc	km s^{-1}	deg	deg	$M_\odot$	arcmin	arcmin	mag	pc
IC5332	9.0	699	74.4	26.9	9.67	3.0	1.4	0.014	45
NGC0628	9.8	651	20.7	8.9	10.34	4.9	1.4	0.061	42
NGC1087	15.9	1502	359.1	42.9	9.93	1.5	0.7	0.030	71
NGC1300	19.0	1545	278.0	31.8	10.62	3.0	1.2	0.026	62
NGC1365 *	19.6	1613	201.1	55.4	10.99	6.0	3.3 [f]	0.018	84
NGC1385	17.2	1477	181.3	44.0	9.98	1.7	0.7	0.017	96
NGC1433 *	18.6	1057	199.7	28.6	10.87	3.1	0.8	0.008	83
NGC1512	18.8	871	261.9	42.5	10.71	4.2	0.9	0.009	96
NGC1566 *	17.7	1483	214.7	29.5	10.78	3.6	0.6	0.008	76
NGC1672 *	19.4	1318	134.3	42.6	10.73	3.1	0.6	0.020	73
NGC2835	12.2	867	1.0	41.3	10.00	3.2	0.9	0.086	33
NGC3351	10.0	775	193.2	45.1	10.36	3.6	1.0	0.024	43
NGC3627 *	11.3	715	173.1	57.3	10.83	5.1	1.1	0.029	69
NGC4254	13.1	2388	68.1	34.4	10.42	2.5	0.6	0.033	61
NGC4303 *	17.0	1560	312.4	23.5	10.52	3.4	0.7	0.019	96
NGC4321	15.2	1572	156.2	38.5	10.75	3.0	1.2	0.023	59
NGC4535	15.8	1954	179.7	44.7	10.53	4.1	1.4	0.017	80
NGC5068	5.2	667	342.4	35.7	9.40	3.7	1.3	0.090	23
NGC7496 *	18.7	1639	193.7	35.9	10.00	1.7	0.7	0.008	104

* Classified as an AGN by Véron-Cetty and Véron (2010).

in the DAP's design: it cannot return negative flux values when fitting emission lines. Consequently, when fitting a line where no emission is present, the DAP may produce positively biased flux values that could mimic the emission from faint regions. These artifacts can then be erroneously identified by segmentation algorithms when attempting to detect faint objects. To mitigate this issue, the authors opted to integrate the flux over a fixed wavelength window within a continuum-subtracted cube to create channel-integrated flux maps.

Therefore, the fluxes included in the catalogue, which serve as the foundation for this work, are derived from these integrated fluxes, while the DAP products, specifically the line maps, will be used to analyze biases related to the dimensions of the apertures.

3.1 Construction of the catalogue

The latest iteration of the PHANGS–MUSE Nebular Catalogue is a compendium comprising over 40,000 nebulae. The initial identification of these regions used CLUMPFIND (Williams et al., 1994). This algorithm adopts a contour-based methodology, identifying peaks and then connecting pixels within the same contour to the nearest peak, emulating the human eye's process. While proficient at identifying peaks, it tends to overestimate sizes and can

Table 3.2: Wavelengths and ionisation potential of each emission line included in the PHANGS–MUSE Nebular Catalog (Groves et al., 2023; Congiu et al., 2023).

Line name	Wavelength [Å]	String ID	Ionization potential [eV]	Fixed ratio
		Hydrogen lines		
Hβ	4861.35	`HB4861`	13.60	no
Hα	6562.79	`HA6562`	13.60	no
		Other lines		
[O I]λ6300	6300.30	`OI6300`	-	no
[N II]λ6548 *	6548.05	`NII6548`	14.53	0.34 [N II]λ6584
[N II]λ6584	6583.45	`NII6583`	14.53	no
[S II]λ6717	6716.44	`SII6716`	10.36	no
[S II]λ6731	6730.82	`SII6730`	10.36	no
[O III]λ4959 *	4958.91	`OIII4958`	35.12	0.35 [O III]λ5007
[O III]λ5007	5006.84	`OIII5006`	35.12	no
[S III]λ9068	9068.6	`SIII9068`	23.34	no

* Not included in Congiu et al. (2023) catalogue, but can be recovered by using the fixed ratios provided.

yield a notable fraction of false positives due to noise spikes. Subsequently, the maps underwent refinement through a custom algorithm designed to discard spurious detections and enhance segmentation accuracy (Congiu et al., 2023). The identified nebulae were then classified through the comparison of their observed properties with model grids representing the classes of ionized nebulae prevalent in galaxies: H II regions, PNe, and shock-ionized nebulae.

The output of this process included segmentation maps alongside a catalogue providing fundamental data such as the position of the region peak, flux-weighted center, area (in pixels) encompassed by the region, maximum radius, and circularized radius. Across a sample of 19 galaxies, a total of 40,920 nebulae were detected, averaging approximately 2,150 nebulae per galaxy. Line fluxes were recovered by fitting the 1D spectra of the nebulae, extracted from the cube using the segmentation maps. Table 3.2 lists the lines integrated into the fitting process.

3.1.1 DIG correction

In most galaxy, a warm, low-density component of ionized gas, known as DIG, permeates the entire galactic disk. While the precise ionization source

of this gas remains a topic of debate (see Belfiore et al., 2022), research has demonstrated that DIG can contribute significantly to the total line emission in certain galaxies (Thilker et al., 2002; Oey et al., 2007; Blanc et al., 2009).

This diffuse emission exhibits a larger scale height compared to the distribution of ionized nebulae and can contaminate the integrated spectra of ionized nebulae due to projection effects. Consequently, when measuring emission line fluxes in H II regions or other types of nebulae, contamination from DIG emission must be considered. The extent of this contamination varies depending on the relative strength of nebula emission compared to DIG, that is, it affects the faintest nebulae the most.

The primary challenge posed by DIG contamination is its distinct feature of exhibiting enhanced low-ionization line emission compared to the spectra of other nebulae, like H II regions and PNe. Consequently, DIG emission can significantly distort the line ratios of observed nebulae, potentially leading to misclassification of DIG-dominated regions if this contamination is not properly accounted for. To address this concern, the Congiu et al. (2023) catalogue corrected the line fluxes for DIG contamination. To accurately correct the spectra of the sources for DIG emission, the following procedure was implemented:

- **Gaussian Filtering and Expansion**: For each region, it was first applied a Gaussian filter with a standard deviation corresponding to the circularized radius of the nebula. This step enlarges the perceived size of the nebula, allowing to better account for the surrounding DIG.

- **Masking and Annulus Extraction**: Next, the area covered by the original nebula was masked, isolating it from further analysis. An annular region around the nebula was then extracted, the size of which was determined by the circularized radius of the original nebula. This annulus serves as the region from which estimate the DIG emission. To avoid contamination, any overlap between this annulus and neighboring regions is masked.

- **DIG Spectrum Extraction**: The DIG spectrum associated with each region was extracted using the isolated annulus. The same spectral extraction algorithm employed for measuring the line fluxes of the nebulae was used here to ensure consistency.

- **Applying the Correction**: After extracting the DIG spectrum, a correction was applied to the nebula's line fluxes. This was done by subtracting the

Table 3.3: Distribution of the regions in the classes defined by Congiu et al. (2023) as a function of the considered sample.

Class	Full sample	Hα sample	[O III] sample	BPT sample
H II	29 986	23 939	14 313	10 993
PNe	796	535	775	32
Shock	6 336	4 454	4 181	2 356
Ambiguous	3 722	3 222	2 556	1 546
Unclassified	80	60	71	47
Total	40 920	32 210	21 896	14 977

estimated DIG flux from the observed flux of each line within the nebula. A rescaling factor is applied during this subtraction to account for the difference in size between the original nebula and the extracted annulus.

In certain cases, particularly for faint regions located in crowded areas where DIG emission varies significantly, the estimated DIG emission may exceed the flux emitted by the nebula itself. When this occurs, these lines are treated as undetected. For subsequent analyses, their flux is replaced by an upper limit, determined through formal error propagation of the nebula and DIG emission line fluxes.

3.1.2 Classification

The authors developed a classification algorithm that relies on comparing the morphological and spectral characteristics of regions with established models of nebular properties. This method uses the principle of odds ratio, which associates to each nebula the probability it belongs to each of the considered class (Congiu et al., 2023). This algorithm was crafted to address several limitations inherent in traditional classification criteria.

As previously mentioned, the catalog encompasses 40,920 regions, with the majority (29,986 objects) classified as H II regions (i.e., their probability of being H II region > 90%). Following closely are shock-ionized nebulae, with 6,336 objects, succeeded by PNe totaling 796 objects. A subset of 3,722 sources presents an ambiguous classification (no class with a probability > 90%), with the ambiguity mainly between H II regions and shock classifications. Additionally, a small portion of the catalog comprises unclassified objects (80).

However, it's worth noting that the absence of detection in certain spectral lines can influence the final classification outcome. To investigate the impact of

the number of detected lines on nebular classifications, Congiu et al. (2023) constructed three sub-samples, each necessitating 3σ detections for distinct subsets of emission lines. Apart from the full sample, the authors examined:

- An "Hα sample", mandating a 3σ detection of the Hα line.
- An "[O III] sample", requiring a 3σ detection of the [O III]λ5007 line.
- A "BPT sample", imposing 3σ detections for all the lines requisite to construct BPT diagrams ([O III]λ5007, Hβ, Hα, [N II]λ6584, [S II]λ6717, [S II]λ6731, [O I]λ6300).

The total number of regions in each sample is outlined in Table 3.3.

For the specific aims and analyses of this study, the BPT sample of H II regions was used, which included a total of 10,993 objects. These H II regions are visually represented in Figures 3.1 and A.1-A.18, organized by galaxy.

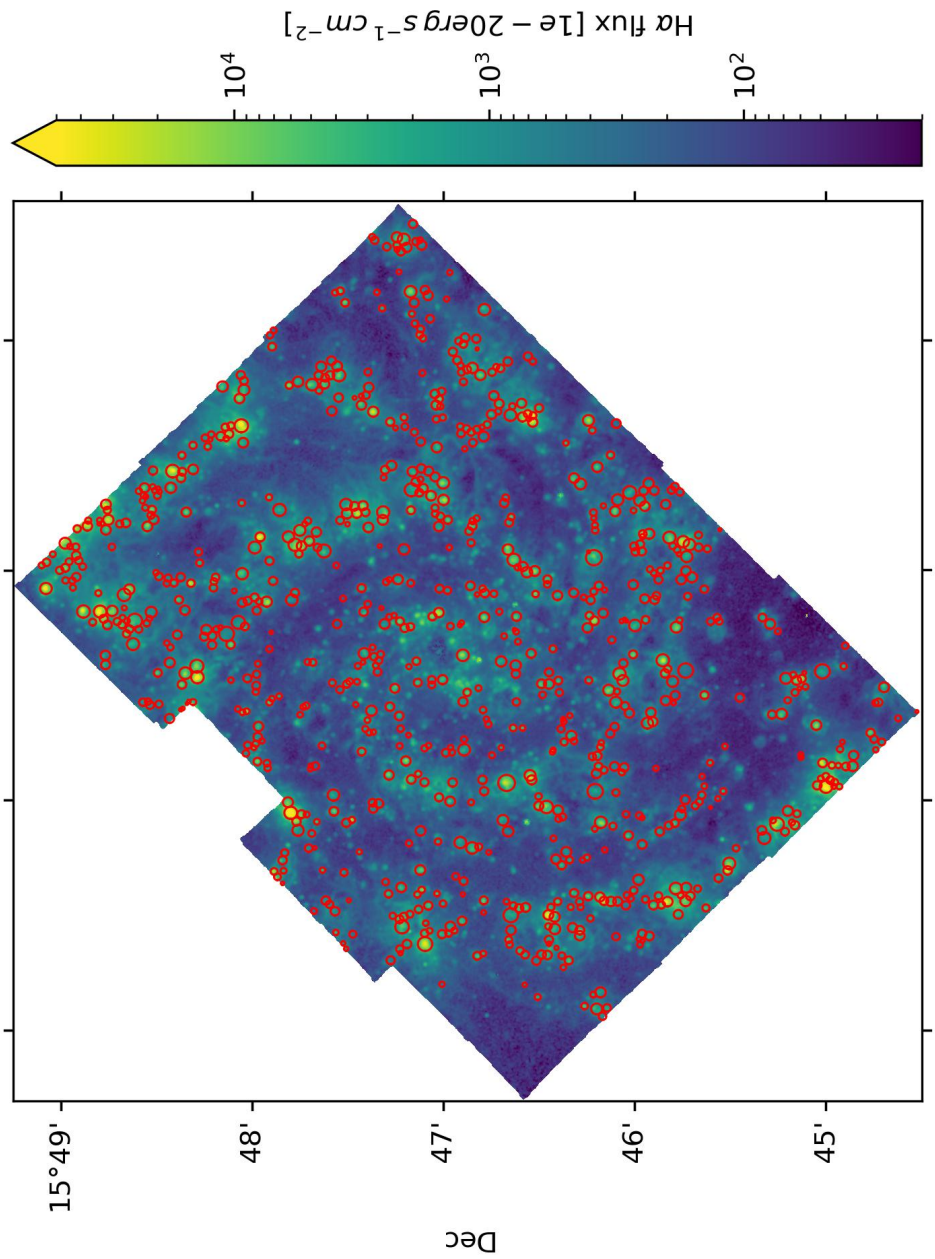

Figure 3.1: Spatial distribution of the H II regions within the galaxy NGC0628, as selected in this work. The background image shows the Hα emission. Additionally, the dimensions of the circles represent the sizes of the H II regions, as computed by Congiu et al. (2023) and reported in the PHANGS-MUSE Nebular Catalogue.

4

Data analysis: DIG relevance in metallicity measurements

This section focuses on analyzing whether DIG contamination affects the computation of metallicity in H II regions. The study uses the "BPT sample" from the PHANGS-MUSE Nebular Catalogue, as defined in Section 3.1.2, which includes 10,993 H II regions.

For each H II region in the sample, the catalogue provides the measured line fluxes necessary to estimate metallicity using the S-calibration method from Pilyugin and Grebel (2016). Importantly, the catalogue offers two sets of flux measurements for each line: DIG-corrected values and uncorrected values. This allowed us to compute two distinct sets of metallicity estimates. By comparing them, we aim to determine the impact of DIG contamination on the metallicity estimates of H II regions.

4.1 Correction for internal extinction

To accurately estimate the metallicity, it is essential to correct for internal extinction caused by the dust in the galaxies. This correction is necessary because the data had not been pre-corrected for this extinction. The reddening, which results from dust absorption, is measured by comparing the observed $H\alpha/H\beta$ ratio with its theoretical value for a nebula at a temperature of 10,000 K ($H\alpha/H\beta$ = 2.86, Osterbrock & Ferland, 2006). The correction process used

the reddening law proposed by Cardelli et al. (1989), with a parameter value of $R_V = 3.1$. The extinction values, $E(B-V)$, associated to each nebulae and obtained in this way, have been already published in the PHANGS-MUSE Catalogue (Congiu et al., 2023). In particular, the catalogue included two distinct $E(B-V)$ values: one derived from the measured fluxes and another from the DIG corrected fluxes. Consequently, we performed separate corrections for each data type. The measured fluxes were corrected using the $E(B-V)$ obtained from the measured fluxes, while the DIG corrected fluxes were adjusted using the DIG corrected $E(B-V)$. We applied the correction using the `PyNeb` Python package (Luridiana et al., 2015).

4.2 Metallicity estimation

Considering the line fluxes available in the catalogue and the fixed ratios necessary to compute the missing line fluxes (see 3.2), we used the the S-calibration relations as defined in Equations 2.22 and 2.24 to compute two different estimations for the metallicity of the H II regions in the sample. The first estimation, labeled $(O/H)_{ORIG}$, is derived from the measured fluxes, while the second estimation, labeled $(O/H)_{DIG}$, is derived from the DIG corrected fluxes.

The errors on the measurements were computed using standard error propagation techniques. The errors on the line ratios are given by:

$$\sigma_{N_2} = N_2 \sqrt{\left(\frac{\sigma_{I_{[\mathrm{N\ II}]\ \lambda6584}}}{I_{[\mathrm{N\ II}]\ \lambda6584}}\right)^2 + \left(\frac{\sigma_{I_{H\beta}}}{I_{H\beta}}\right)^2} \tag{4.1}$$

$$\sigma_{R_3} = R_3 \sqrt{\left(\frac{\sigma_{I_{[\mathrm{O\ III}]\ \lambda5007}}}{I_{[\mathrm{O\ III}]\ \lambda5007}}\right)^2 + \left(\frac{\sigma_{I_{H\beta}}}{I_{H\beta}}\right)^2} \tag{4.2}$$

$$\sigma_{S_2} = S_2 \sqrt{\frac{\sigma^2_{I_{[\mathrm{S\ II}]\ \lambda6717}} + \sigma^2_{I_{[\mathrm{S\ II}]\ \lambda6731}}}{(I_{[\mathrm{S\ II}]\ \lambda6717} + I_{[\mathrm{S\ II}]\ \lambda6731})^2} + \left(\frac{\sigma_{I_{H\beta}}}{I_{H\beta}}\right)^2} \tag{4.3}$$

These errors, in logarithmic form, become:

$$\sigma_{\log N_2} = \frac{\sigma_{N_2}}{N_2 \cdot \ln 10}, \quad \sigma_{\log S_2} = \frac{\sigma_{S_2}}{S_2 \cdot \ln 10} \tag{4.4}$$

at the same time, the error on the ratio R_3/S_2 and its logarithm are:

$$\sigma_{R_3/S_2} = \frac{R_3}{S_2}\sqrt{\left(\frac{\sigma_{R_3}}{R_3}\right)^2 + \left(\frac{\sigma_{S_2}}{S_2}\right)^2}, \quad \sigma_{\log(R_3/S_2)} = \frac{\sigma_{R_3/S_2}}{R_3/S_2 \cdot \ln 10} \tag{4.5}$$

4.3 Results

The results of this analysis are illustrated in Figure 4.1. This figure provides a comparison between the original metallicity measurements and those corrected for the DIG component. In the plot, the x-axis represents the metallicity derived from the measured fluxes, which we labeled as $(O/H)_{ORIG}$, while the y-axis represents the DIG-corrected metallicity, labeled as $(O/H)_{DIG}$. The dashed grey line represents the 1-to-1 diagonal, which serves as a reference indicating perfect agreement between the two sets of measurements.

From the plot, it is evident that the data points align closely with the diagonal line, indicating no significant offset between the metallicity measurements derived from the total fluxes and those corrected for the DIG component. This lack of systematic deviation suggests that the original metallicity estimates are not systematically biased by the presence of the DIG. The linear fit to the data yields a slope of 1.004 ± 0.001 and an intercept of -0.03 ± 0.01, further confirming the close alignment with the 1-to-1 line.

However, the distribution of points around the diagonal line shows a significant scatter of ~ 0.15 dex. This level of scatter is comparable to the azimuthal variations in metallicity observed in several nearby galaxies (such as those reported byHo et al. (2017) and Kreckel et al. (2019)). This finding implies that while there is no systematic error, the scatter remains an important factor to consider.

The observed scatter could have two potential origins. On one hand, it might represent intrinsic variations in metallicity within the H II regions themselves, reflecting true physical differences that are somewhat mitigated by the DIG contribution. On the other hand, it could be due to uncertainties in the DIG correction process, which involves some level of arbitrariness, in particular with the selection of the area from which to compute the DIG associated to each region. An imprecise correction could introduce an artificial scatter that is not physically meaningful.

To explore this further, we examined how the scatter changes as a function of

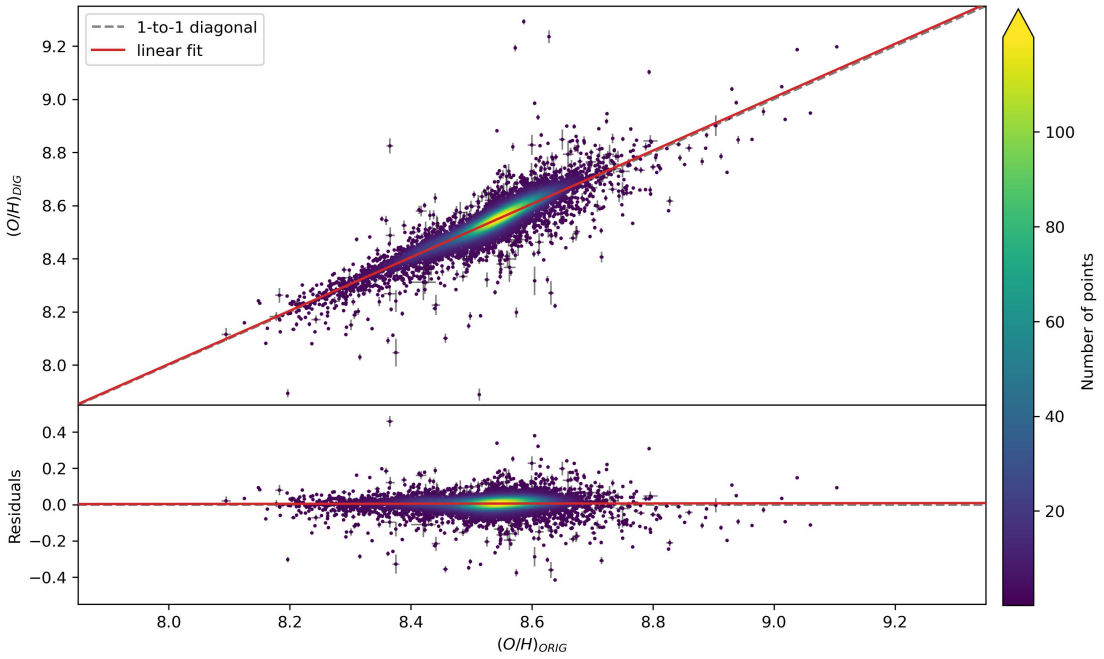

Figure 4.1: Scatter plot comparing the original metallicity measurements with those corrected for the DIG component. The x-axis represents the metallicity derived from the measured fluxes, labeled as $(O/H)_{ORIG}$, while the y-axis represents the DIG-corrected metallicity, labeled as $(O/H)_{DIG}$. The dashed grey line represents the 1-to-1 diagonal, which serves as a reference line indicating perfect agreement between the two sets of measurements. The points are closely aligned with the diagonal line, with a mean scattering of ~ 0.15. The red line shows the linear fit of the data.

different parameters, such as the luminosity of the H II regions and the contrast between the flux of these regions and the surrounding DIG.

4.3.1 Luminosity and contrast separation

To further analyze potential dependencies on various properties of nebulae, we divided our sample into different bins based on luminosity and contrast. The luminosity bins were determined using the $H\alpha$ luminosity provided in the catalogue. For the contrast, denoted as C, we calculated it as the ratio between the flux of the H II region and the flux of the DIG component. This contrast can be mathematically expressed as:

$$C = \frac{I_{\mathrm{H\,II}}}{I_{\mathrm{DIG}}} \tag{4.6}$$

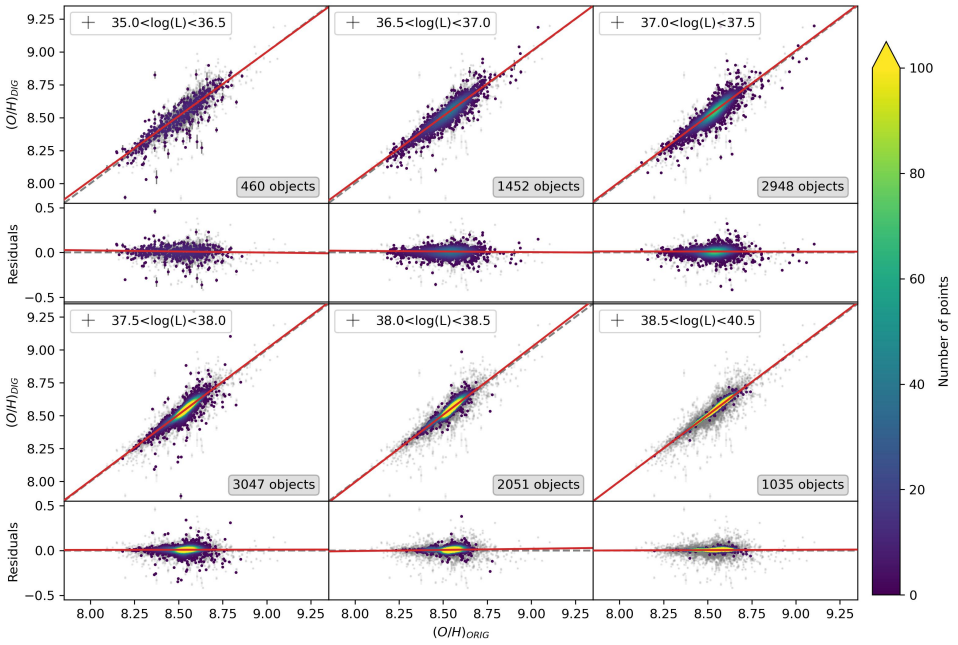

(a)

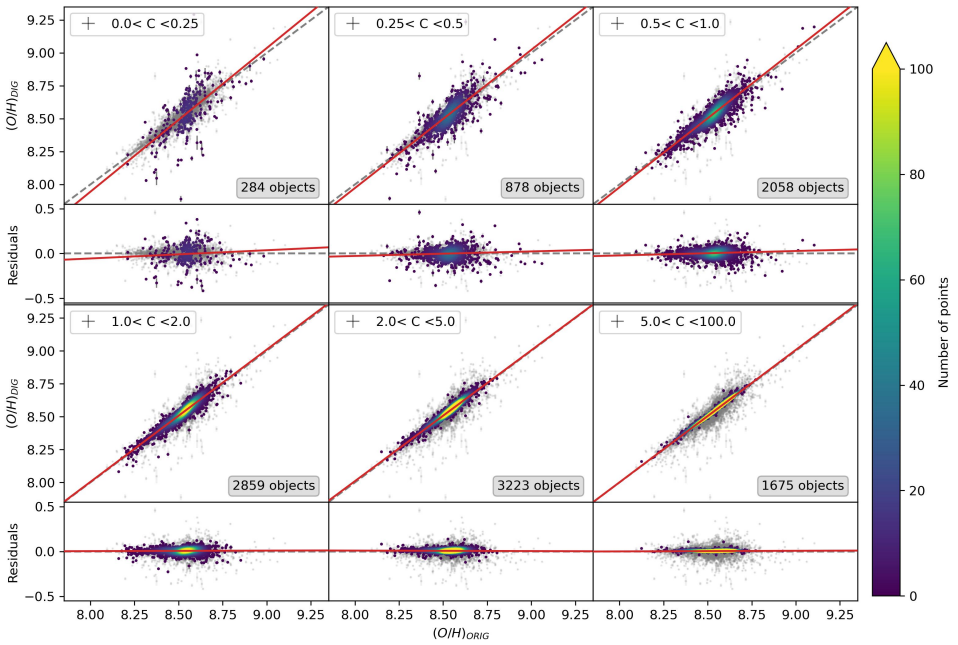

(b)

Figure 4.2: As Figure 4.1 but with the sample data divided into (a) bins based on luminosity and (b) bins based on contrast. For the luminosity bins, we used the $H\alpha$ luminosity values provided in the catalogue. For the contrast bins, we computed the contrast as the ratio between the flux of the H II region and the flux of the DIG component. Each subplot displays the total number of points in each bin. The full sample of data is plotted in gray for comparison. The red line is the linear fit of the sample (the coefficients are reported in Table 4.1 and 4.2).

Table 4.1: Coefficients of the linear fit ($y = Ax + B$) of the sample of data divided into bins of luminosity, shown in Figure 4.2a, along with the weighted scattering for the data points with respect to the 1-to-1 diagonal, labelled σ.

Bin	A	B dex	σ dex
$35.0 < \log(L_{H\alpha}) < 36.5$	0.98 ± 0.02	0.2 ± 0.1	0.106
$36.5 < \log(L_{H\alpha}) < 37.0$	0.986 ± 0.007	0.13 ± 0.06	0.074
$37.0 < \log(L_{H\alpha}) < 37.5$	0.998 ± 0.006	0.03 ± 0.05	0.063
$37.5 < \log(L_{H\alpha}) < 38.0$	1.003 ± 0.004	-0.02 ± 0.03	0.043
$38.0 < \log(L_{H\alpha}) < 38.5$	1.026 ± 0.004	-0.21 ± 0.03	0.045
$38.5 < \log(L_{H\alpha}) < 40.5$	1.007 ± 0.003	-0.05 ± 0.03	0.013

Table 4.2: Coefficients of the linear fit ($y = Ax + B$) of the sample of data divided into bins of contrast, shown in Figure 4.2b, along with the weighted scattering for the data points with respect to the 1-to-1 diagonal, labelled σ.

Bin	A	B dex	σ dex
$0.0 < C < 0.25$	1.09 ± 0.08	-0.8 ± 0.6	0.130
$0.25 < C < 0.5$	1.05 ± 0.03	-0.4 ± 0.2	0.081
$0.5 < C < 1.0$	1.05 ± 0.01	-0.42 ± 0.08	0.061
$1.0 < C < 2.0$	1.006 ± 0.006	-0.04 ± 0.05	0.068
$2.0 < C < 5.0$	0.995 ± 0.003	0.05 ± 0.02	0.053
$5.0 < C < 100.0$	1.007 ± 0.002	-0.05 ± 0.01	0.012

where $I_{\mathrm{H\,II}}$ represents the flux of the H II region and I_{DIG} is the flux of the DIG component.

The flux of the DIG component was derived by subtracting the DIG-corrected line fluxes from the measured line fluxes. This process was applied to six different emission lines: $H\alpha$, $H\beta$, [N II]λ6584, [S II]λ6717, [S II]λ6731 and [O III]λ5007. Consequently, we obtained six individual contrast values, one for each line. The mean of these values was then calculated to represent the overall contrast for each region. According to our definition, a contrast value between 0 and 1 indicates that the H II region is, on average, less intense than the surrounding gas. On the other hand, a contrast value equal to or greater than 1 signifies that the H II region is more intense than the DIG on average.

Our analyses, illustrated in Figures 4.2a and 4.2b, revealed that the scatter of data points gradually decreased as the luminosity or contrast of the H II region increased. This is expected, since typically the most luminous regions are also

Table 4.3: Coefficients of the linear fit ($y = Ax + B$) of the sample of data divided by galaxy, shown in Figure 4.3, along with the weighted scattering for the data points with respect to the 1-to-1 diagonal, labelled σ.

Bin	A	B dex	σ dex
IC5332	1.03 ± 0.01	-0.23 ± 0.09	0.031
NGC0628	1.018 ± 0.008	-0.14 ± 0.07	0.051
NGC1087	1.030 ± 0.008	-0.24 ± 0.07	0.045
NGC1300	1.074 ± 0.009	-0.62 ± 0.07	0.026
NGC1365	0.984 ± 0.007	0.14 ± 0.06	0.076
NGC1385	1.08 ± 0.01	-0.7 ± 0.1	0.057
NGC1433	1.000 ± 0.008	0.02 ± 0.07	0.072
NGC1512	1.04 ± 0.02	-0.4 ± 0.2	0.125
NGC1566	1.072 ± 0.009	-0.61 ± 0.08	0.104
NGC1672	1.025 ± 0.008	-0.21 ± 0.07	0.078
NGC2835	1.043 ± 0.007	-0.36 ± 0.06	0.054
NGC3351	1.04 ± 0.02	-0.3 ± 0.1	0.091
NGC3627	1.23 ± 0.02	-2.0 ± 0.2	0.139
NGC4254	1.132 ± 0.008	-1.12 ± 0.07	0.038
NGC4303	1.082 ± 0.009	-0.70 ± 0.08	0.037
NGC4321	1.11 ± 0.01	-1.0 ± 0.1	0.061
NGC4535	1.03 ± 0.01	-0.26 ± 0.09	0.120
NGC5068	1.04 ± 0.02	-0.3 ± 0.1	0.073
NGC7496	1.06 ± 0.01	-0.50 ± 0.09	0.027

those who are less affected by the contamination from the DIG. It also confirms that only bright regions with minimal DIG contamination should be used when investigating spatial metallicity variations, in particular if these variations are below 0.15 dex with respect to the average.

Figure 4.2b illustrates that, with the exception of a few regions exhibiting very low contrast (below 0.5), there is no systematic offset or significant trend between the two metallicity measurements. This indicates that reliable metallicity estimates can still be obtained even in environments with a relatively strong DIG contribution and low contrast, if a sufficient number of H II regions can be identified and measured.

4.3.2 Individual galaxies

In figure 4.3 we compare the DIG corrected vs measured flux metallicity relation for each galaxy in the sample. In the majority of cases, we still observe no

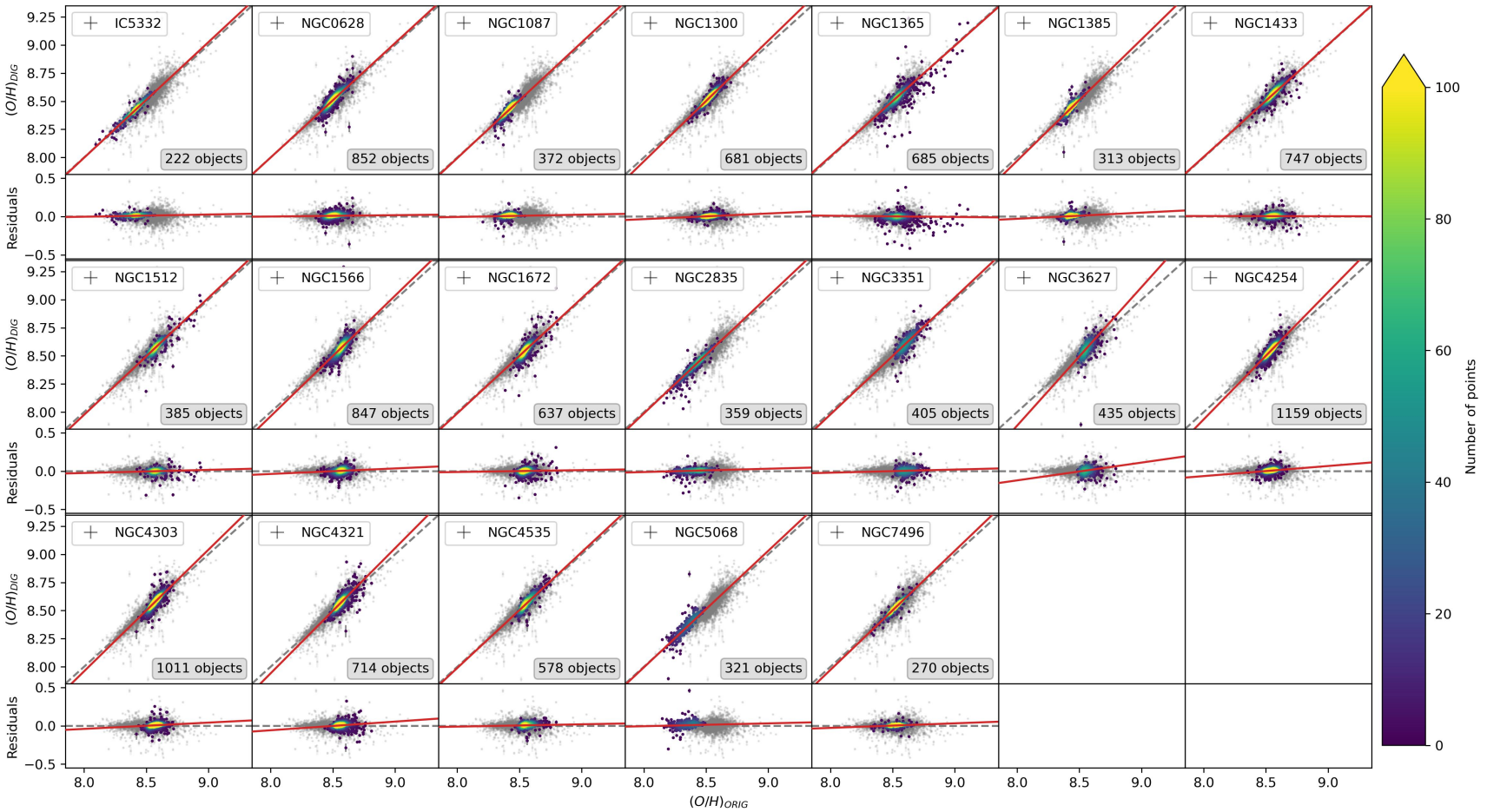

Figure 4.3: As Figure 4.1 but with the sample data divided by galaxy. Each subplot displays the total number of points in each galaxy. The full sample of data is plotted in gray for comparison. The red line is the linear fit of the sample (the coefficients are reported in Table 4.3).

systematic offset or other trend. A few galaxies (NGC1300, NGC1385, NGC4303, NGC4321) show some minor deviations, while two galaxies, NGC3627 and NGC4254, show a more pronounced deviation from the diagonal line.

Upon comparing these findings with the data presented in Table 3.1, it becomes evident that the galaxies that deviates more from the 1-to-1 relation are Active Galactic Nuclei (AGN). This correlation suggests that the presence of an AGN may contribute to the ionization of the DIG. As a result, the DIG becomes brighter, thereby increasing its contribution to the overall flux attributed to H II regions, and also exhibits altered properties. Consequently, this leads to a steeper slope in the metallicity relation.

These observations imply that AGNs might play a significant role in shaping the dynamics and characteristics of both H II regions and the surrounding DIG within their host galaxies. The energetic processes associated with AGNs could be affecting the ionization states or altering the spatial distribution of the DIG, thereby influencing the observed metallicities. Further investigation into the specific mechanisms driving this influence could provide deeper insights into the interplay between AGNs, the DIG, and star-forming regions in galaxies.

Interestingly, NGC1365, which is known to have a prominent ionization cone, does not show significant deviations from the expected relation. This could be because the region of the galaxy dominated by the ionization cone is relatively poor in H II regions, thus limiting the impact of the AGN on the measured metallicity trends in that area.

5

Data analysis: Influence of apertures' dimensions in metallicity estimations

The second part of this work aimed to explore the potential dependence of metallicity on the size of the aperture used to obtain the spectra of H II regions. The idea is to verify whether there is a bias in the measured metallicities when using traditional observation techniques, such as slit or fiber multi-object spectroscopy. Such biases could arise from an incomplete coverage of the examined H II region, or from crowding (i.e., the presence of multiple H II regions) in the considered aperture. For this reasons, we specifically focused on rectangular apertures, which represent slits, and circular apertures, which represent fibers, to investigate whether the use of either rectangular slits or circular fibers influence the measurements.

Also in this case, we selected only the H II regions belonging to the "BPT sample" from the PHANGS-MUSE Nebular Catalogue, as defined in Section 3.1.2, which includes 10,993 H II regions. To measure the fluxes in the different apertures, we used the emission line map produced by the DAP and released by the PHANGS collaboration in Emsellem et al. (2022), and the segmentation maps released in Congiu et al. (2023).

5.1 Information on the aperture's size

With this experiment, we aim to verify how different types of apertures affect the final measurement of metallicity. We selected aperture sizes in parsecs to make them independent of the distance to each galaxy. By defining the apertures in physical units, we ensure that the comparison across different galaxies remains uniform, as parsecs allow us to account for the varying distances of these galaxies without introducing bias related to their apparent size. During the simulation process, these dimensions were subsequently converted to arcseconds, based on the distance to each galaxy.

For the simulations, we employed both rectangular and circular apertures to model the observations. For both types of apertures, we used the same set of dimensions: 300 pc, 200 pc, 150 pc, 100 pc, 50 pc, and 20 pc. For rectangular slits, these values represent the width of the aperture, while for circular apertures, they represent the diameter. The length of each rectangular aperture was adjusted to correspond to the size of the H II region under consideration.

The flux measurements were obtained by performing aperture photometry on the emission line maps using the different aperture sizes. The measurement involved summing the contributions from all the pixels within the simulated apertures. The process also considered the presence of fractional pixels within the aperture, following the guidelines of the `photutils` Python package as described by Bradley et al. (2024).

Using the same script defined in the previous chapter, we corrected all measured fluxes for internal extinction. We then estimated the metallicity using the S-calibration method as described by Pilyugin and Grebel (2016).

However, a significant issue arose due to the fact that the fluxes of the catalogue and the ones from the simulations were obtained using different methodologies, making a direct comparison between them potentially inaccurate. The catalogue fluxes were derived from the data cubes by integrating the spectrum of each region before fitting it. In contrast, the simulation fluxes were obtained by summing the pixel values from two-dimensional emission line maps within the specified apertures. The discrepancy here is that in the catalogue, fluxes were integrated first and then fitted, whereas in our simulations, we are fitting the data first (to produce the emission line maps) and then integrating. Although theoretically there should be no difference, as we can see in Figure 5.2, practically the integration and fitting processes differ, potentially leading to

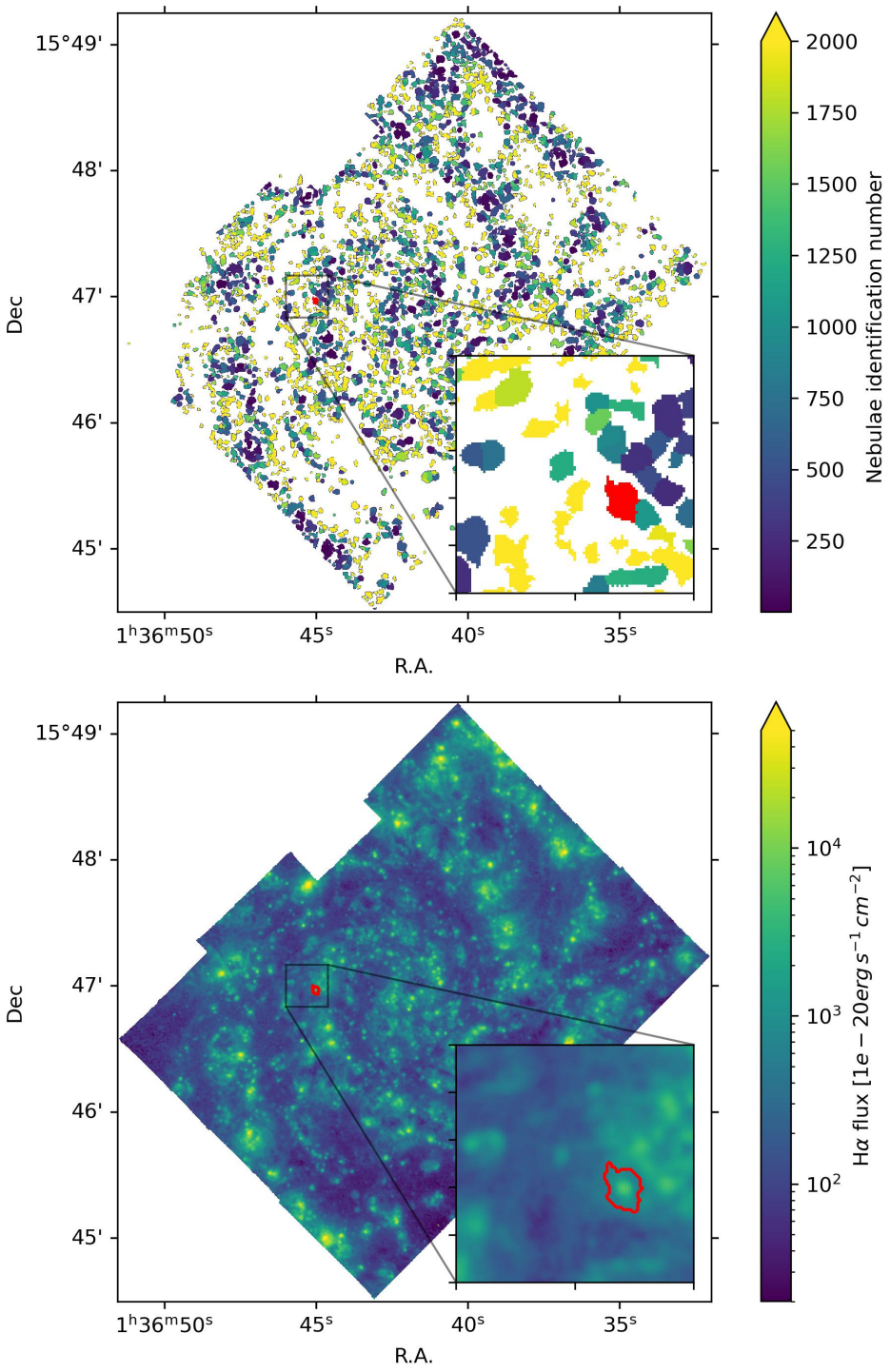

Figure 5.1: The process of re-estimating the original line fluxes by using the segmentation map is shown here (for galaxy NGC0628). In the segmentation map (above) each pixel is associated with its corresponding H II region. The fluxes are recovered by summing the contributions from all pixels assigned to each H II region. As an example, the H II region identified with the number 200 in the catalogue is highlighted in red.

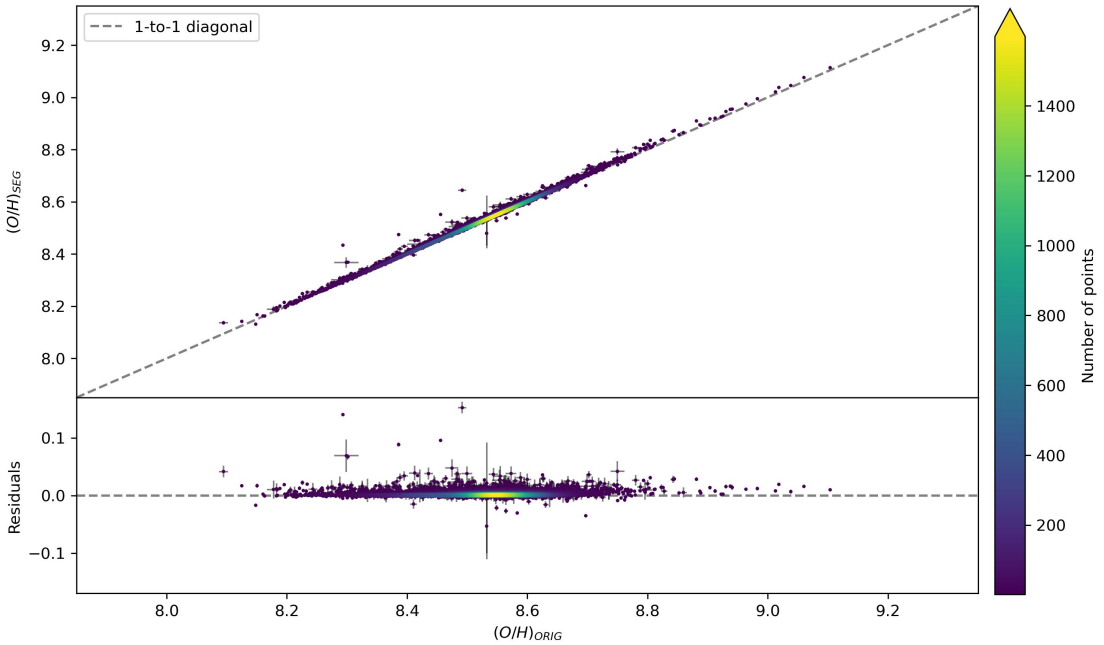

Figure 5.2: Scatter plot comparing the metallicity measurements obtained from the catalogue fluxes and those obtained from the segmentation maps. The x-axis represents the metallicity derived from the catalogue, labeled as $(O/H)_{ORIG}$, while the y-axis represents the metallicity obtained from the segmentation maps, labeled as $(O/H)_{SEGM}$. The dashed grey line represents the 1-to-1 diagonal. The difference is generally under 0.05 dex, with an average scatter of 0.005 dex.

slight discrepancies due to the higher S/N ratio of the spectra in the catalogue.

To address this issue and to check for self-consistency, we re-estimated the original line fluxes by using the segmentation maps provided with the catalogue. These maps associate each pixel with its corresponding H II region. The fluxes of the emission lines were recovered by summing the contributions from all pixels assigned to each H II region (the process is shown in Figure 5.1). We then recalculated the metallicity based on these updated fluxes.

The comparison between the metallicity derived from the catalog fluxes, labeled as $(O/H)_{ORIG}$, and the metallicity estimated from the segmentation fluxes, labeled as $(O/H)_{SEGM}$, is presented in Figure 5.2. In this figure, it is evident that the metallicity values obtained from both methods are in close agreement, with differences generally remaining below 0.05 dex.

Table 5.1: Coefficients of the linear fit ($y = Ax + B$) of the sample of data derived from the circular aperture, shown in Figure 5.3, along with the weighted scattering of the data points with respect to the 1-to-1 diagonal, labelled σ.

Diameters pc	A	B dex	σ dex
300.0	1.021 ± 0.002	-0.18 ± 0.01	0.033
200.0	1.028 ± 0.001	-0.23 ± 0.01	0.026
150.0	1.036 ± 0.001	-0.30 ± 0.01	0.019
100.0	1.049 ± 0.001	-0.41 ± 0.01	0.012
50.0	1.059 ± 0.002	-0.49 ± 0.02	0.016
20.0	1.072 ± 0.003	-0.60 ± 0.02	0.025

Table 5.2: Coefficients of the linear fit ($y = Ax + B$) of the sample of data derived from the rectangular aperture, shown in Figure 5.4, along with the weighted scattering of the data points with respect to the 1-to-1 diagonal, labelled σ.

Widths pc	A	B dex	σ dex
300.0	1.009 ± 0.001	-0.08 ± 0.01	0.027
200.0	1.0108 ± 0.0008	-0.092 ± 0.007	0.023
150.0	1.0137 ± 0.0008	-0.115 ± 0.006	0.015
100.0	1.0181 ± 0.0008	-0.151 ± 0.007	0.010
50.0	1.0214 ± 0.0009	-0.177 ± 0.008	0.012
20.0	1.022 ± 0.001	-0.18 ± 0.01	0.013

5.2 Results

The results of this analysis are illustrated in Figures 5.3 and 5.4, which provide a comparison between the metallicity measurements estimated using segmentation maps and those obtained from aperture simulations. In these plots, the x-axis represents the metallicity derived from the segmentation maps, labeled as $(O/H)_{SEGM}$, while the y-axis represents the metallicity obtained from the simulations, labeled as $(O/H)_{SIM}$. As in the previous analysis, the dashed grey line represents the 1-to-1 diagonal, serving as a reference point that indicates perfect agreement between the two sets of measurements.

Figure 5.3 focuses on the results obtained with circular apertures. The data indicate that larger aperture sizes achieve the best alignment with the 1-to-1 diagonal; however, this is accompanied by a higher scatter of points. In contrast, intermediate aperture sizes (e.g., 100 pc) offer a better balance between alignment

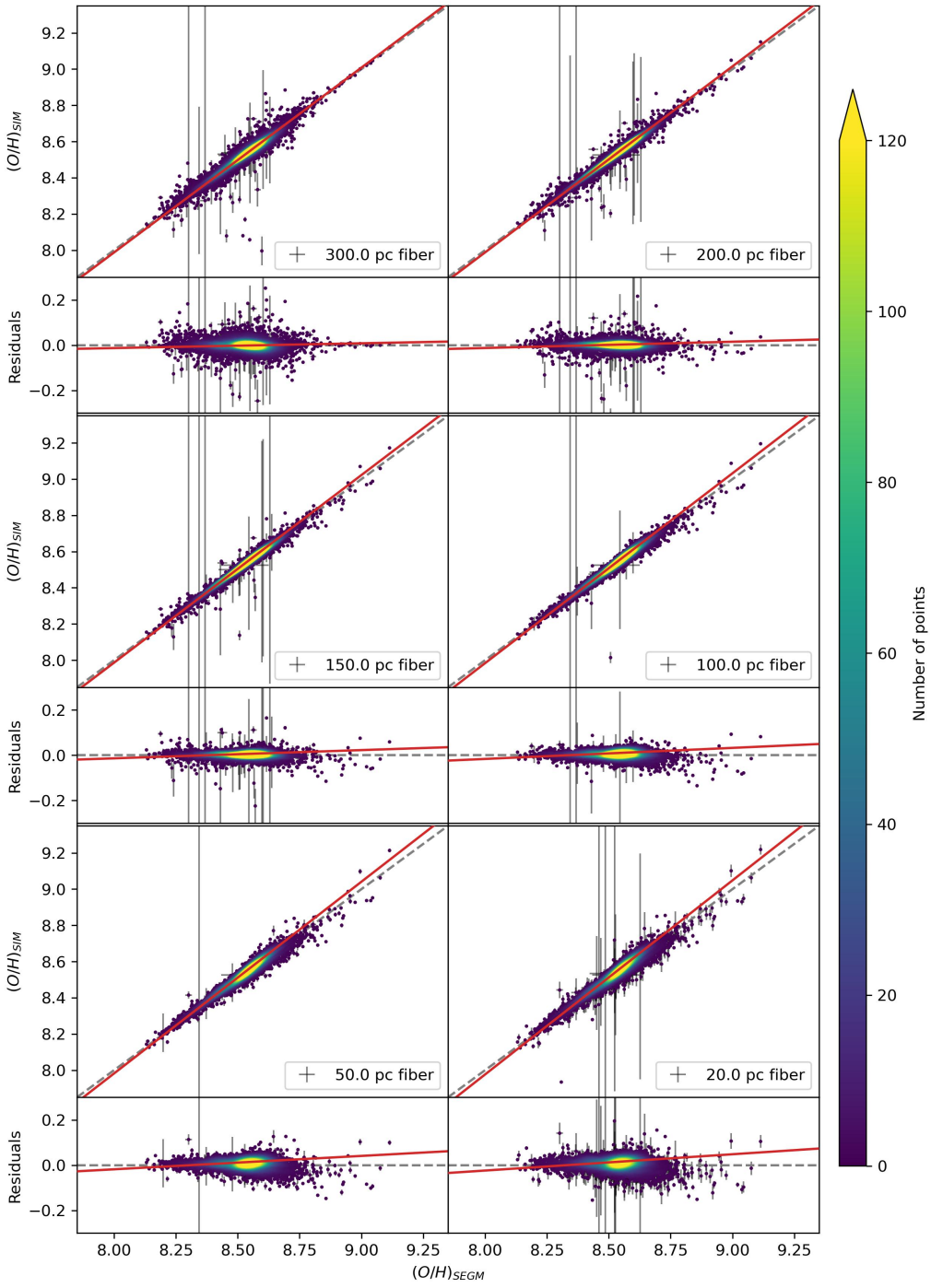

Figure 5.3: Scatter plot comparing the metallicity measurements obtained from the segmentation maps and those obtained from the simulations of circular apertures. The x-axis represents the metallicity derived from the segmentation maps, labeled as $(O/H)_{SEGM}$, while the y-axis represents the metallicity obtained from the simulations, labeled as $(O/H)_{SIM}$. The dashed grey line represents the 1-to-1 diagonal. The red line is the linear fit of the sample (the coefficients are reported in Table 5.1).

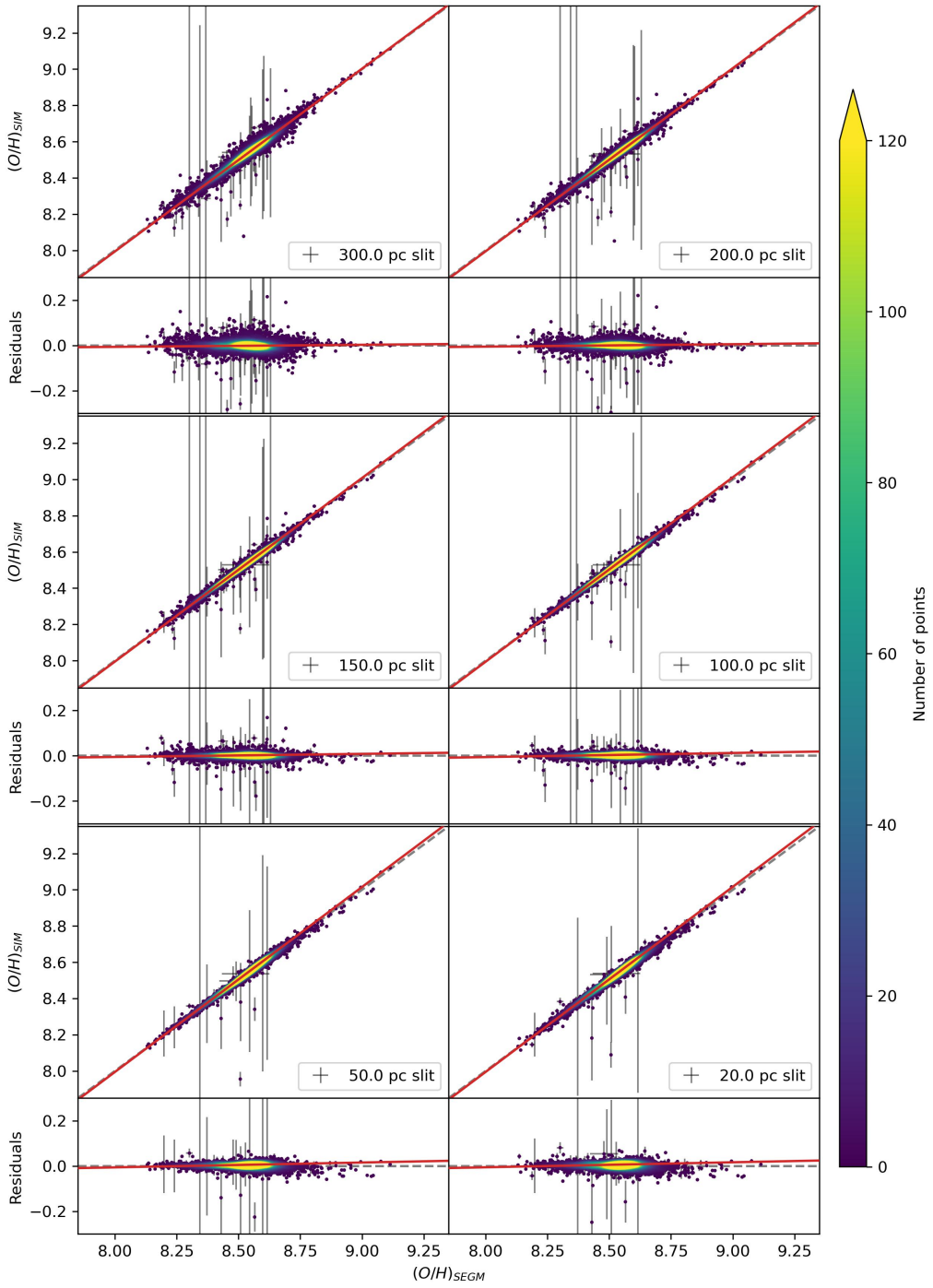

Figure 5.4: As Figure 5.3 but with the metallicity measurements obtained from the simulations of rectangular apertures, instead of circular ones (the coefficients are reported in Table 5.2).

and scatter.

At both smaller and larger aperture sizes, the data exhibit greater scatter. For the smallest apertures, the increased scatter may be due to the fact that only the central part of the H II region is captured, leading to inaccurate metallicity estimates. Additionally, in some galaxies, the smallest apertures fall below the resolution limit, introducing another potential source of error. On the other hand, the larger apertures tend to encompass multiple H II regions, which results in an averaging effect that smooths out the variations in metallicity, causing the data to deviate from the diagonal line. This trend is particularly evident when the sample is separated by galaxy, as shown in Figure 5.5 for NGC0628.

Figure 5.4 presents the results for rectangular slits, where the scatter appears to be less pronounced compared to the circular apertures. This reduced scatter might be attributed to the fact that the length of the rectangular slit was adjusted to match the size of the nebula, thereby minimizing the loss of spatial information. As a result, the rectangular slits provide a more accurate representation of the metallicity across the nebula, reducing the impact of the slit dimensions on the overall measurement accuracy.

However, when examining the larger rectangular apertures, a significant trend becomes apparent when the sample is separated by galaxy, like for NGC0628 (Figure 5.6). The data points for these larger apertures increasingly deviate from the diagonal line, reinforcing the idea that including multiple H II regions within a single aperture leads to an averaging of the metallicity values. This averaging effect, while less pronounced in rectangular slits compared to circular apertures, still introduces a systematic bias that must be considered when interpreting the results.

In summary, this analysis highlights that the aperture size has a modest but notable effect on the estimation of metallicity, potentially introducing a bias in the results. Unfortunately, there does not appear to be a specific aperture size where this bias becomes negligible or is entirely absent. Instead, the impact of aperture size on metallicity estimation is highly dependent on the resolution of the data. This resolution, in turn, is influenced by both the distance of the galaxy being observed and the quality of the seeing conditions during the observations.

Table 5.3: Coefficients of the linear fit ($y = Ax + B$) of the sample of data derived from the circular aperture restricted to the galaxy NGC0628, shown in Figure 5.5, along with the weighted scattering of the data points with respect to the 1-to-1 diagonal, labelled σ.

Diameters pc	A	B dex	σ dex
300.0	0.90 ± 0.02	0.9 ± 0.1	0.032
200.0	0.947 ± 0.009	0.45 ± 0.08	0.025
150.0	0.986 ± 0.006	0.12 ± 0.05	0.014
100.0	1.035 ± 0.006	-0.29 ± 0.05	0.007
50.0	1.062 ± 0.009	-0.51 ± 0.08	0.012
20.0	1.05 ± 0.01	-0.38 ± 0.09	0.017

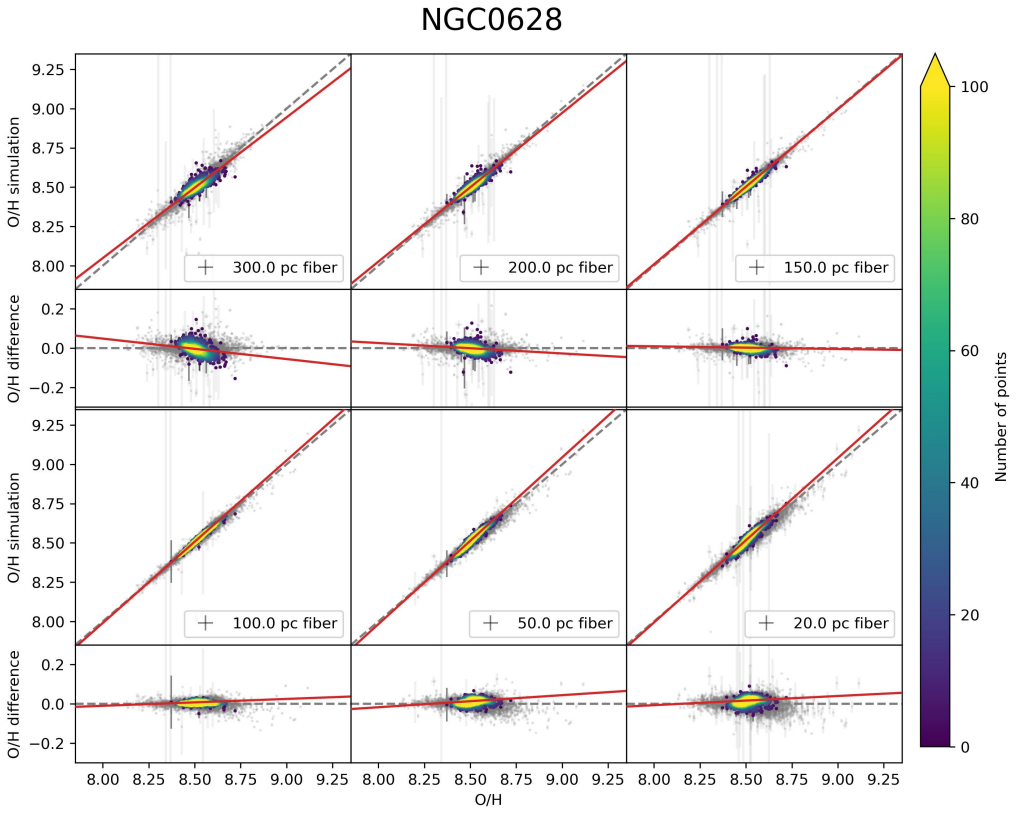

Figure 5.5: As Figure 5.3 but only for galaxy NGC0628. The sample includes 852 objects out of the 10,993 total. The full sample of data is plotted in gray for comparison. The red line is the linear fit of the sample (the coefficients are reported in Table 5.3).

Table 5.4: Coefficients of the linear fit ($y = Ax + B$) of the sample of data derived from the rectangular aperture restricted to the galaxy NGC0628, shown in Figure 5.6, along with the weighted scattering of the data points with respect to the 1-to-1 diagonal, labelled σ.

Widths pc	A	B dex	σ dex
300.0	0.92 ± 0.01	0.7 ± 0.1	0.029
200.0	0.942 ± 0.008	0.49 ± 0.07	0.019
150.0	0.964 ± 0.005	0.31 ± 0.04	0.010
100.0	0.995 ± 0.004	0.04 ± 0.03	0.006
50.0	1.024 ± 0.005	−0.19 ± 0.04	0.005
20.0	1.029 ± 0.006	−0.23 ± 0.05	0.010

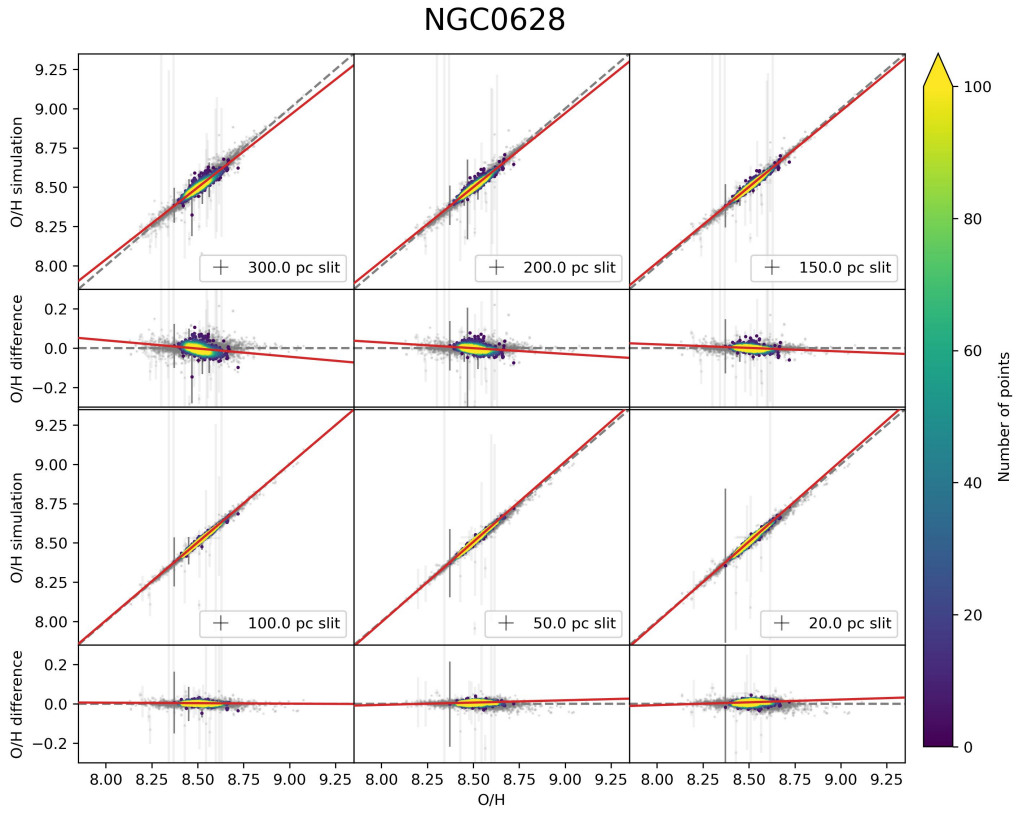

Figure 5.6: As Figure 5.4 but only for galaxy NGC0628. The sample includes 852 objects out of the 10,993 total. The full sample of data is plotted in gray for comparison. The red line is the linear fit of the sample (the coefficients are reported in Table 5.4).

6

Conclusions

This thesis investigates the challenges and biases associated with the measurement of metallicity in extragalactic H II regions using the SELs Method. Understanding the chemical composition of the ISM is vital in astrophysics, as metallicity directly impacts the evolution of stars, galaxies, and the universe. Metallicity is primarily measured through the oxygen-to-hydrogen ratio, which serves as a proxy for the overall metal content. However, the methods for determining this ratio, particularly the SELs Method, are prone to various observational biases.

This work focuses on examining these potential biases using the PHANGS–MUSE Nebular Catalogue. This dataset comprises over 40,000 high-resolution spectra of extragalactic nebulae across 19 galaxies, allowing for a detailed investigation of two primary sources of bias: (1) the influence of the DIG on metallicity estimates and (2) the impact of varying aperture dimensions on the derived metallicities.

The study used the "BPT sample" from the PHANGS-MUSE Nebular Catalogue, which includes 10,993 H II regions, to assess the influence of DIG on metallicity estimates using the S-calibration method from Pilyugin and Grebel (2016). The results show that, after correcting for the DIG, there is no systematic bias in metallicity measurements. The DIG-corrected metallicity values align closely with the original metallicity measurements, which are derived from total fluxes. A linear fit to the data produces a slope of 1.004 ± 0.001 and an intercept of -0.03 ± 0.01, confirming that there is no significant offset between DIG-corrected and uncorrected values.

However, a notable scatter of ~ 0.15 dex is observed around the 1-to-1 line, which is comparable to the azimuthal variations in metallicity seen in several nearby galaxies. This scatter could arise from an intrinsic difference in metallicity between the DIG and the H II regions or uncertainties in the DIG correction process. Additionally, the scatter decreases when considering bright or high contrast regions, suggesting that only this type of regions should be used when studying complex metallicity variations within a galaxy. However, it is still possible to obtain average metallicities or radial trend using less bright and lower contrast regions, provided that the sample is large enough to average out the scatter.

When analyzing individual galaxies, most show no systematic trend between DIG-corrected and uncorrected metallicity values. Nonetheless, a few galaxies, such as NGC3627 and NGC4254, show more significant deviations from the diagonal, potentially due to specific local factors, such as AGN influence, which can alter the DIG's properties.

The study also investigates how different aperture sizes impact metallicity measurements. The results indicate that aperture dimensions significantly influence metallicity estimates, and the choice of aperture shape (circular or rectangular) also plays a role in the results.

- **Circular Apertures**: The analysis explored circular apertures of varying sizes, ranging from 20 pc to 300 pc in diameter. It was found that circular apertures with diameters around 100 pc provide the better balance between alignment to the 1-to-1 diagonal and scatter of points. At this aperture size, the data points cluster closely around the 1-to-1 diagonal, with a mean scatter under 0.10 dex, indicating minimal systematic deviations. Smaller circular apertures (e.g., 20 pc or 50 pc) tend to capture only the central parts of H II regions, missing peripheral areas and resulting in biased metallicity estimates. Larger apertures (e.g., 200 pc or 300 pc) can include multiple H II regions, leading to an averaging effect that smooths out variations and introduces deviations from the 1-to-1 line.

- **Rectangular Apertures**: Rectangular apertures were also analyzed with widths ranging from 20 pc to 300 pc, and their lengths were always adjusted to match the size of each nebula. These apertures showed less scatter compared to circular ones, as their adapted lengths provide a better fit for the nebulae, capturing the full extent of the H II regions without includ-

ing unrelated background or adjacent regions. However, even with this adjustment, when the rectangular slits are too large (e.g., 300 pc or 200 pc in width), they can still introduce a bias similar to the larger circular apertures due to averaging effects.

Combining the findings for both circular and rectangular aperture shapes, it is evident that the aperture size exerts a modest yet significant influence on the estimation of metallicity, which can introduce a bias into the results. Using circular apertures ~ 100 pc in diameter, or rectangular apertures with length tailored to the size of the nebulae and width of between 50 and 100 pc, offers the better balance between alignment and scatter of points, without significant systematic deviations. Larger apertures, whether circular or rectangular, tend to average out metallicity variations, while smaller apertures may miss important parts of H II regions, both resulting in inaccuracies. The choice between circular and rectangular apertures depends on the observational setup and the specific characteristics of the target H II regions.

6.1 Future Research Possibilities

While this thesis provides significant insights into the biases affecting SELs metallicity measurements, it also opens up avenues for future research. A promising direction involves conducting similar studies using alternative SELs calibrations to determine whether the identified biases are calibration-dependent or universally present. The current study relies on one of the calibrations established by Pilyugin and Grebel (2016), known as the "S" calibration. This calibration, along with the other "R" calibration presented in the same paper, was designed to provide accurate oxygen and nitrogen abundances across a wide range of metallicities. However, as the thesis discusses, no single calibration can at present perfectly capture the complexities of H II regions' metallicity measurements due to variations in physical conditions and ionization structures.

Future studies could explore other SELs calibrations, such as those developed by Kewley and Dopita (2002), Kobulnicky and Kewley (2004), and Marino et al. (2013). A comparative analysis across different calibrations would help identify whether certain calibrations are more prone to biases from DIG contamination or aperture effects. This could also reveal if there are calibration methods that are more robust for specific types of galaxies or H II regions.

In conclusion, while the study provides a valuable framework for understanding and mitigating biases in SELs metallicity measurements, the field remains ripe for further exploration. By examining alternative calibrations, testing for significant deviations, and expanding the scope of analysis to different galactic environments, future studies can build on the findings of this thesis and contribute to a more refined understanding of extragalactic metallicity measurements.

A

Atlas of nebulae

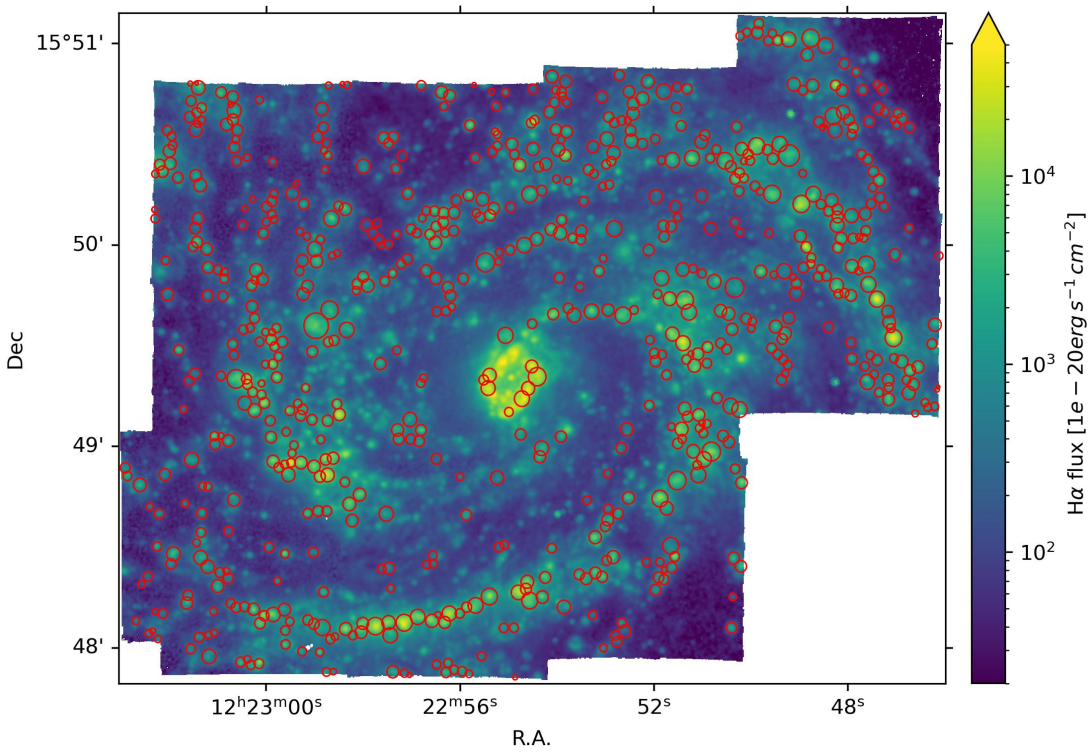

Figure A.1: Spatial distribution of the H II regions within the galaxy NGC4321, as selected in this work. The background image shows the Hα emission. The dimensions of the circles represent the sizes of the H II regions, as reported in the PHANGS-MUSE Nebular Catalogue.

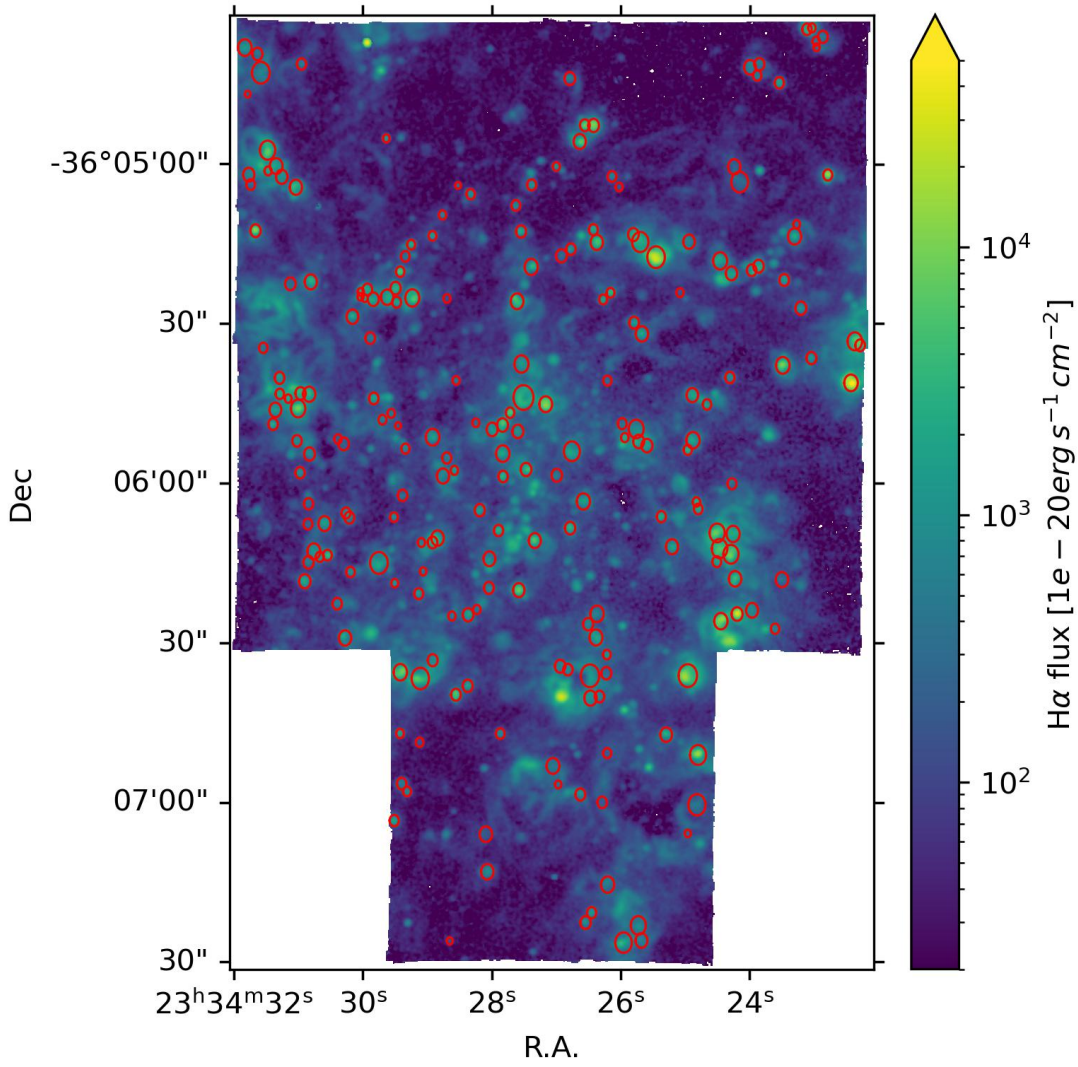

Figure A.2: Spatial distribution of the H II regions within the galaxy IC5332, as selected in this work. The background image shows the Hα emission. The dimensions of the circles represent the sizes of the H II regions, as reported in the PHANGS-MUSE Nebular Catalogue.

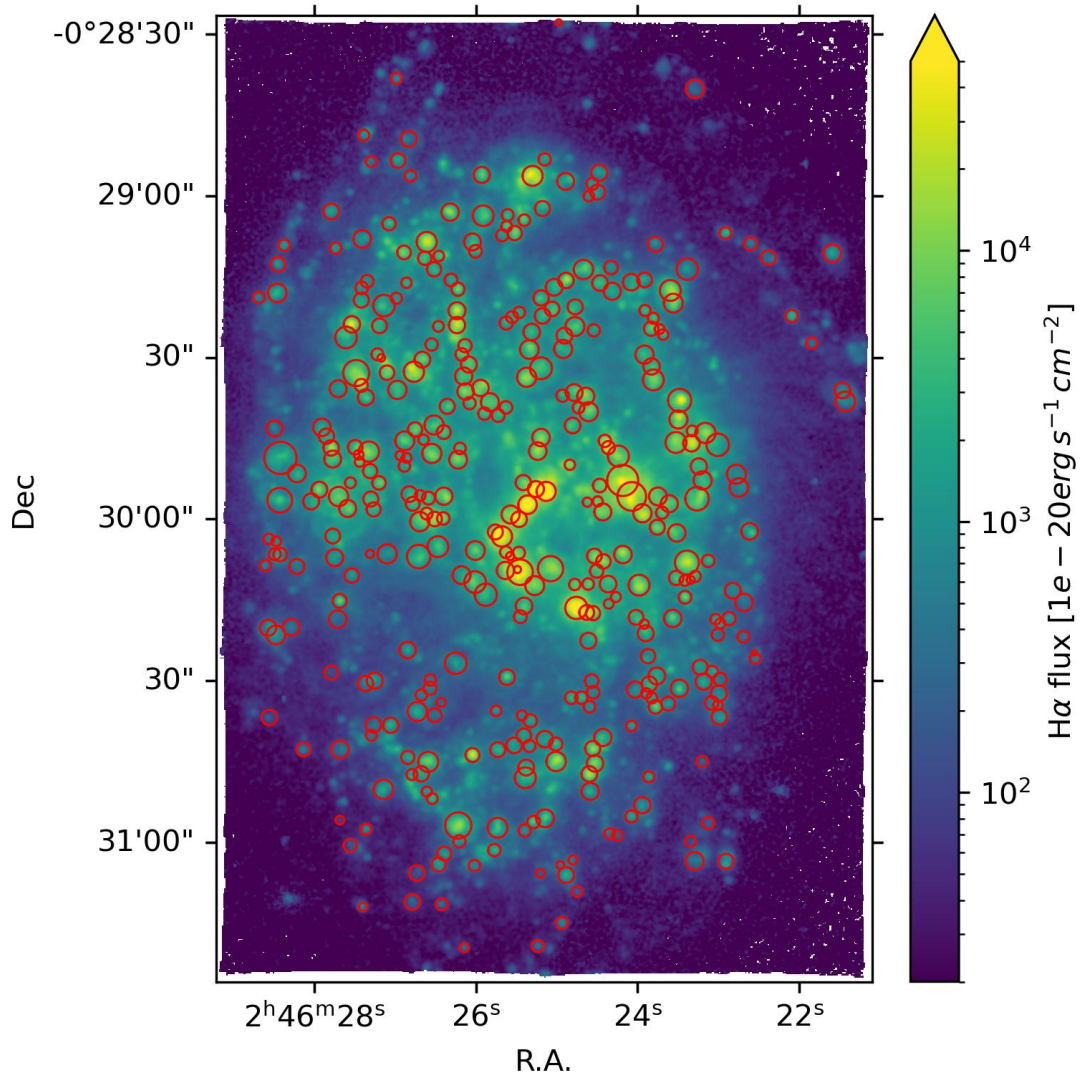

Figure A.3: Spatial distribution of the H II regions within the galaxy NGC1087, as selected in this work. The background image shows the Hα emission. The dimensions of the circles represent the sizes of the H II regions, as reported in the PHANGS-MUSE Nebular Catalogue.

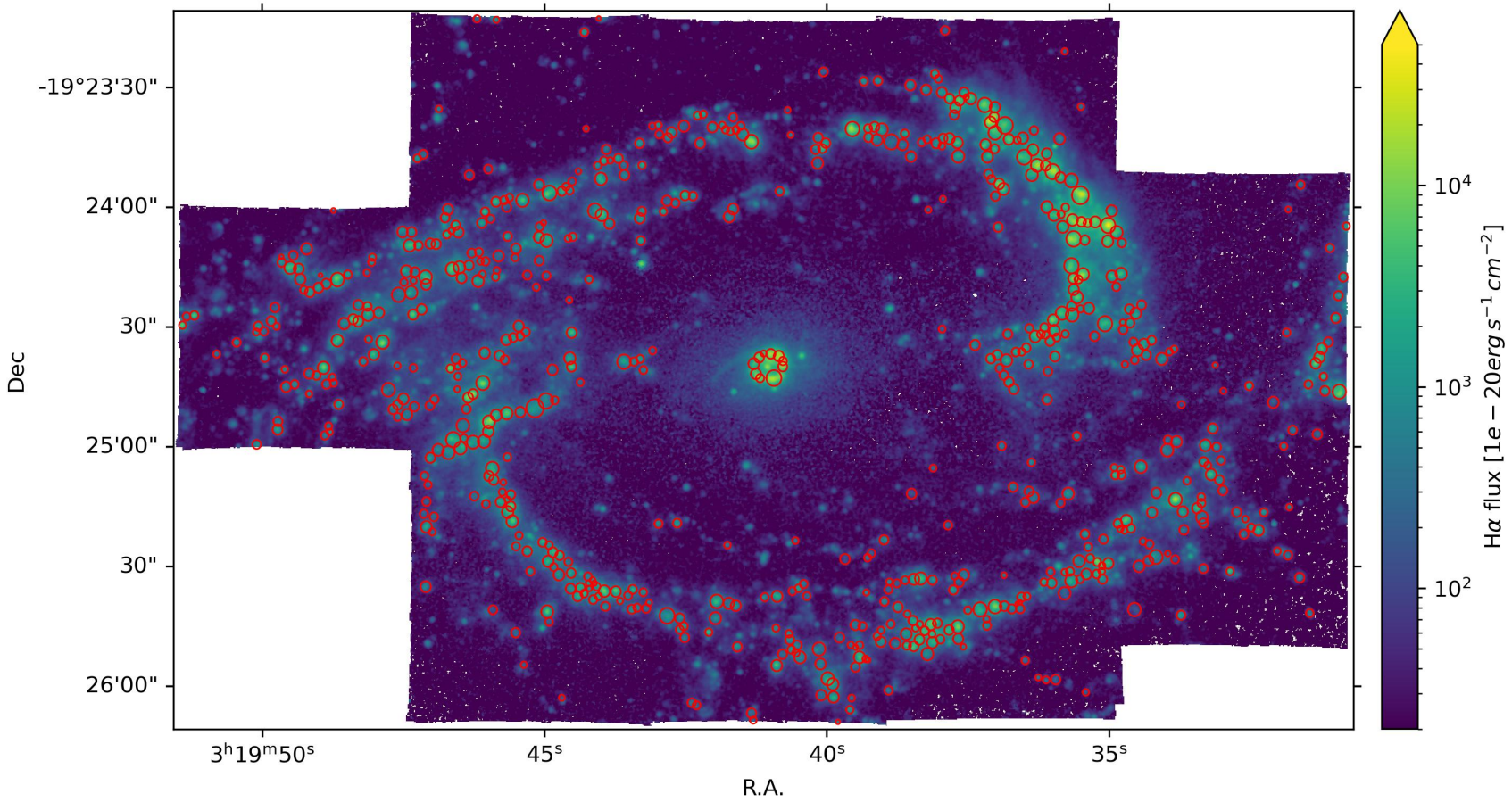

Figure A.4: Spatial distribution of the H II regions within the galaxy NGC1300, as selected in this work. The background image shows the Hα emission. The dimensions of the circles represent the sizes of the H II regions, as reported in the PHANGS-MUSE Nebular Catalogue.

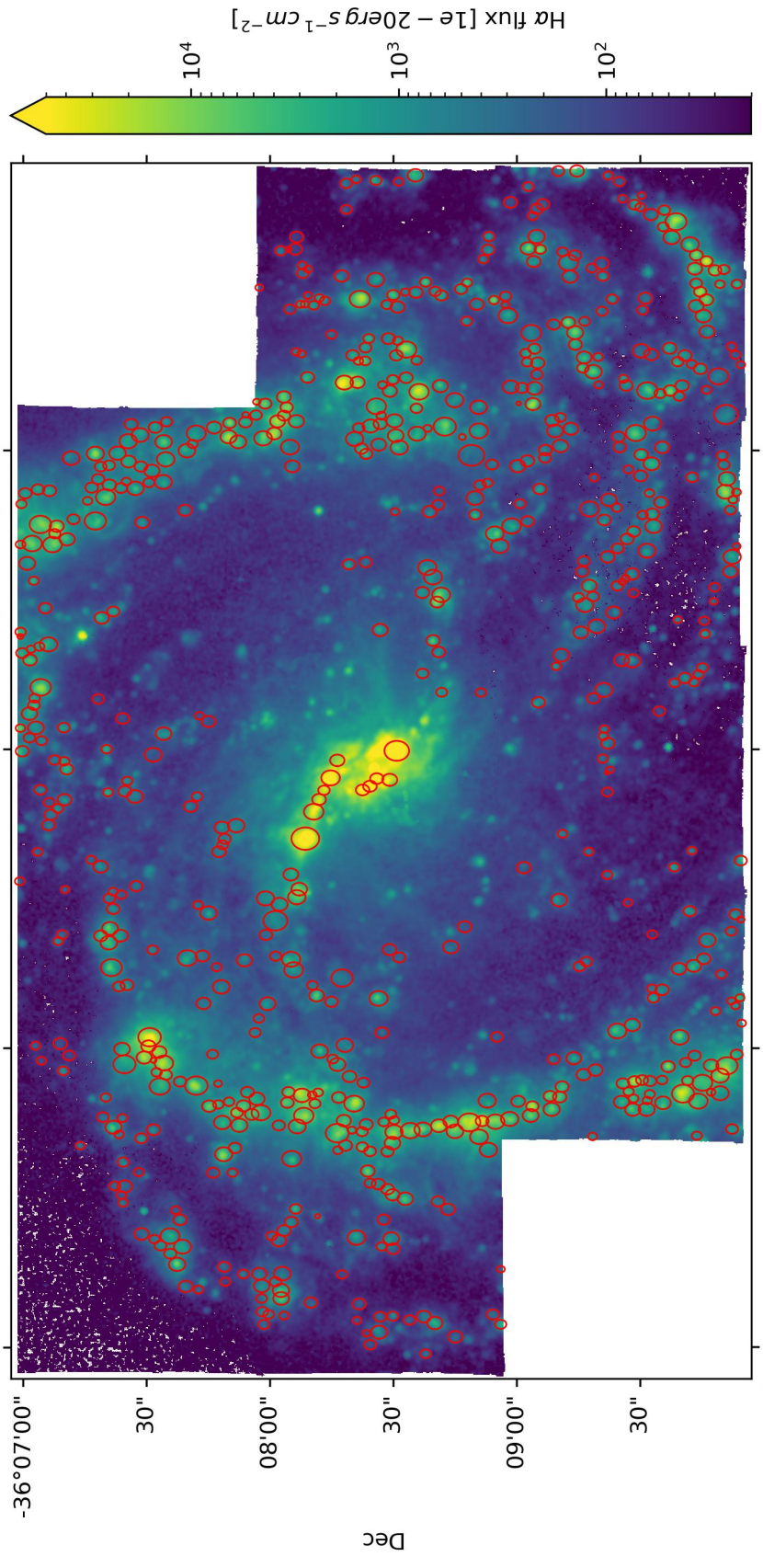

Figure A.5: Spatial distribution of the H II regions within the galaxy NGC1365, as selected in this work. The background image shows the Hα emission. The dimensions of the circles represent the sizes of the H II regions, as reported in the PHANGS-MUSE Nebular Catalogue.

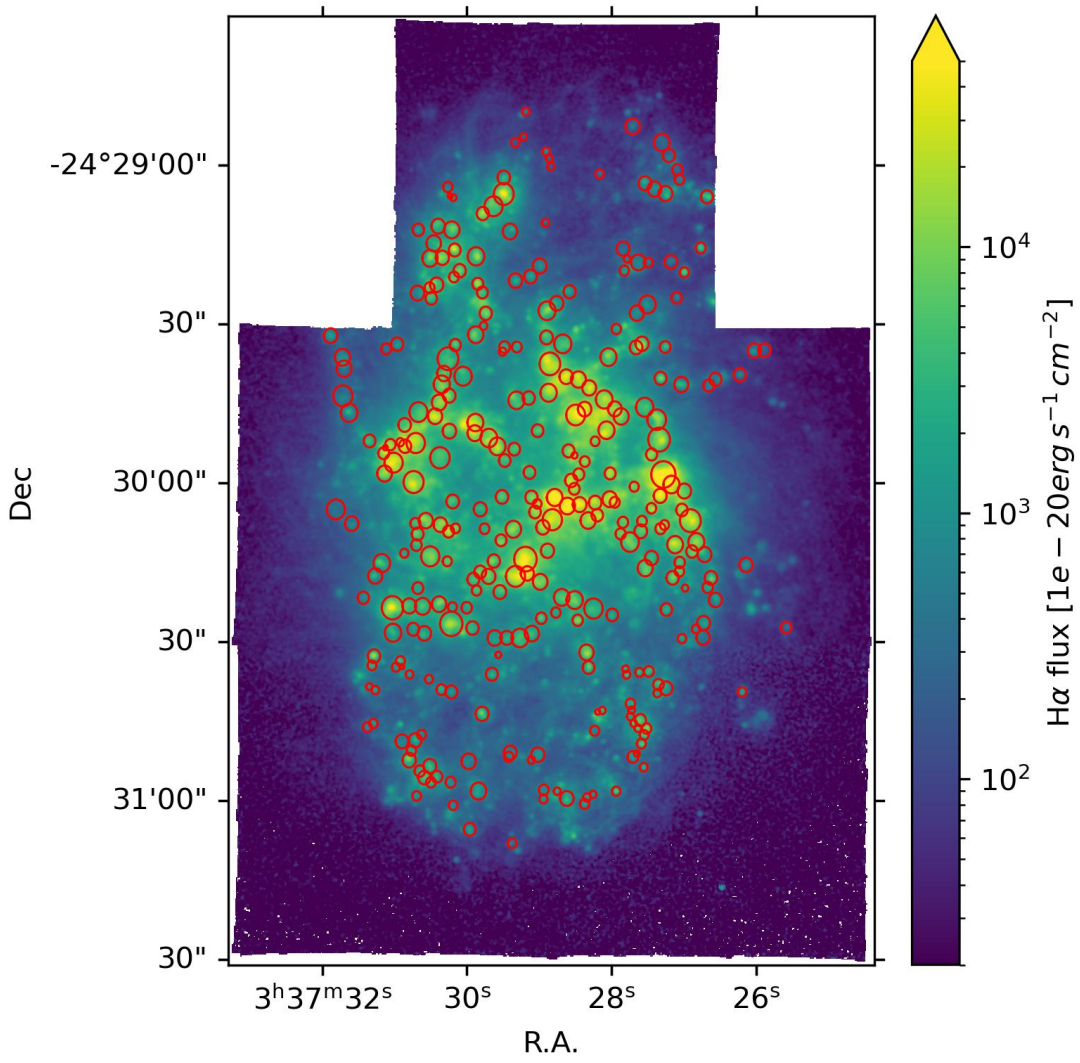

Figure A.6: Spatial distribution of the H II regions within the galaxy NGC1385, as selected in this work. The background image shows the Hα emission. The dimensions of the circles represent the sizes of the H II regions, as reported in the PHANGS-MUSE Nebular Catalogue.

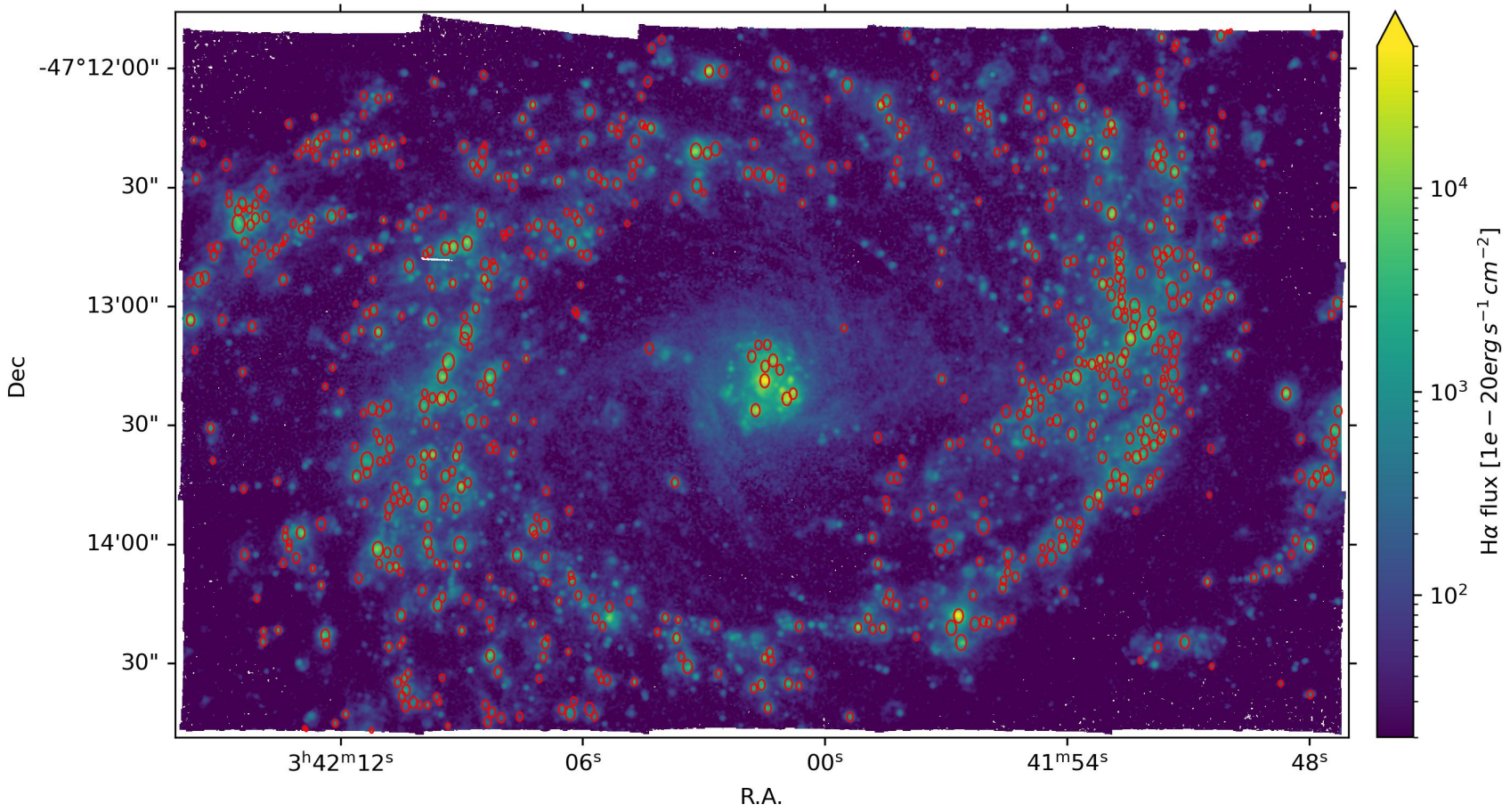

Figure A.7: Spatial distribution of the H II regions within the galaxy NGC1433, as selected in this work. The background image shows the Hα emission. The dimensions of the circles represent the sizes of the H II regions, as reported in the PHANGS-MUSE Nebular Catalogue.

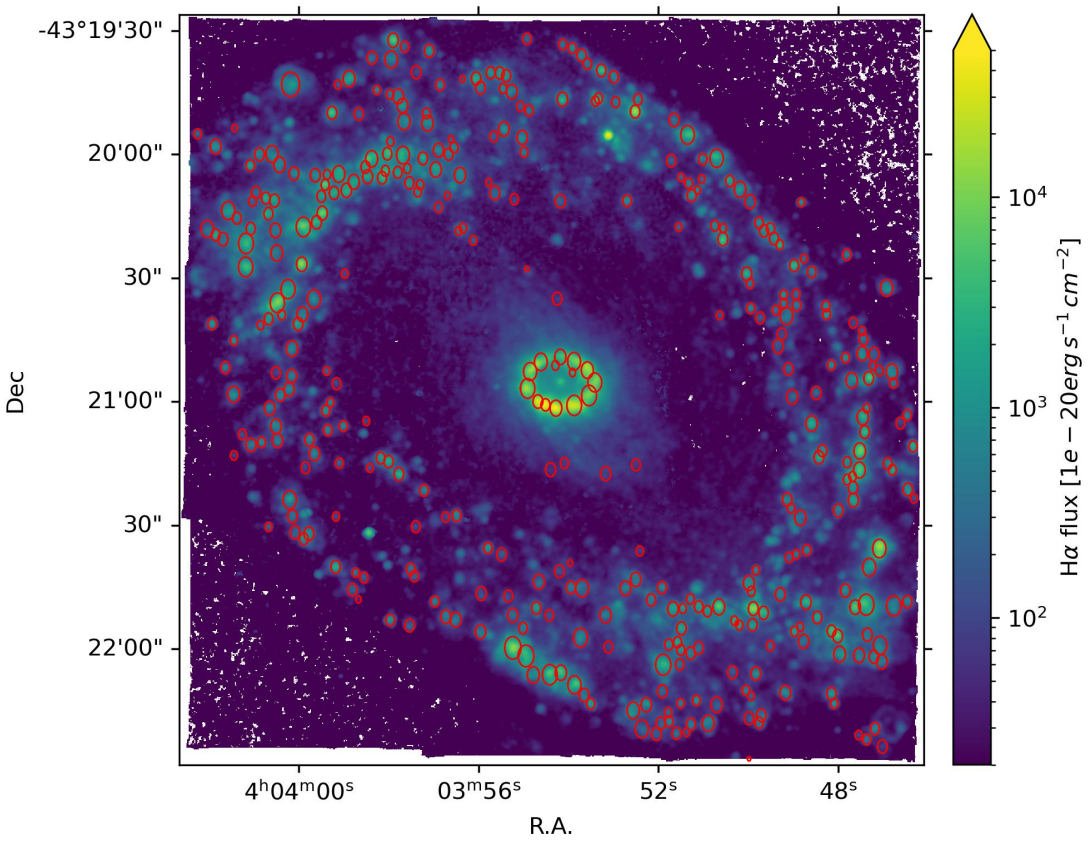

Figure A.8: Spatial distribution of the H II regions within the galaxy NGC1512, as selected in this work. The background image shows the Hα emission. The dimensions of the circles represent the sizes of the H II regions, as reported in the PHANGS-MUSE Nebular Catalogue.

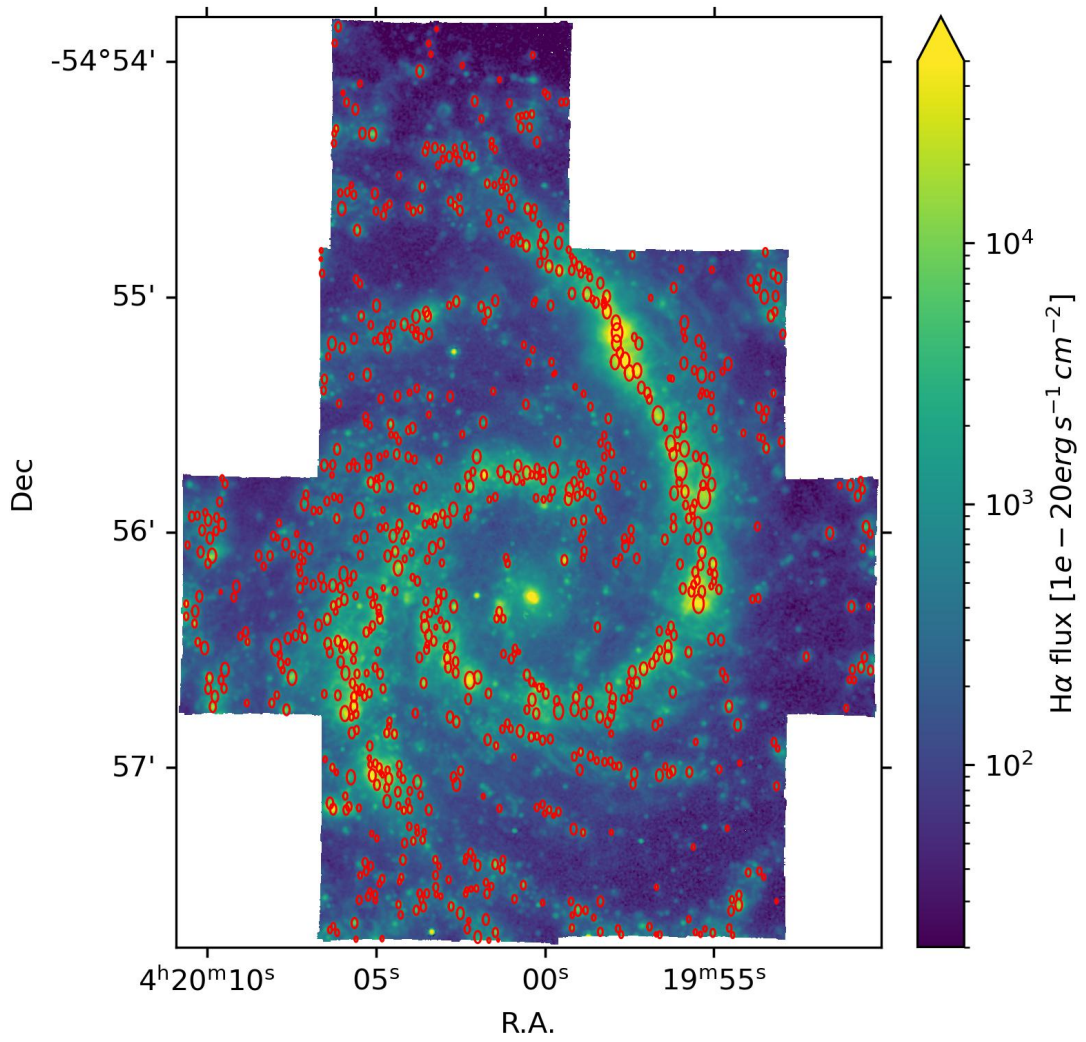

Figure A.9: Spatial distribution of the H II regions within the galaxy NGC1566, as selected in this work. The background image shows the Hα emission. The dimensions of the circles represent the sizes of the H II regions, as reported in the PHANGS-MUSE Nebular Catalogue.

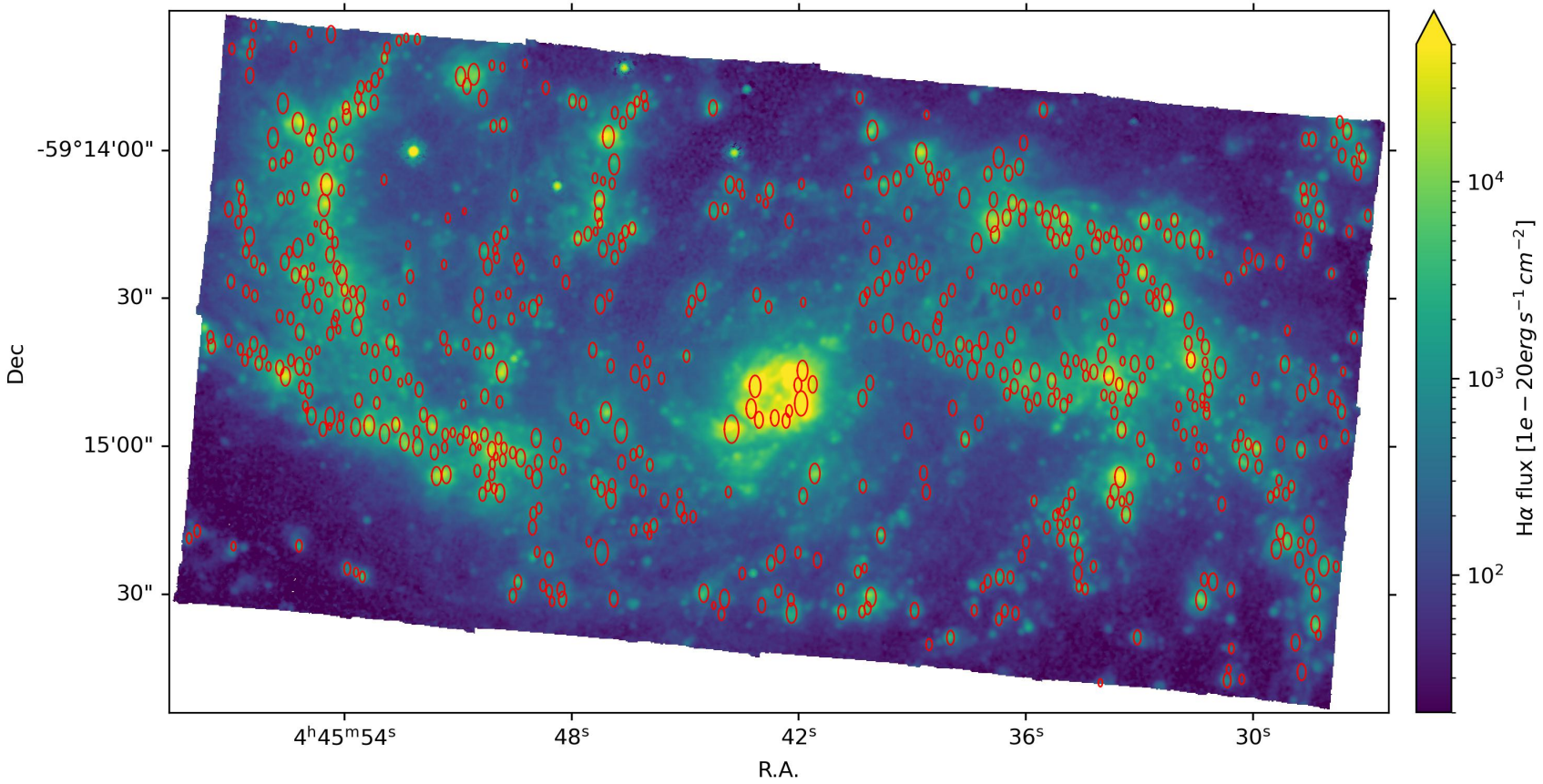

Figure A.10: Spatial distribution of the H II regions within the galaxy NGC1672, as selected in this work. The background image shows the Hα emission. The dimensions of the circles represent the sizes of the H II regions, as reported in the PHANGS-MUSE Nebular Catalogue.

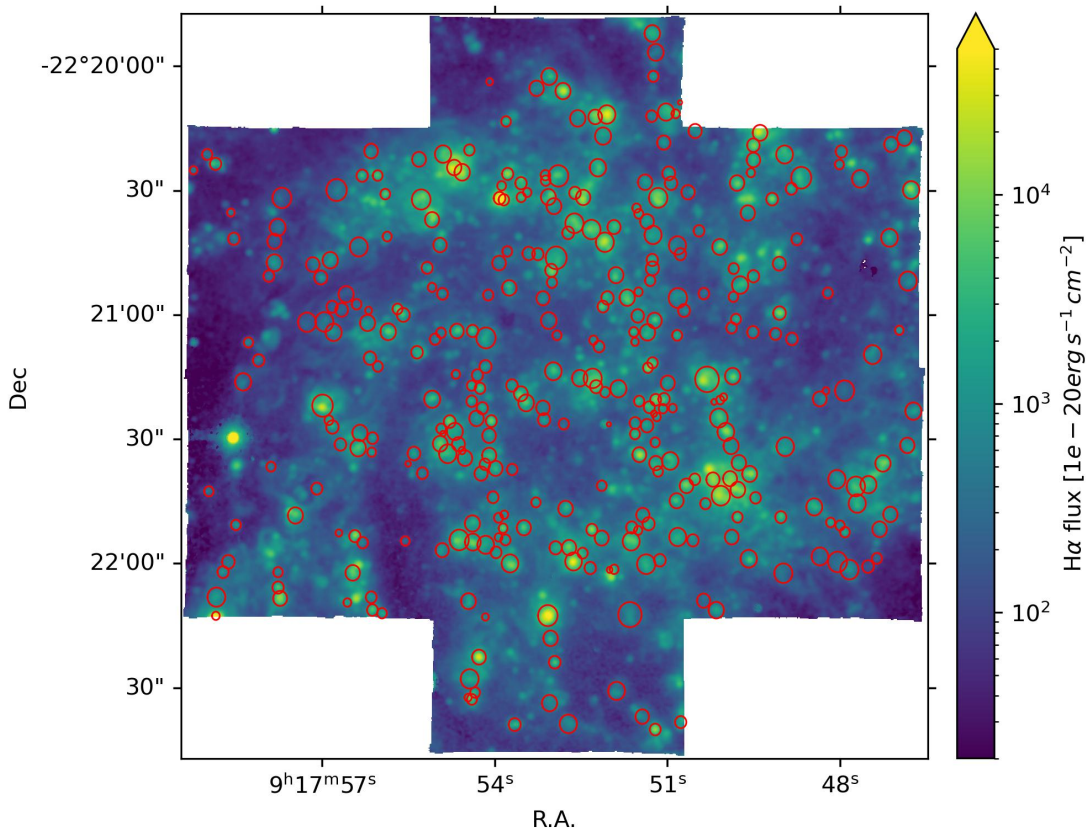

Figure A.11: Spatial distribution of the H II regions within the galaxy NGC2835, as selected in this work. The background image shows the Hα emission. The dimensions of the circles represent the sizes of the H II regions, as reported in the PHANGS-MUSE Nebular Catalogue.

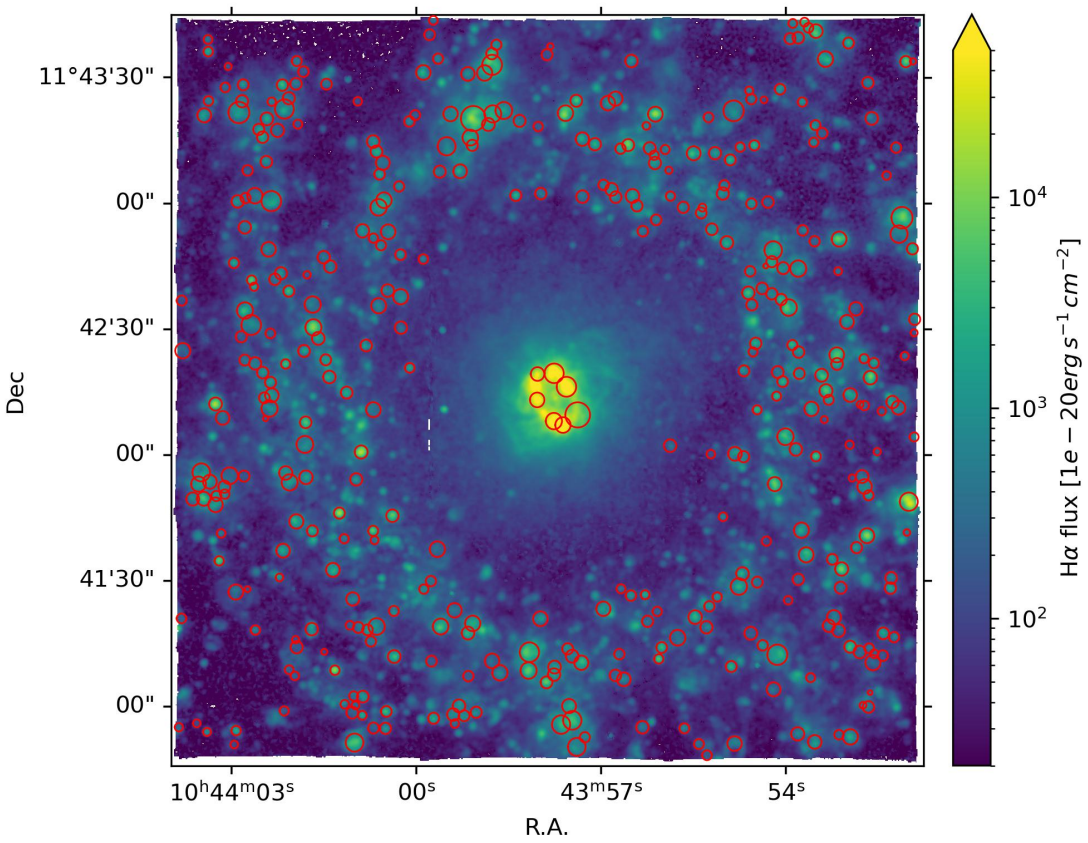

Figure A.12: Spatial distribution of the H II regions within the galaxy NGC3351, as selected in this work. The background image shows the Hα emission. The dimensions of the circles represent the sizes of the H II regions, as reported in the PHANGS-MUSE Nebular Catalogue.

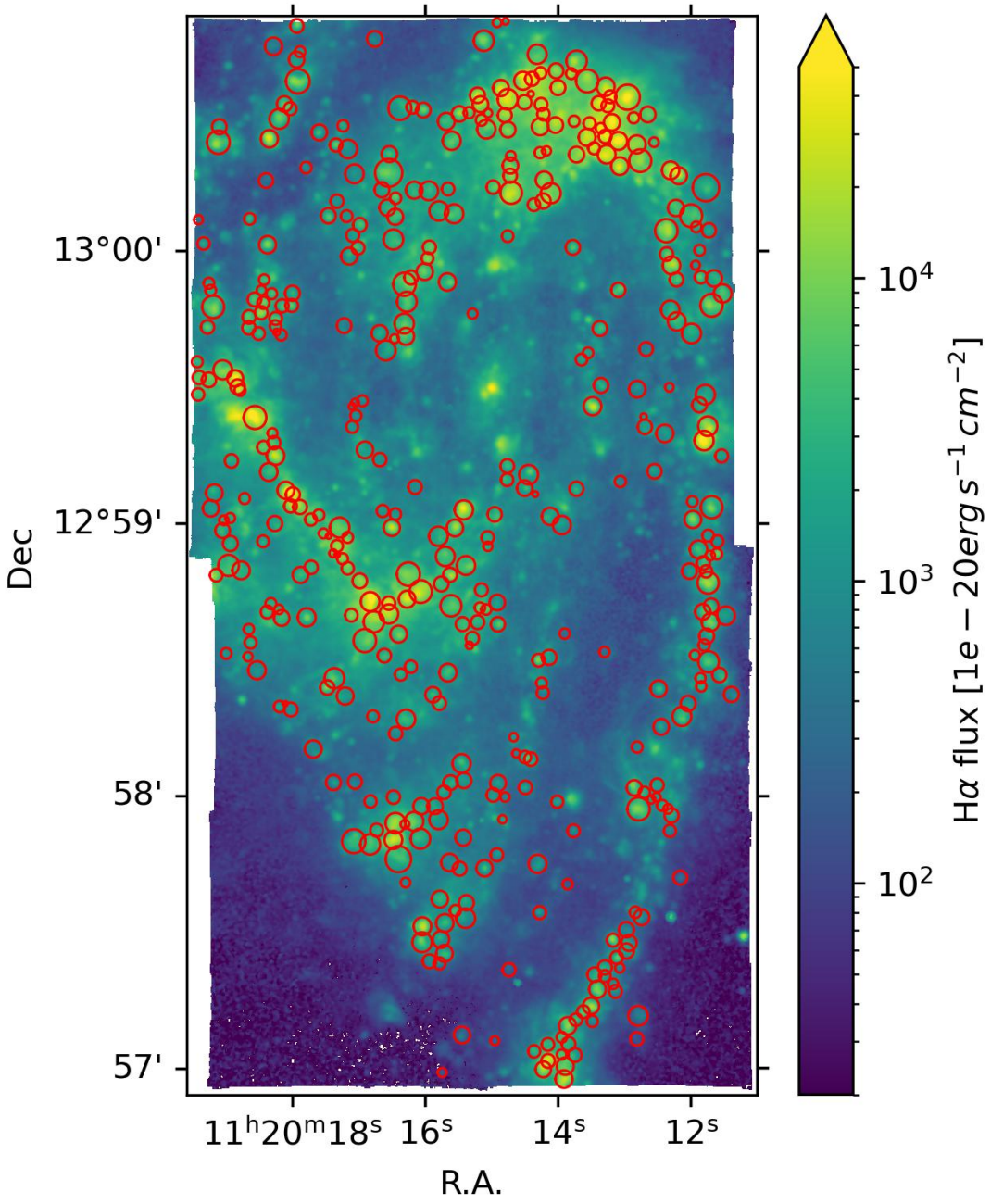

Figure A.13: Spatial distribution of the H II regions within the galaxy NGC3627, as selected in this work. The background image shows the Hα emission. The dimensions of the circles represent the sizes of the H II regions, as reported in the PHANGS-MUSE Nebular Catalogue.

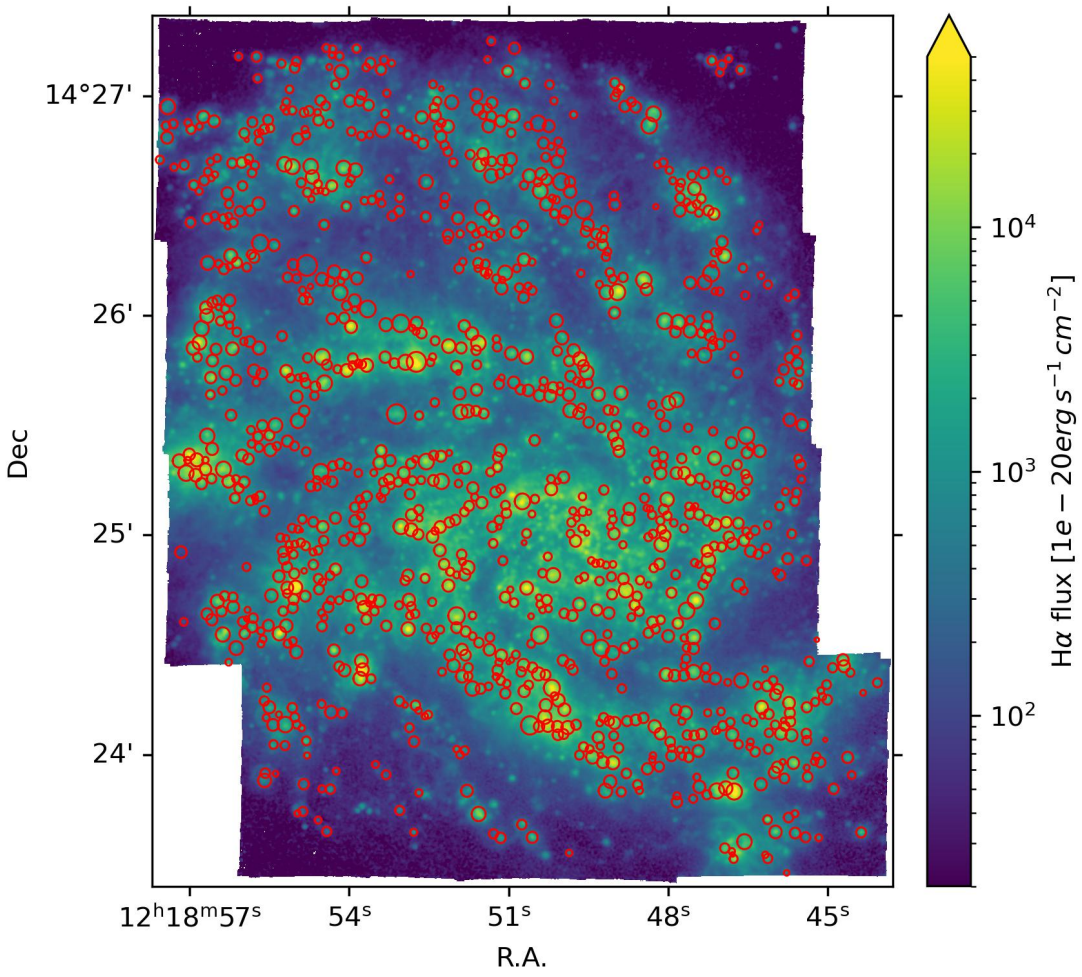

Figure A.14: Spatial distribution of the H II regions within the galaxy NGC4254, as selected in this work. The background image shows the Hα emission. The dimensions of the circles represent the sizes of the H II regions, as reported in the PHANGS-MUSE Nebular Catalogue.

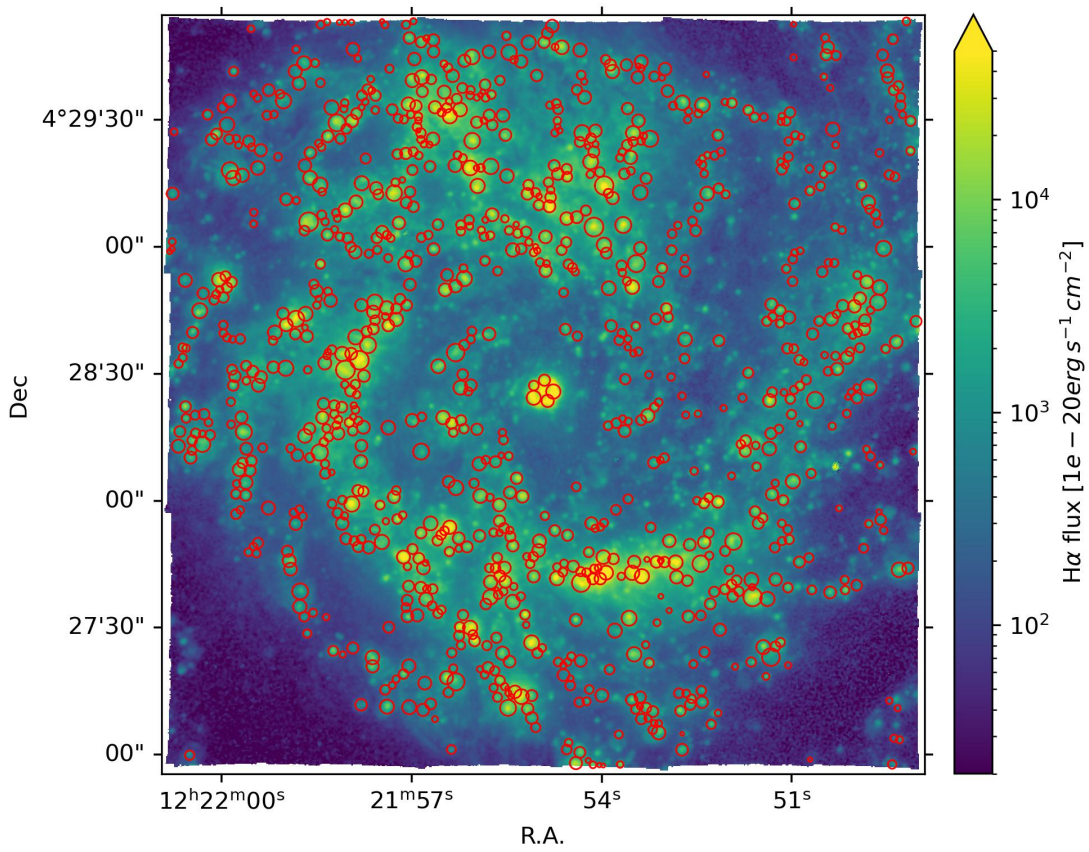

Figure A.15: Spatial distribution of the H II regions within the galaxy NGC4303, as selected in this work. The background image shows the Hα emission. The dimensions of the circles represent the sizes of the H II regions, as reported in the PHANGS-MUSE Nebular Catalogue.

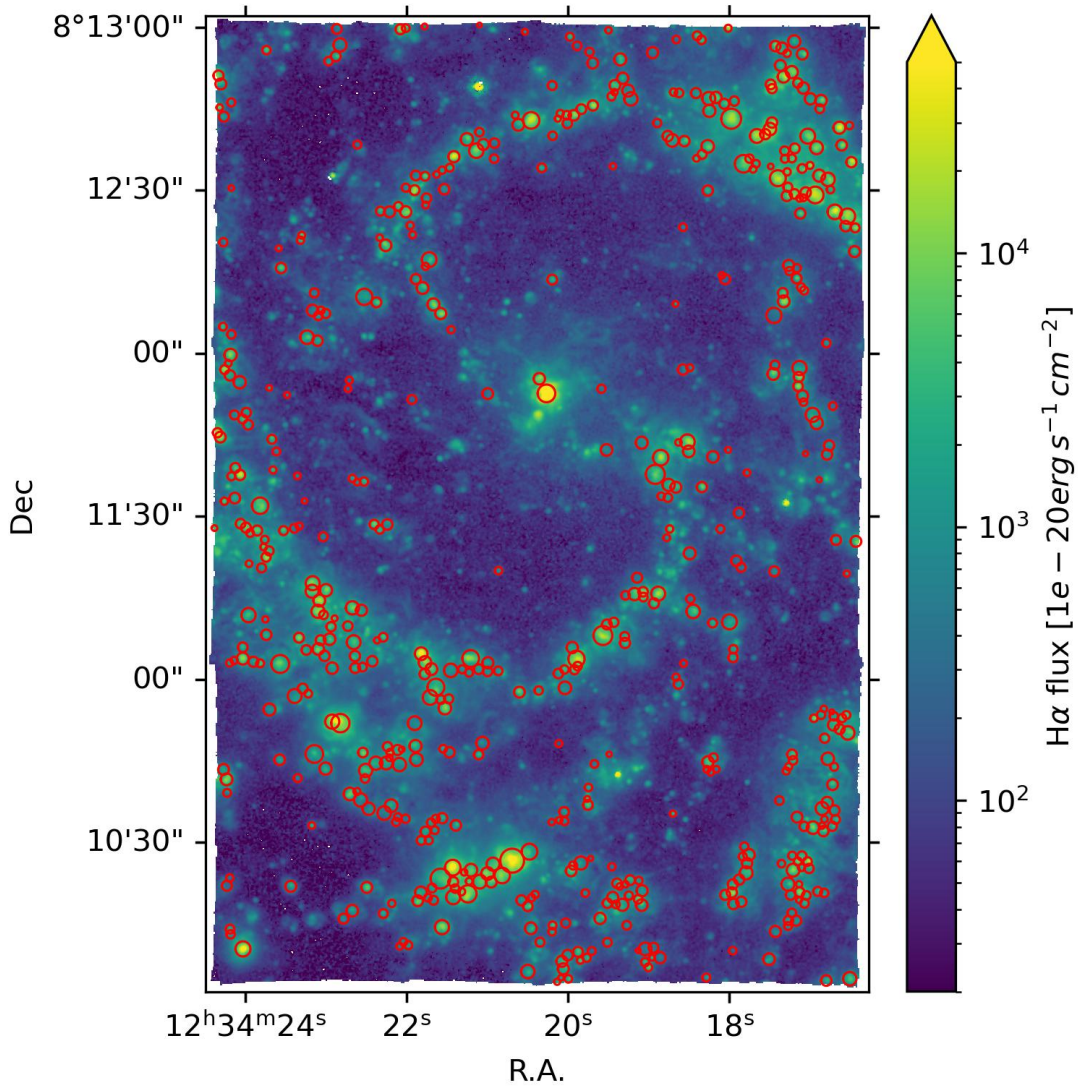

Figure A.16: Spatial distribution of the H II regions within the galaxy NGC4535, as selected in this work. The background image shows the Hα emission. The dimensions of the circles represent the sizes of the H II regions, as reported in the PHANGS-MUSE Nebular Catalogue.

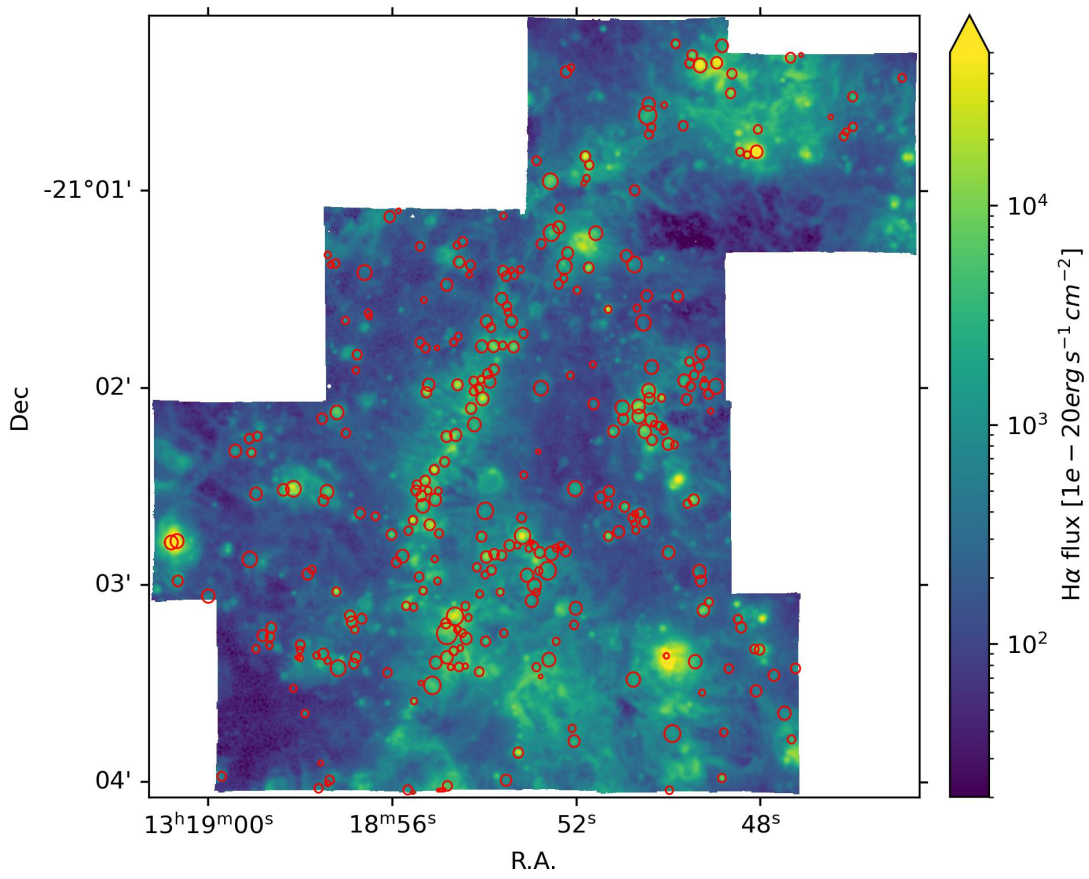

Figure A.17: Spatial distribution of the H II regions within the galaxy NGC5068, as selected in this work. The background image shows the Hα emission. The dimensions of the circles represent the sizes of the H II regions, as reported in the PHANGS-MUSE Nebular Catalogue.

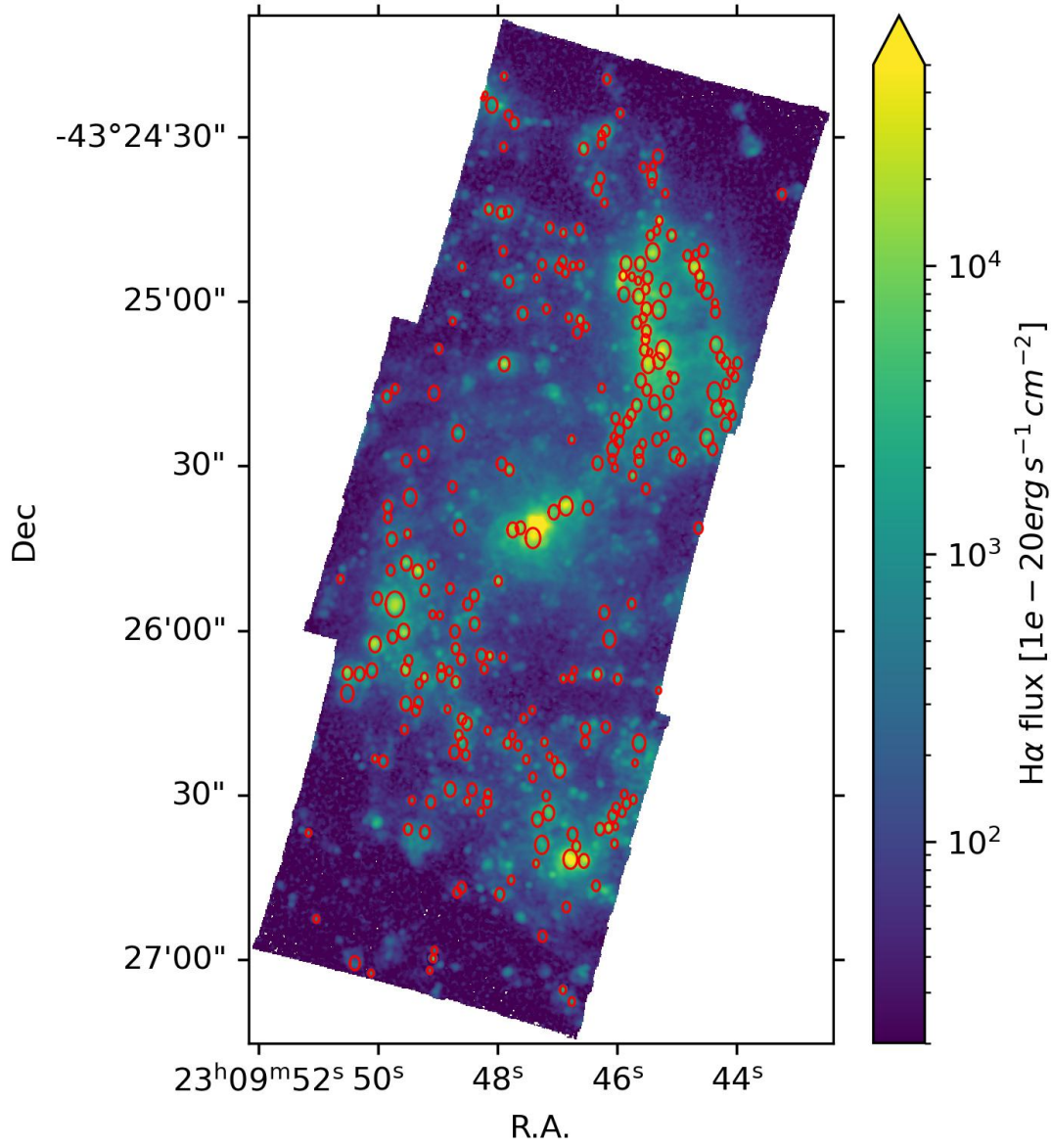

Figure A.18: Spatial distribution of the H II regions within the galaxy NGC7496, as selected in this work. The background image shows the Hα emission. The dimensions of the circles represent the sizes of the H II regions, as reported in the PHANGS-MUSE Nebular Catalogue.

B

Apertures' simulations by galaxy

In this appendix, we provide the detailed results of the aperture simulations conducted for each galaxy studied in this thesis.

For each galaxy, the same plots as in Figures 5.5 and 5.6 are presented, alongside the Tables summarizing the values for the linear fits and the scattering of the data points with respect to the 1-to-1 diagonal.

Table B.1: Coefficients of the linear fit ($y = Ax + B$) of the sample of data derived from the circular aperture restricted to the galaxy IC5332, shown in Figure B.1, along with the weighted scattering of the data points with respect to the 1-to-1 diagonal, labelled σ.

Diameters pc	A	B dex	σ dex
300.0	0.92 ± 0.02	0.6 ± 0.2	0.063
200.0	0.96 ± 0.01	0.4 ± 0.1	0.068
150.0	0.98 ± 0.01	0.15 ± 0.08	0.065
100.0	1.002 ± 0.008	−0.01 ± 0.06	0.030
50.0	1.00 ± 0.01	0.0 ± 0.1	0.012
20.0	1.00 ± 0.01	0.0 ± 0.1	0.018

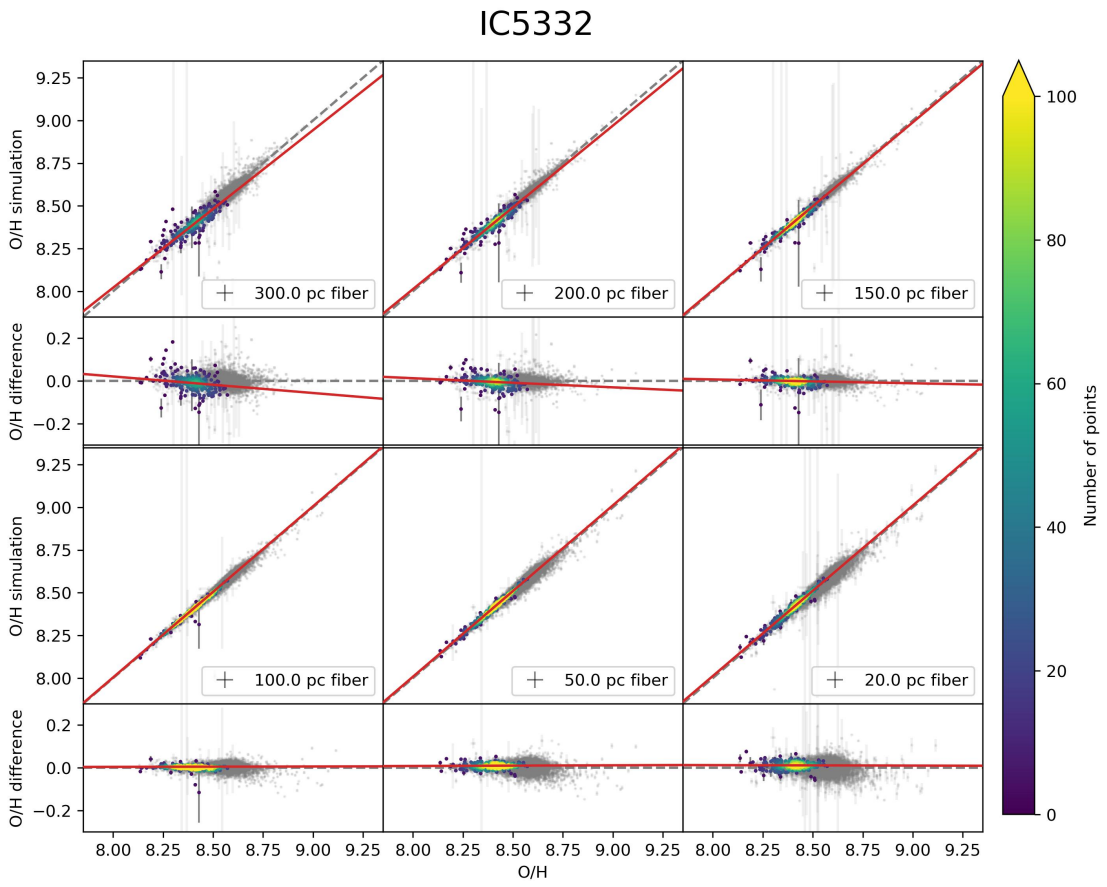

Figure B.1: As Figure 5.5 but for galaxy IC5332. The sample includes 222 objects out of the 10,993 total. The full sample of data is plotted in gray for comparison. The red line is the linear fit of the sample (the coefficients are reported in Table B.1).

Table B.2: Coefficients of the linear fit ($y = Ax + B$) of the sample of data derived from the rectangular aperture restricted to the galaxy IC5332, shown in Figure B.2, along with the weighted scattering of the data points with respect to the 1-to-1 diagonal, labelled σ.

Widths pc	A	B dex	σ dex
300.0	0.95 ± 0.02	0.4 ± 0.1	0.070
200.0	0.97 ± 0.01	0.28 ± 0.09	0.064
150.0	0.981 ± 0.008	0.16 ± 0.06	0.064
100.0	0.997 ± 0.006	0.02 ± 0.05	0.045
50.0	1.006 ± 0.006	-0.05 ± 0.05	0.030
20.0	1.006 ± 0.008	-0.04 ± 0.07	0.065

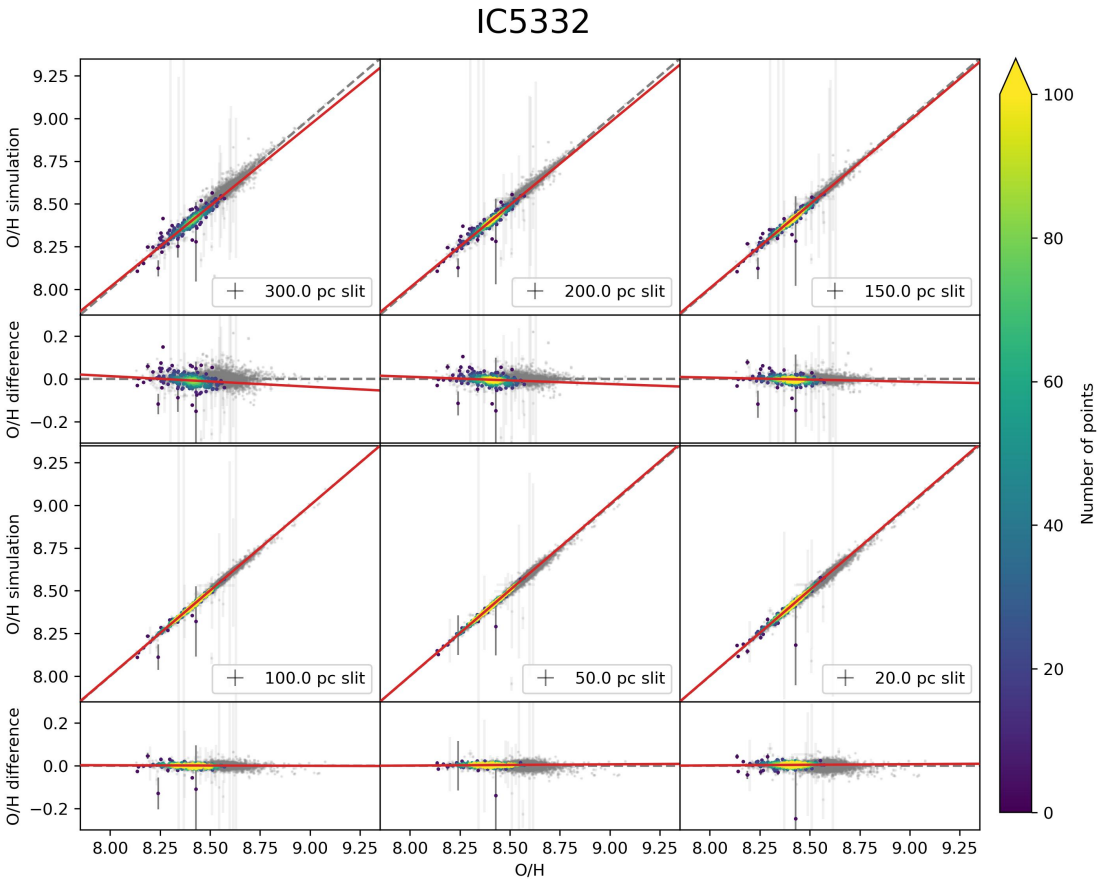

Figure B.2: As Figure 5.6 but for galaxy IC5332. The sample includes 222 objects out of the 10,993 total. The full sample of data is plotted in gray for comparison. The red line is the linear fit of the sample (the coefficients are reported in Table B.2).

Table B.3: Coefficients of the linear fit ($y = Ax + B$) of the sample of data derived from the circular aperture restricted to the galaxy NGC1087, shown in Figure B.3, along with the weighted scattering of the data points with respect to the 1-to-1 diagonal, labelled σ.

Diameters pc	A	B dex	σ dex
300.0	1.025 ± 0.008	−0.21 ± 0.07	0.027
200.0	1.057 ± 0.007	−0.47 ± 0.06	0.014
150.0	1.078 ± 0.008	−0.65 ± 0.07	0.005
100.0	1.10 ± 0.01	−0.80 ± 0.08	0.006
50.0	1.10 ± 0.01	−0.9 ± 0.1	0.011
20.0	1.10 ± 0.01	−0.9 ± 0.1	0.019

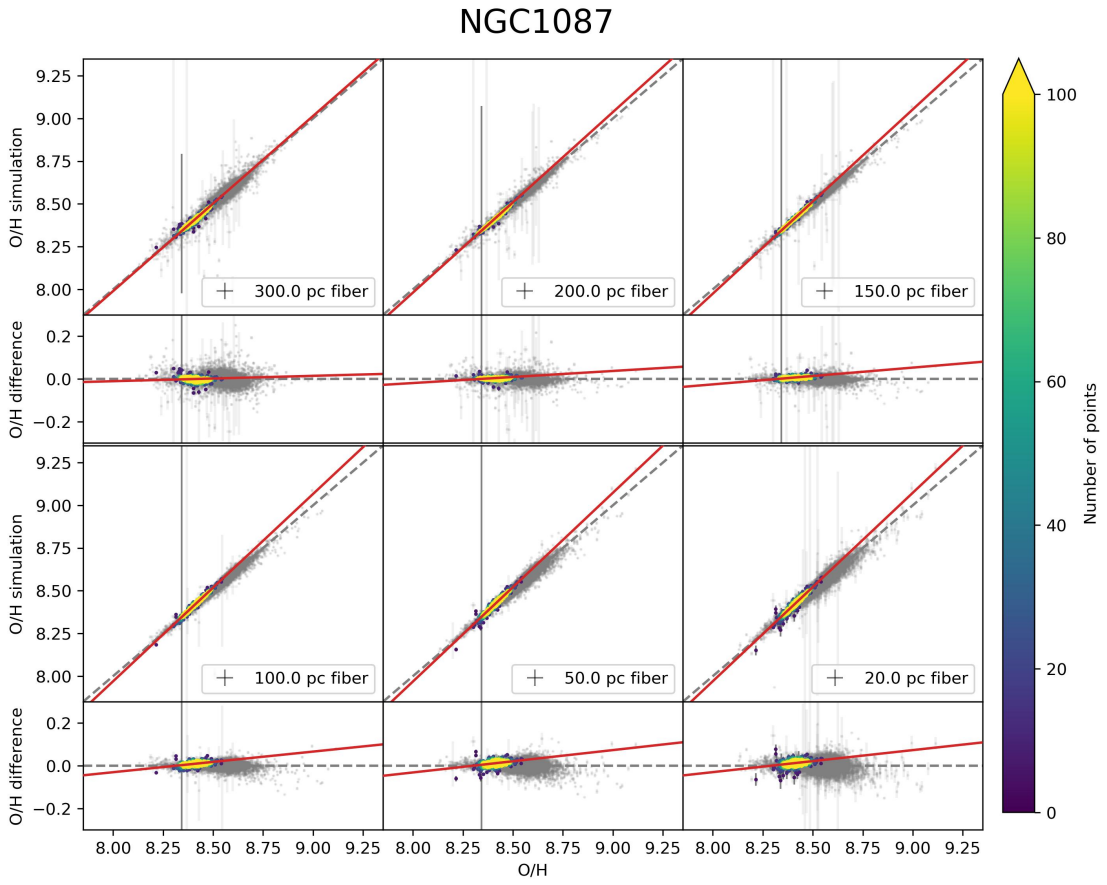

Figure B.3: As Figure 5.5 but for galaxy NGC1087. The sample includes 372 objects out of the 10,993 total. The full sample of data is plotted in gray for comparison. The red line is the linear fit of the sample (the coefficients are reported in Table B.3).

Table B.4: Coefficients of the linear fit ($y = Ax + B$) of the sample of data derived from the rectangular aperture restricted to the galaxy NGC1087, shown in Figure B.4, along with the weighted scattering of the data points with respect to the 1-to-1 diagonal, labelled σ.

Widths pc	A	B dex	σ dex
300.0	0.998 ± 0.006	0.02 ± 0.05	0.004
200.0	1.025 ± 0.004	-0.21 ± 0.04	0.014
150.0	1.038 ± 0.004	-0.32 ± 0.04	0.011
100.0	1.045 ± 0.005	-0.38 ± 0.05	0.001
50.0	1.047 ± 0.007	-0.39 ± 0.06	0.014
20.0	1.045 ± 0.008	-0.38 ± 0.07	0.009

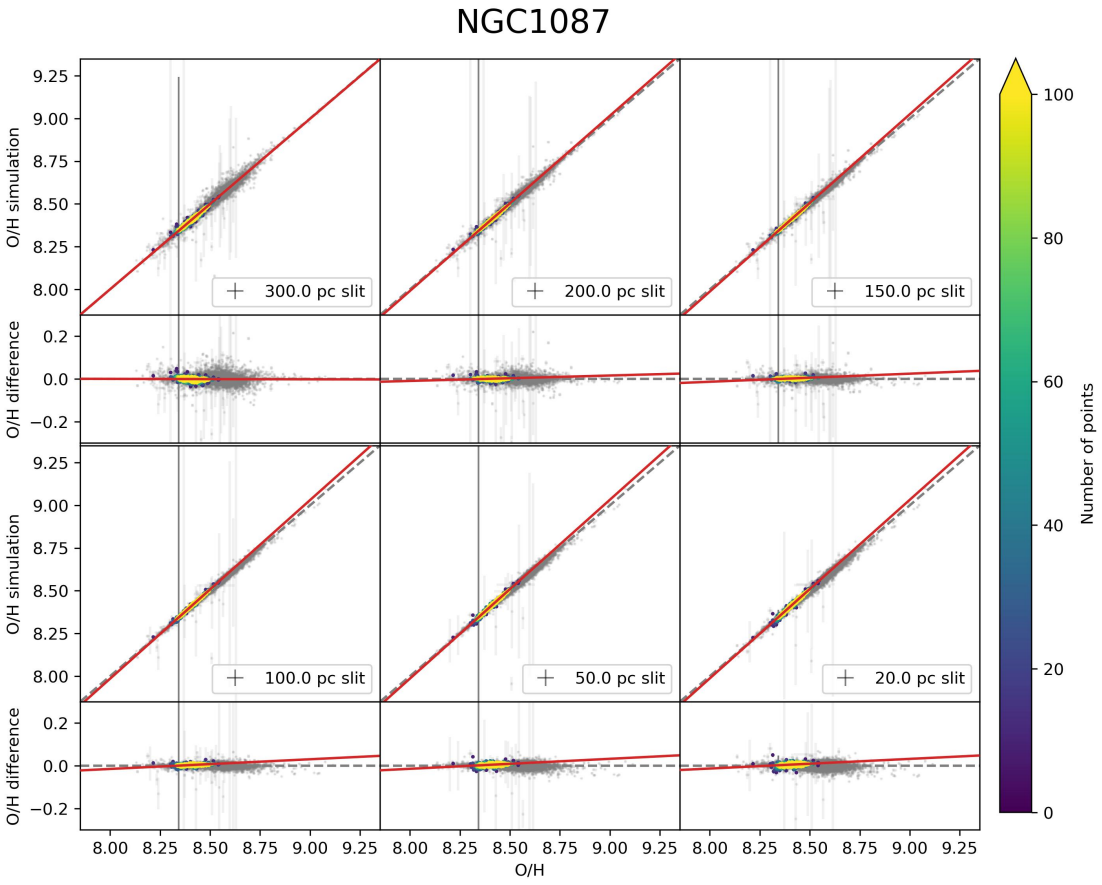

Figure B.4: As Figure 5.6 but for galaxy NGC1087. The sample includes 372 objects out of the 10,993 total. The full sample of data is plotted in gray for comparison. The red line is the linear fit of the sample (the coefficients are reported in Table B.4).

Table B.5: Coefficients of the linear fit ($y = Ax + B$) of the sample of data derived from the circular aperture restricted to the galaxy NGC1300, shown in Figure B.5, along with the weighted scattering of the data points with respect to the 1-to-1 diagonal, labelled σ.

Diameters pc	A	B dex	σ dex
300.0	0.984 ± 0.008	0.13 ± 0.07	0.017
200.0	1.037 ± 0.007	−0.31 ± 0.06	0.005
150.0	1.072 ± 0.009	−0.61 ± 0.08	0.006
100.0	1.10 ± 0.01	−0.8 ± 0.1	0.011
50.0	1.09 ± 0.01	−0.8 ± 0.1	0.016
20.0	1.08 ± 0.01	−0.7 ± 0.1	0.017

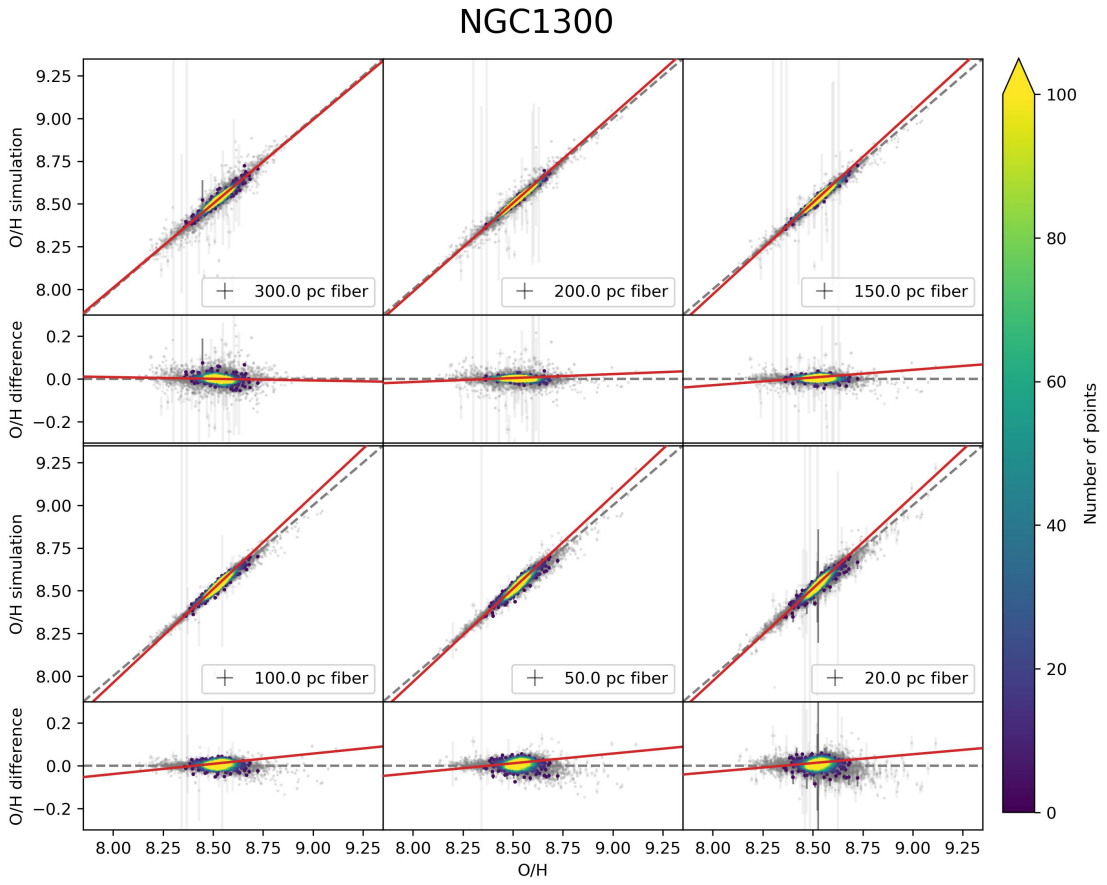

Figure B.5: As Figure 5.5 but for galaxy NGC1300. The sample includes 681 objects out of the 10,993 total. The full sample of data is plotted in gray for comparison. The red line is the linear fit of the sample (the coefficients are reported in Table B.5).

Table B.6: Coefficients of the linear fit ($y = Ax + B$) of the sample of data derived from the rectangular aperture restricted to the galaxy NGC1300, shown in Figure B.6, along with the weighted scattering of the data points with respect to the 1-to-1 diagonal, labelled σ.

Widths pc	A	B dex	σ dex
300.0	0.977 ± 0.006	0.19 ± 0.05	0.010
200.0	1.001 ± 0.005	-0.01 ± 0.04	0.006
150.0	1.019 ± 0.005	-0.16 ± 0.04	0.004
100.0	1.040 ± 0.007	-0.33 ± 0.06	0.005
50.0	1.052 ± 0.008	-0.43 ± 0.07	0.008
20.0	1.048 ± 0.008	-0.40 ± 0.07	0.009

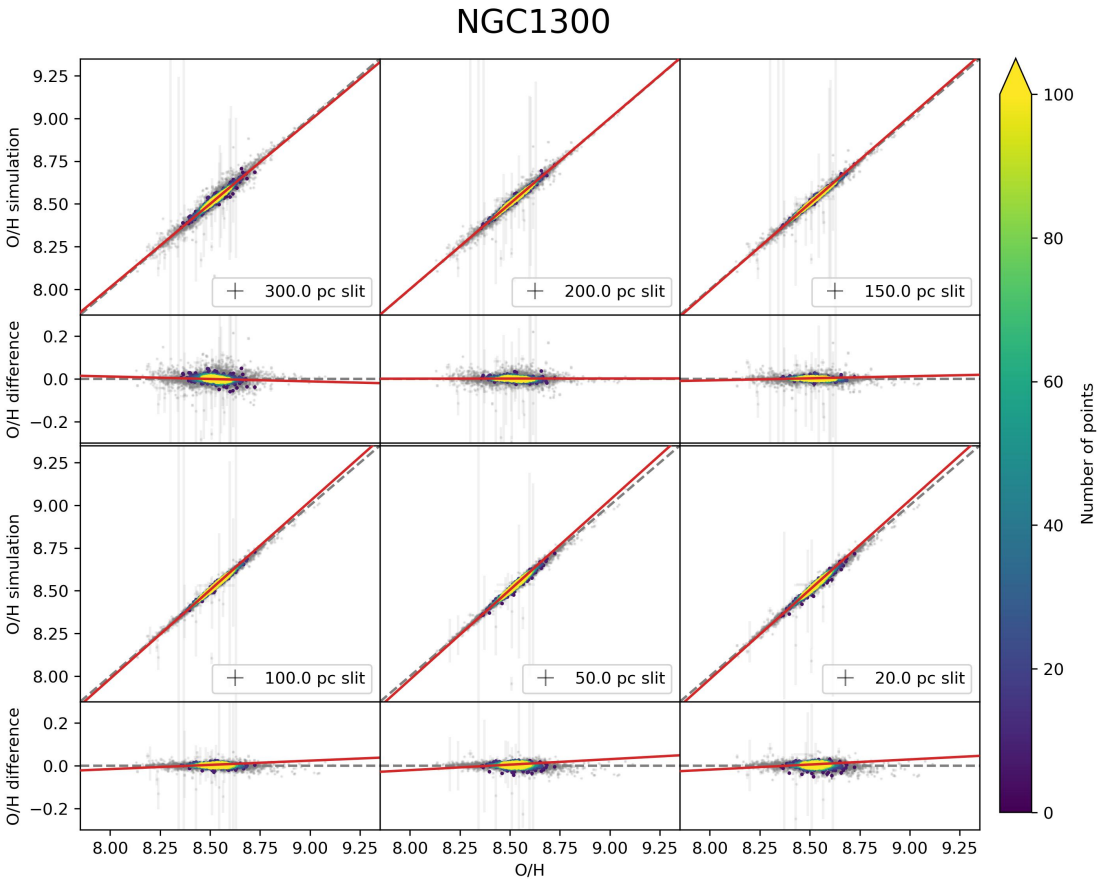

Figure B.6: As Figure 5.6 but for galaxy NGC1300. The sample includes 681 objects out of the 10,993 total. The full sample of data is plotted in gray for comparison. The red line is the linear fit of the sample (the coefficients are reported in Table B.6).

Table B.7: Coefficients of the linear fit ($y = Ax + B$) of the sample of data derived from the circular aperture restricted to the galaxy NGC1365, shown in Figure B.7, along with the weighted scattering of the data points with respect to the 1-to-1 diagonal, labelled σ.

Diameters pc	A	B dex	σ dex
300.0	1.015 ± 0.004	−0.13 ± 0.04	0.025
200.0	1.008 ± 0.007	−0.06 ± 0.06	0.025
150.0	0.996 ± 0.008	0.04 ± 0.07	0.027
100.0	0.981 ± 0.009	0.17 ± 0.07	0.019
50.0	0.968 ± 0.009	0.28 ± 0.08	0.022
20.0	0.963 ± 0.009	0.32 ± 0.08	0.023

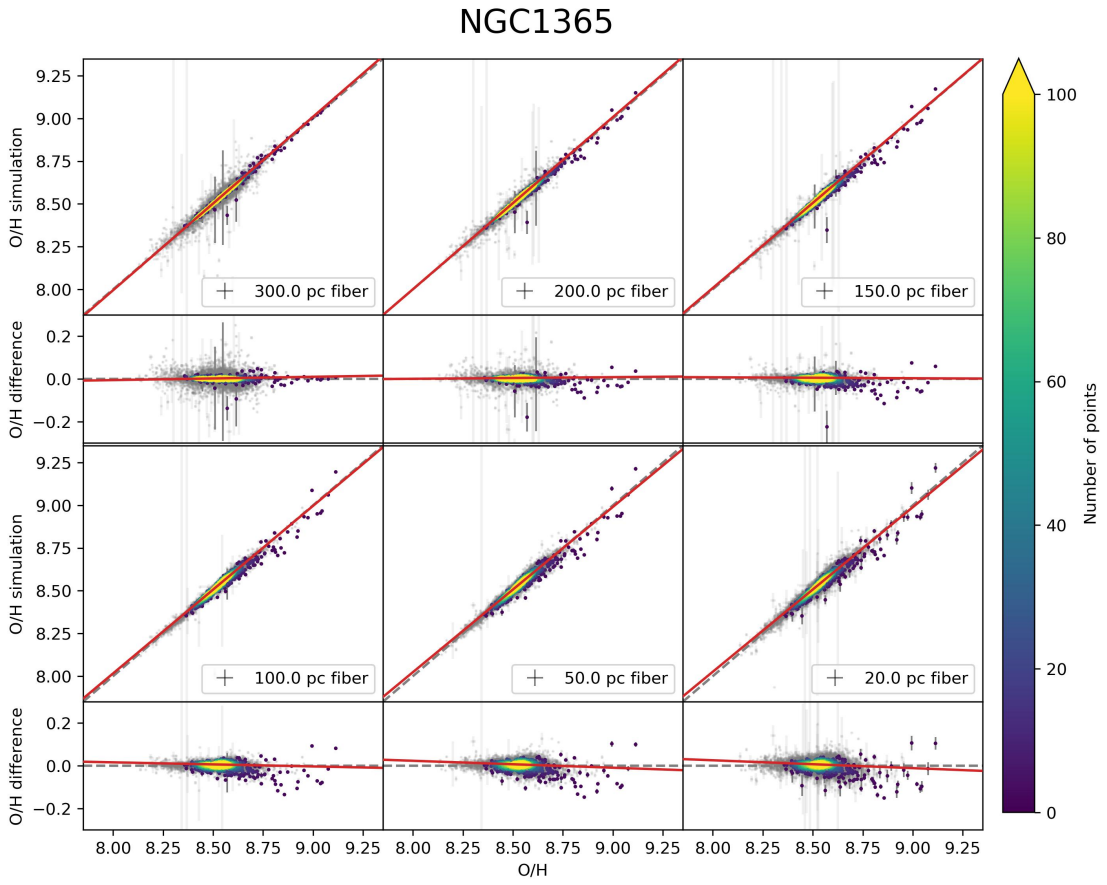

Figure B.7: As Figure 5.5 but for galaxy NGC1365. The sample includes 685 objects out of the 10,993 total. The full sample of data is plotted in gray for comparison. The red line is the linear fit of the sample (the coefficients are reported in Table B.7).

Table B.8: Coefficients of the linear fit ($y = Ax + B$) of the sample of data derived from the rectangular aperture restricted to the galaxy NGC1365, shown in Figure B.8, along with the weighted scattering of the data points with respect to the 1-to-1 diagonal, labelled σ.

Widths pc	A	B dex	σ dex
300.0	1.003 ± 0.003	−0.02 ± 0.02	0.024
200.0	1.011 ± 0.003	−0.09 ± 0.03	0.034
150.0	1.012 ± 0.004	−0.10 ± 0.03	0.032
100.0	1.010 ± 0.005	−0.08 ± 0.04	0.017
50.0	1.004 ± 0.005	−0.03 ± 0.04	0.027
20.0	1.000 ± 0.005	0.01 ± 0.04	0.012

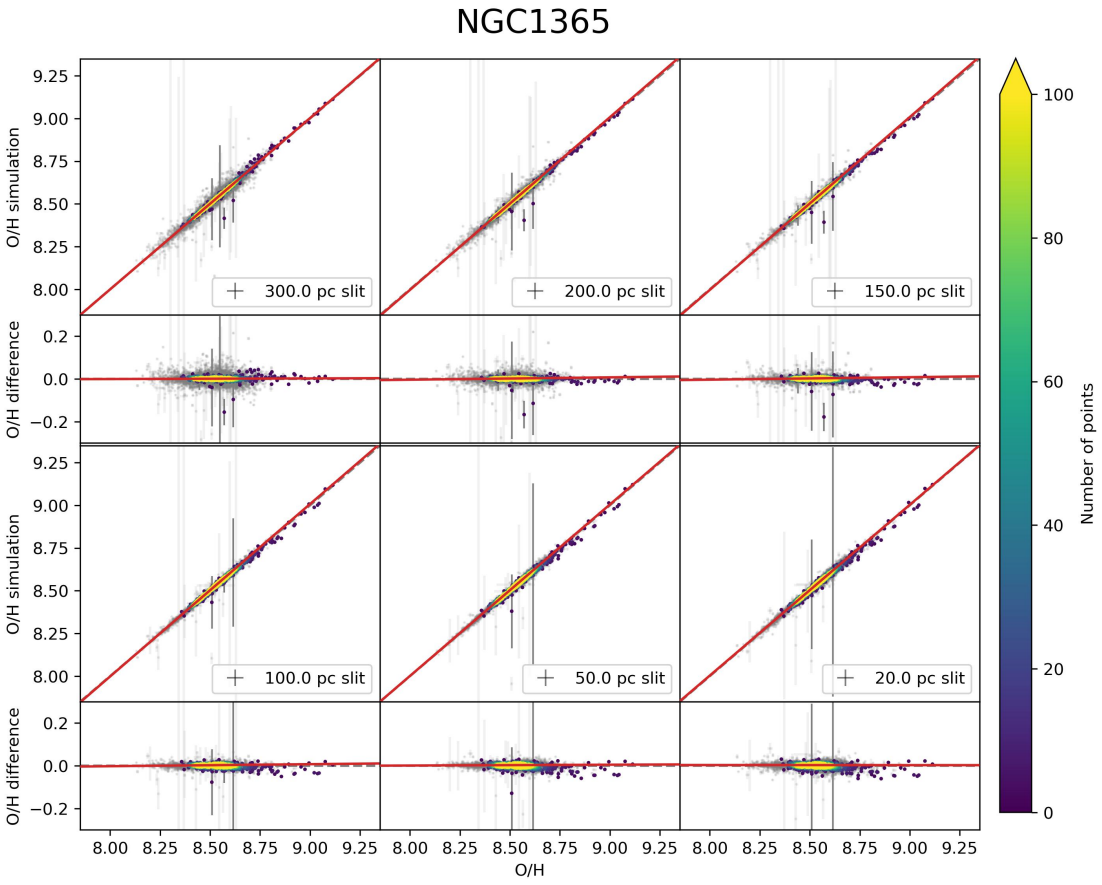

Figure B.8: As Figure 5.6 but for galaxy NGC1365. The sample includes 685 objects out of the 10,993 total. The full sample of data is plotted in gray for comparison. The red line is the linear fit of the sample (the coefficients are reported in Table B.8).

Table B.9: Coefficients of the linear fit ($y = Ax + B$) of the sample of data derived from the circular aperture restricted to the galaxy NGC1385, shown in Figure B.9, along with the weighted scattering of the data points with respect to the 1-to-1 diagonal, labelled σ.

Diameters pc	A	B dex	σ dex
300.0	0.989 ± 0.008	0.09 ± 0.07	0.011
200.0	1.039 ± 0.008	−0.32 ± 0.07	0.007
150.0	1.066 ± 0.009	−0.55 ± 0.08	0.006
100.0	1.08 ± 0.01	−0.68 ± 0.09	0.009
50.0	1.08 ± 0.01	−0.7 ± 0.1	0.015
20.0	1.08 ± 0.01	−0.6 ± 0.1	0.017

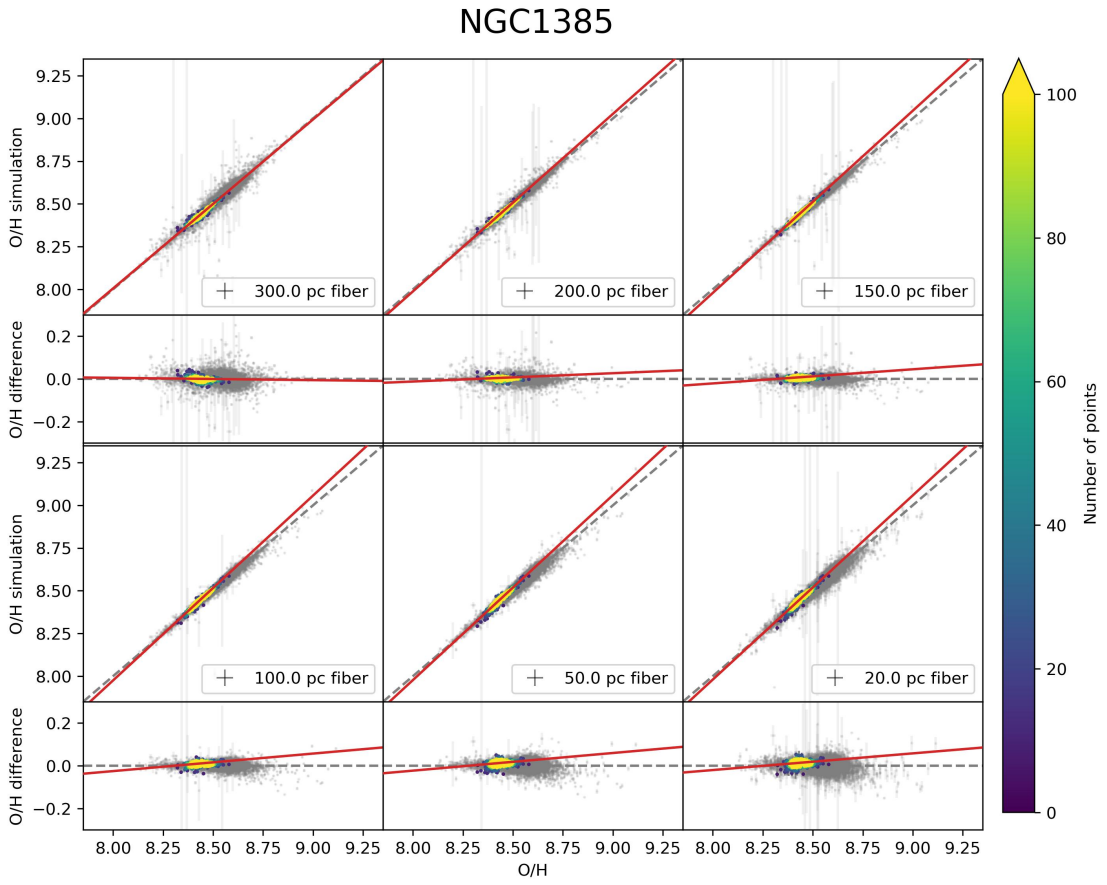

Figure B.9: As Figure 5.5 but for galaxy NGC1385. The sample includes 313 objects out of the 10,993 total. The full sample of data is plotted in gray for comparison. The red line is the linear fit of the sample (the coefficients are reported in Table B.9).

Table B.10: Coefficients of the linear fit ($y = Ax + B$) of the sample of data derived from the rectangular aperture restricted to the galaxy NGC1385, shown in Figure B.10, along with the weighted scattering of the data points with respect to the 1-to-1 diagonal, labelled σ.

Widths pc	A	B dex	σ dex
300.0	0.971 ± 0.007	0.25 ± 0.06	0.009
200.0	0.998 ± 0.005	0.02 ± 0.04	0.007
150.0	1.015 ± 0.005	−0.12 ± 0.04	0.005
100.0	1.030 ± 0.006	−0.25 ± 0.05	0.004
50.0	1.041 ± 0.007	−0.34 ± 0.06	0.007
20.0	1.042 ± 0.008	−0.34 ± 0.07	0.008

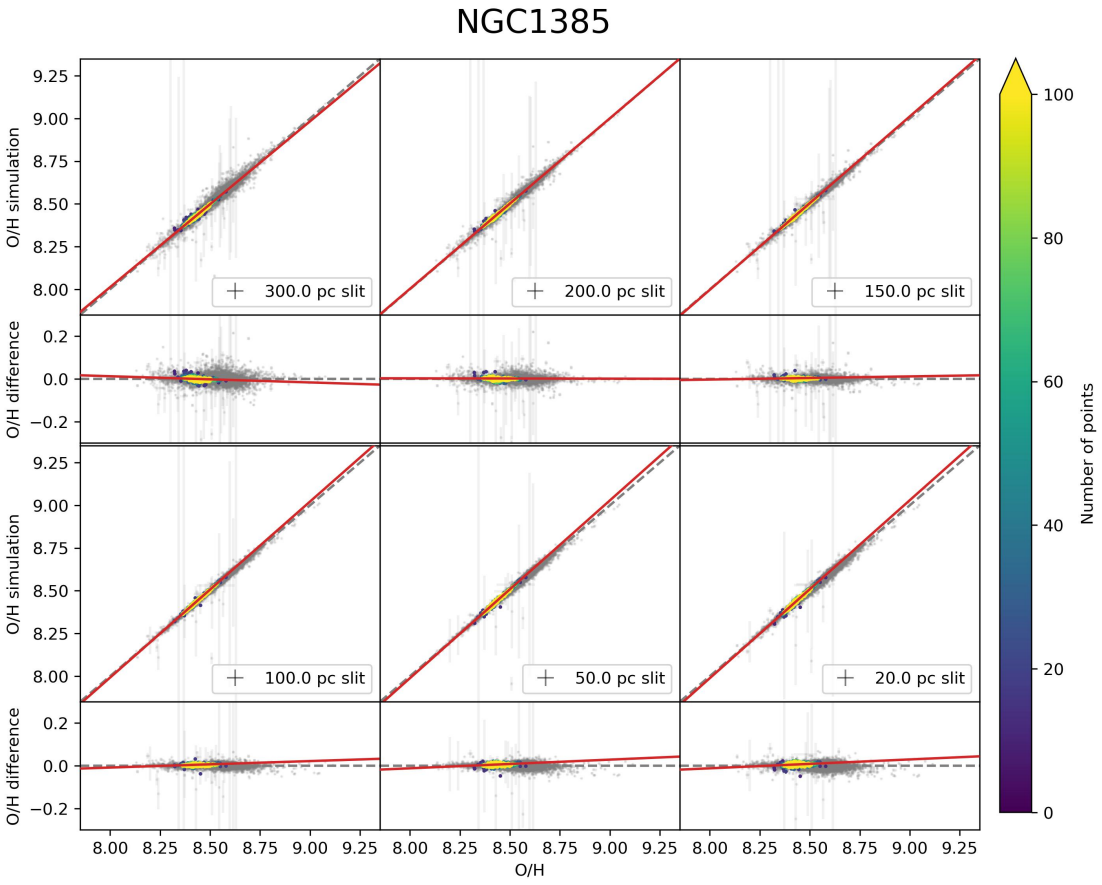

Figure B.10: As Figure 5.6 but for galaxy NGC1385. The sample includes 313 objects out of the 10,993 total. The full sample of data is plotted in gray for comparison. The red line is the linear fit of the sample (the coefficients are reported in Table B.10).

Table B.11: Coefficients of the linear fit ($y = Ax+B$) of the sample of data derived from the circular aperture restricted to the galaxy NGC1433, shown in Figure B.11, along with the weighted scattering of the data points with respect to the 1-to-1 diagonal, labelled σ.

Diameters pc	A	B dex	σ dex
300.0	0.994 ± 0.006	0.05 ± 0.05	0.041
200.0	0.954 ± 0.004	0.40 ± 0.04	0.050
150.0	0.927 ± 0.006	0.63 ± 0.05	0.030
100.0	0.893 ± 0.008	0.92 ± 0.07	0.013
50.0	0.86 ± 0.01	1.23 ± 0.08	0.020
20.0	0.84 ± 0.01	1.37 ± 0.09	0.042

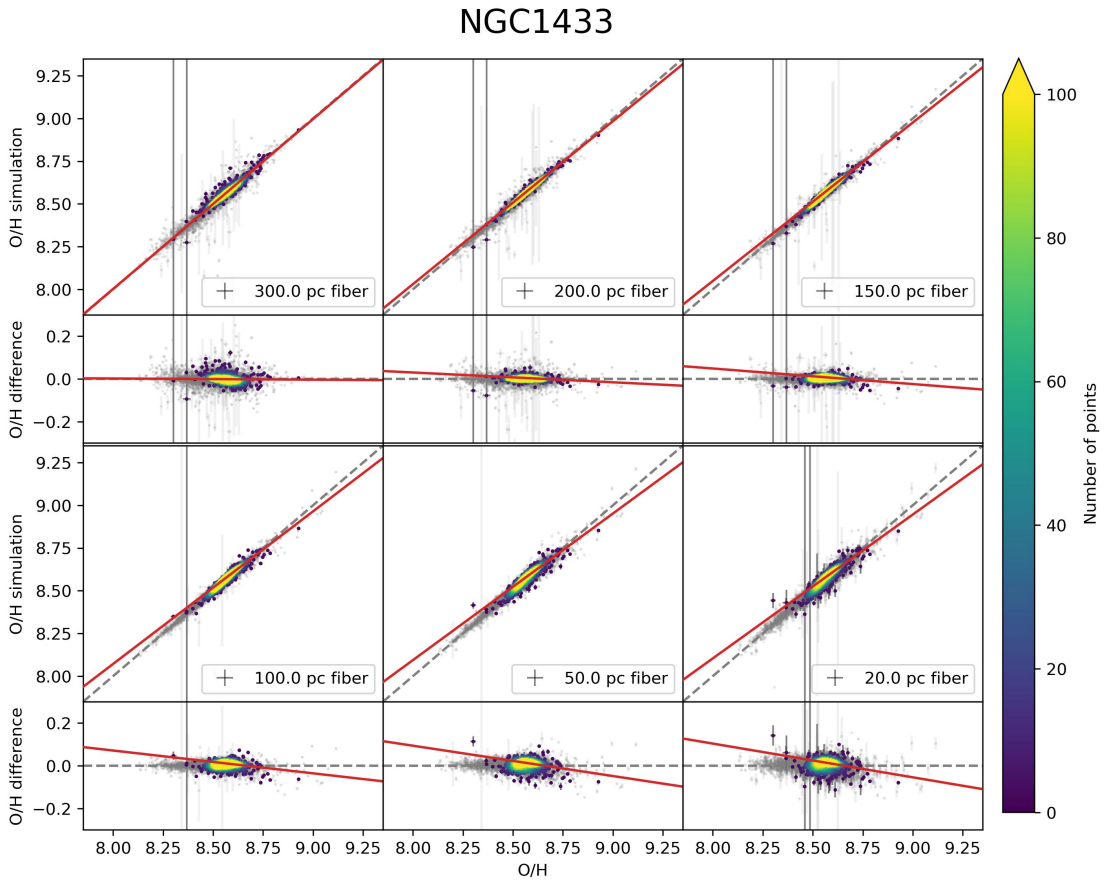

Figure B.11: As Figure 5.5 but for galaxy NGC1433. The sample includes 747 objects out of the 10,993 total. The full sample of data is plotted in gray for comparison. The red line is the linear fit of the sample (the coefficients are reported in Table B.11).

Table B.12: Coefficients of the linear fit ($y = Ax + B$) of the sample of data derived from the rectangular aperture restricted to the galaxy NGC1433, shown in Figure B.12, along with the weighted scattering of the data points with respect to the 1-to-1 diagonal, labelled σ.

Widths pc	A	B dex	σ dex
300.0	1.009 ± 0.006	-0.08 ± 0.05	0.048
200.0	0.994 ± 0.003	0.05 ± 0.03	0.039
150.0	0.985 ± 0.003	0.13 ± 0.03	0.018
100.0	0.975 ± 0.004	0.22 ± 0.03	0.010
50.0	0.963 ± 0.005	0.32 ± 0.04	0.011
20.0	0.956 ± 0.005	0.38 ± 0.05	0.012

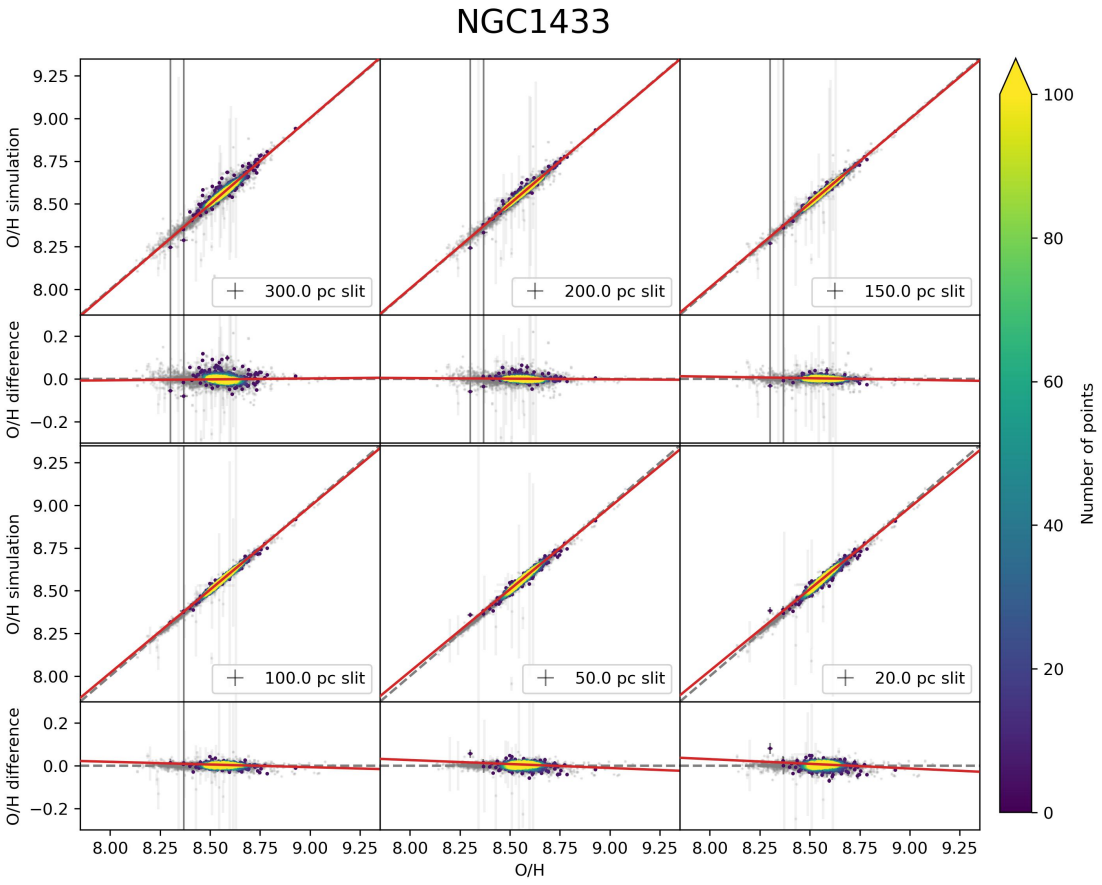

Figure B.12: As Figure 5.6 but for galaxy NGC1433. The sample includes 747 objects out of the 10,993 total. The full sample of data is plotted in gray for comparison. The red line is the linear fit of the sample (the coefficients are reported in Table B.12).

Table B.13: Coefficients of the linear fit ($y = Ax+B$) of the sample of data derived from the circular aperture restricted to the galaxy NGC1512, shown in Figure B.13, along with the weighted scattering of the data points with respect to the 1-to-1 diagonal, labelled σ.

Diameters pc	A	B dex	σ dex
300.0	0.97 ± 0.01	0.20 ± 0.08	0.012
200.0	1.01 ± 0.02	−0.1 ± 0.1	0.008
150.0	1.00 ± 0.02	−0.0 ± 0.2	0.012
100.0	0.97 ± 0.02	0.2 ± 0.2	0.018
50.0	0.94 ± 0.03	0.5 ± 0.2	0.022
20.0	0.93 ± 0.03	0.6 ± 0.2	0.023

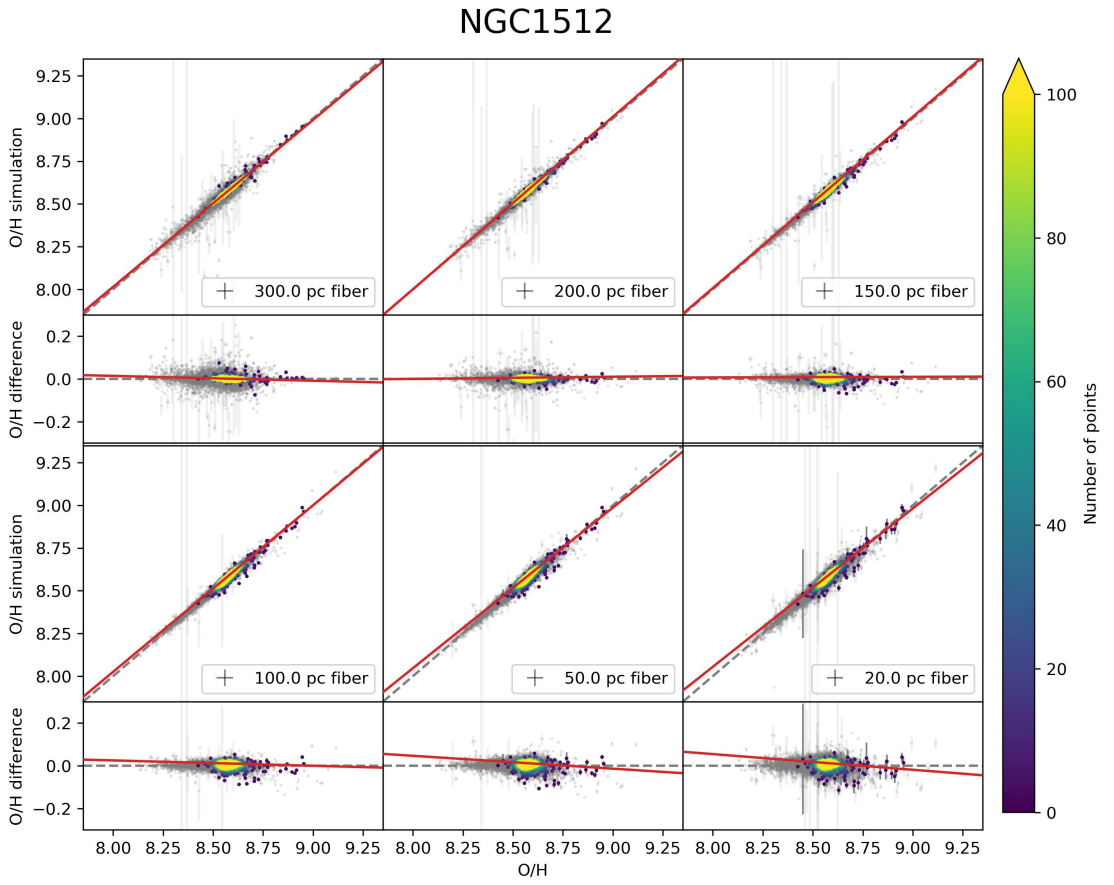

Figure B.13: As Figure 5.5 but for galaxy NGC1512. The sample includes 385 objects out of the 10,993 total. The full sample of data is plotted in gray for comparison. The red line is the linear fit of the sample (the coefficients are reported in Table B.13).

Table B.14: Coefficients of the linear fit ($y = Ax + B$) of the sample of data derived from the rectangular aperture restricted to the galaxy NGC1512, shown in Figure B.14, along with the weighted scattering of the data points with respect to the 1-to-1 diagonal, labelled σ.

Widths pc	A	B dex	σ dex
300.0	0.952 ± 0.007	0.41 ± 0.06	0.012
200.0	0.956 ± 0.008	0.38 ± 0.07	0.006
150.0	0.95 ± 0.01	0.43 ± 0.09	0.005
100.0	0.94 ± 0.01	0.5 ± 0.1	0.008
50.0	0.92 ± 0.01	0.7 ± 0.1	0.010
20.0	0.91 ± 0.02	0.8 ± 0.1	0.011

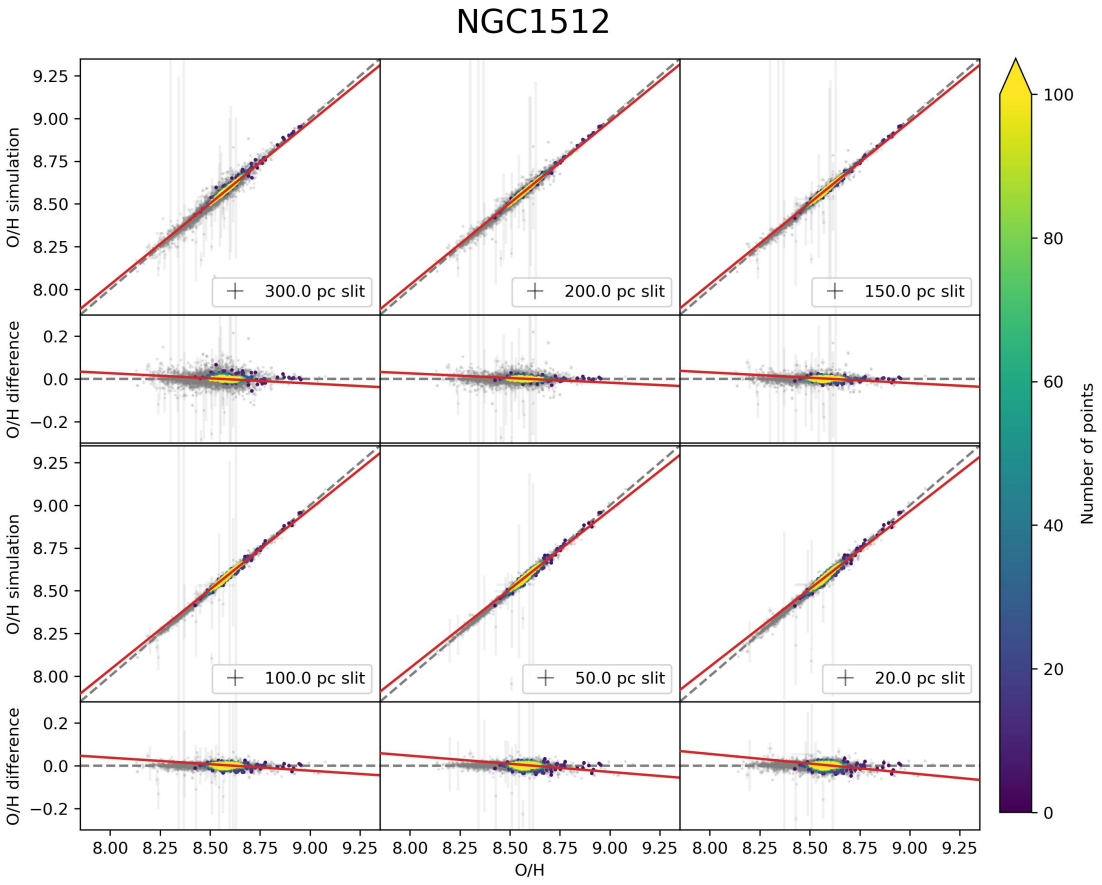

Figure B.14: As Figure 5.6 but for galaxy NGC1512. The sample includes 385 objects out of the 10,993 total. The full sample of data is plotted in gray for comparison. The red line is the linear fit of the sample (the coefficients are reported in Table B.14).

Table B.15: Coefficients of the linear fit ($y = Ax + B$) of the sample of data derived from the circular aperture restricted to the galaxy NGC1566, shown in Figure B.15, along with the weighted scattering of the data points with respect to the 1-to-1 diagonal, labelled σ.

Diameters pc	A	B dex	σ dex
300.0	0.99 ± 0.01	0.05 ± 0.09	0.042
200.0	1.041 ± 0.007	−0.35 ± 0.06	0.020
150.0	1.081 ± 0.008	−0.69 ± 0.07	0.010
100.0	1.12 ± 0.01	−1.00 ± 0.09	0.009
50.0	1.13 ± 0.01	−1.1 ± 0.1	0.016
20.0	1.12 ± 0.01	−1.0 ± 0.1	0.020

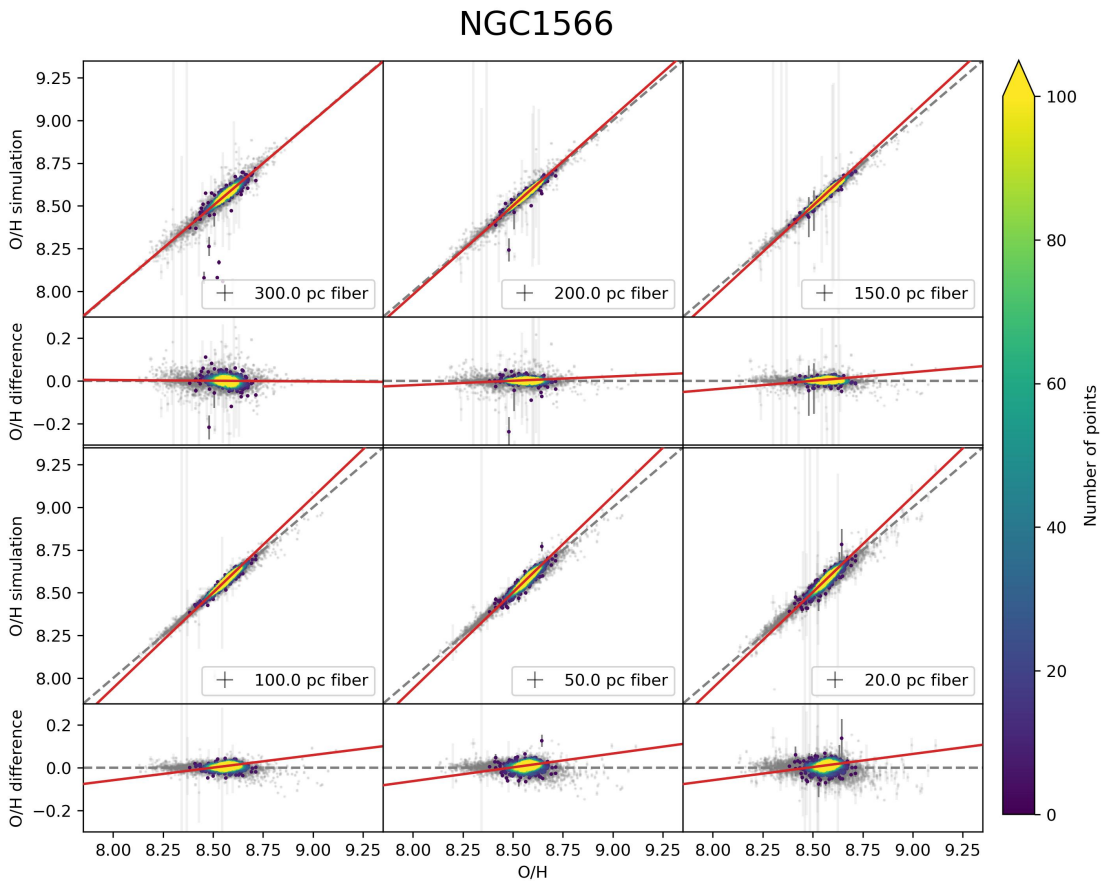

Figure B.15: As Figure 5.5 but for galaxy NGC1566. The sample includes 847 objects out of the 10,993 total. The full sample of data is plotted in gray for comparison. The red line is the linear fit of the sample (the coefficients are reported in Table B.15).

Table B.16: Coefficients of the linear fit ($y = Ax + B$) of the sample of data derived from the rectangular aperture restricted to the galaxy NGC1566, shown in Figure B.16, along with the weighted scattering of the data points with respect to the 1-to-1 diagonal, labelled σ.

Widths pc	A	B dex	σ dex
300.0	0.979 ± 0.009	0.18 ± 0.08	0.028
200.0	0.997 ± 0.006	0.03 ± 0.05	0.026
150.0	1.014 ± 0.005	-0.12 ± 0.04	0.014
100.0	1.036 ± 0.006	-0.30 ± 0.05	0.006
50.0	1.053 ± 0.007	-0.45 ± 0.06	0.008
20.0	1.054 ± 0.008	-0.45 ± 0.07	0.010

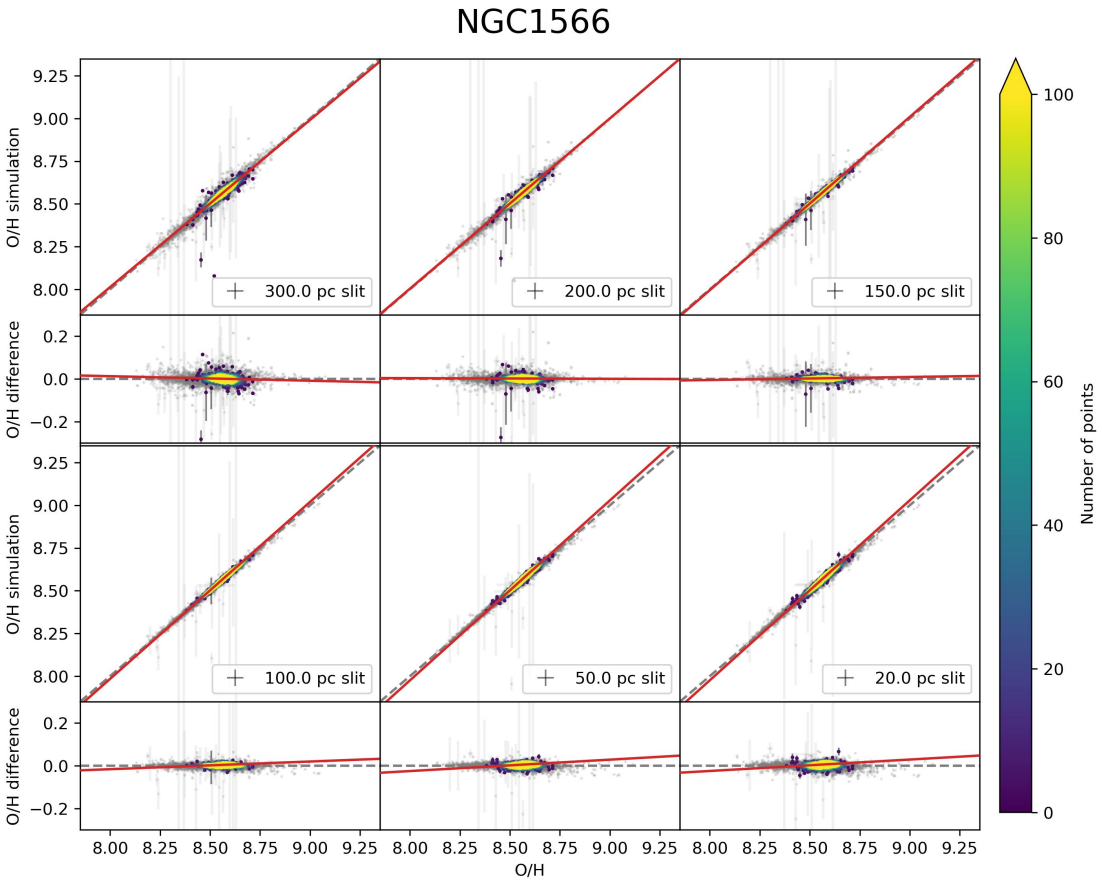

Figure B.16: As Figure 5.6 but for galaxy NGC1566. The sample includes 847 objects out of the 10,993 total. The full sample of data is plotted in gray for comparison. The red line is the linear fit of the sample (the coefficients are reported in Table B.16).

Table B.17: Coefficients of the linear fit ($y = Ax+B$) of the sample of data derived from the circular aperture restricted to the galaxy NGC1672, shown in Figure B.17, along with the weighted scattering of the data points with respect to the 1-to-1 diagonal, labelled σ.

Diameters pc	A	B dex	σ dex
300.0	1.041 ± 0.004	−0.35 ± 0.04	0.010
200.0	1.055 ± 0.006	−0.46 ± 0.05	0.005
150.0	1.062 ± 0.007	−0.52 ± 0.06	0.008
100.0	1.065 ± 0.009	−0.55 ± 0.07	0.011
50.0	1.06 ± 0.01	−0.50 ± 0.09	0.015
20.0	1.06 ± 0.01	−0.48 ± 0.09	0.016

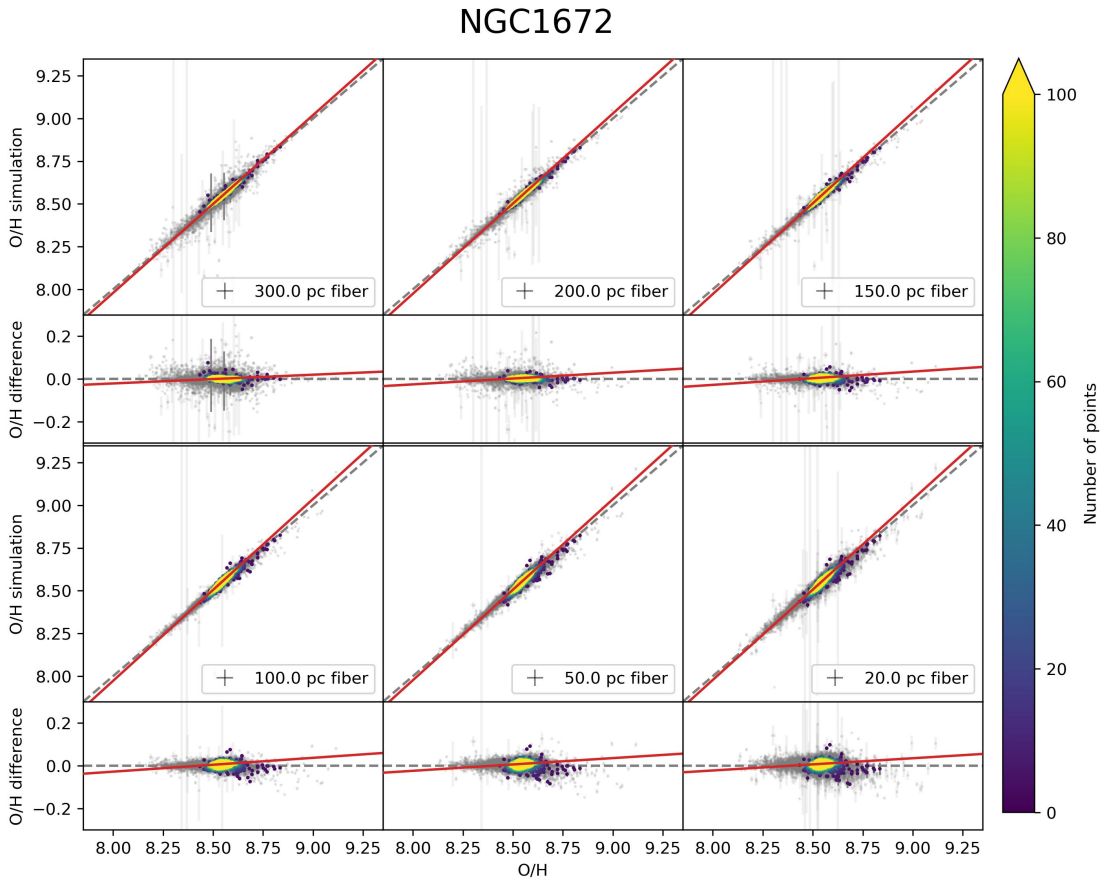

Figure B.17: As Figure 5.5 but for galaxy NGC1672. The sample includes 637 objects out of the 10,993 total. The full sample of data is plotted in gray for comparison. The red line is the linear fit of the sample (the coefficients are reported in Table B.17).

Table B.18: Coefficients of the linear fit ($y = Ax + B$) of the sample of data derived from the rectangular aperture restricted to the galaxy NGC1672, shown in Figure B.18, along with the weighted scattering of the data points with respect to the 1-to-1 diagonal, labelled σ.

Widths pc	A	B dex	σ dex
300.0	1.021 ± 0.003	-0.18 ± 0.03	0.008
200.0	1.017 ± 0.003	-0.14 ± 0.02	0.004
150.0	1.015 ± 0.003	-0.12 ± 0.03	0.004
100.0	1.011 ± 0.004	-0.09 ± 0.04	0.006
50.0	1.007 ± 0.005	-0.06 ± 0.04	0.008
20.0	1.004 ± 0.005	-0.03 ± 0.04	0.008

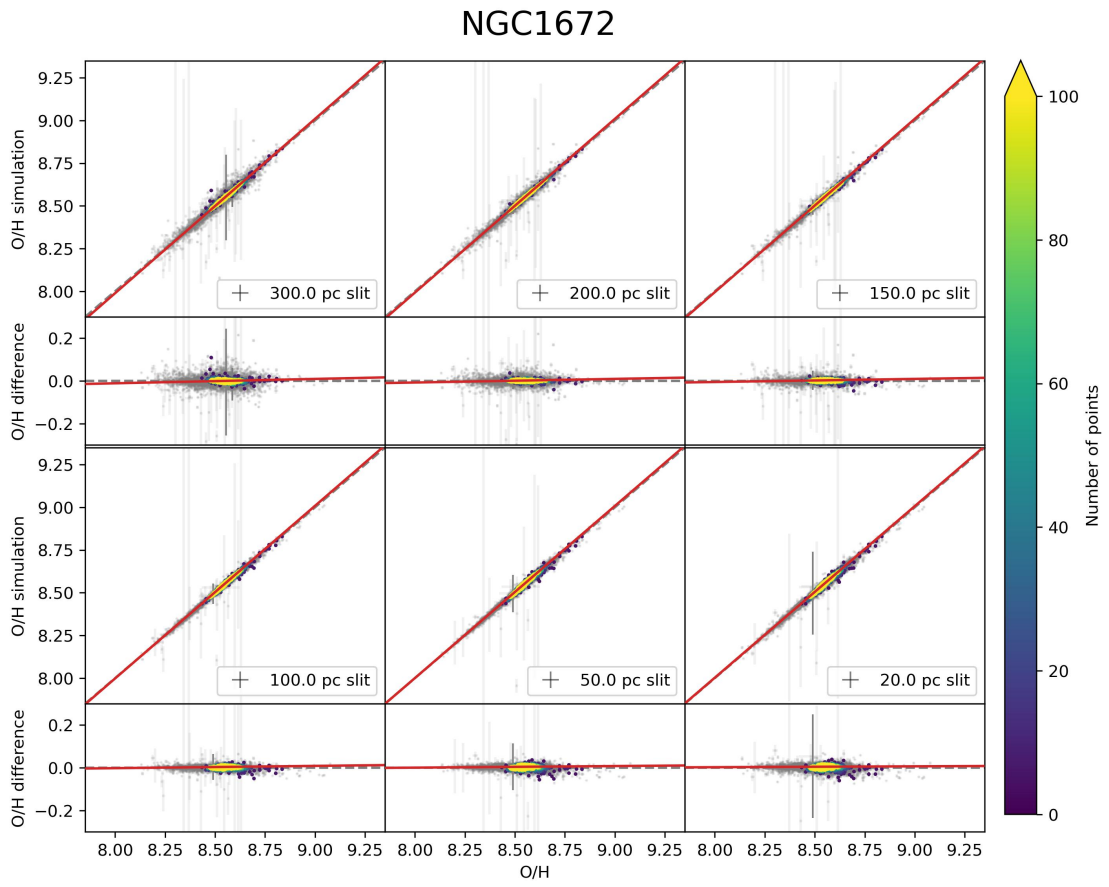

Figure B.18: As Figure 5.6 but for galaxy NGC1672. The sample includes 637 objects out of the 10,993 total. The full sample of data is plotted in gray for comparison. The red line is the linear fit of the sample (the coefficients are reported in Table B.18).

Table B.19: Coefficients of the linear fit ($y = Ax+B$) of the sample of data derived from the circular aperture restricted to the galaxy NGC2835, shown in Figure B.19, along with the weighted scattering of the data points with respect to the 1-to-1 diagonal, labelled σ.

Diameters pc	A	B dex	σ dex
300.0	0.989 ± 0.006	0.09 ± 0.05	0.013
200.0	1.011 ± 0.005	−0.09 ± 0.04	0.007
150.0	1.022 ± 0.006	−0.18 ± 0.05	0.006
100.0	1.029 ± 0.008	−0.23 ± 0.06	0.009
50.0	1.03 ± 0.01	−0.23 ± 0.08	0.014
20.0	1.03 ± 0.01	−0.21 ± 0.09	0.017

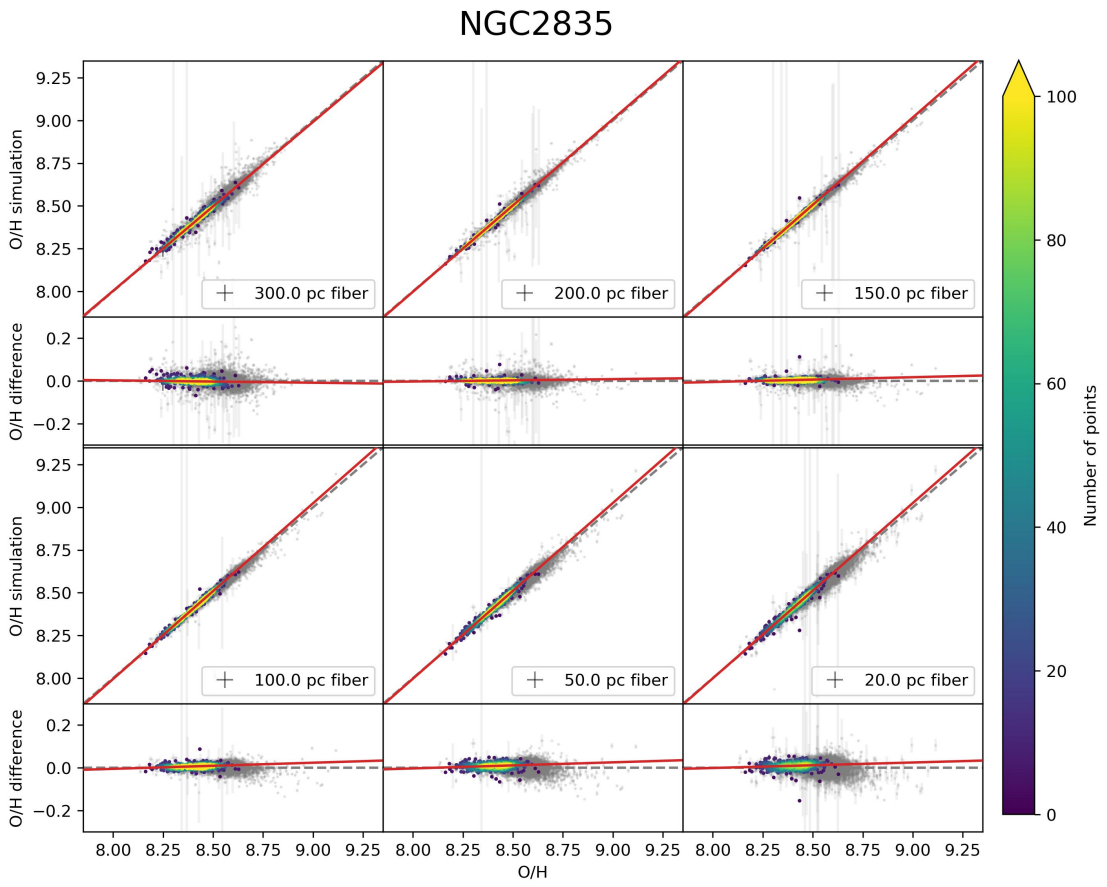

Figure B.19: As Figure 5.5 but for galaxy NGC2835. The sample includes 359 objects out of the 10,993 total. The full sample of data is plotted in gray for comparison. The red line is the linear fit of the sample (the coefficients are reported in Table B.19).

Table B.20: Coefficients of the linear fit ($y = Ax + B$) of the sample of data derived from the rectangular aperture restricted to the galaxy NGC2835, shown in Figure B.20, along with the weighted scattering of the data points with respect to the 1-to-1 diagonal, labelled σ.

Widths pc	A	B dex	σ dex
300.0	0.992 ± 0.005	0.07 ± 0.05	0.012
200.0	1.003 ± 0.003	-0.02 ± 0.03	0.007
150.0	1.010 ± 0.004	-0.08 ± 0.03	0.004
100.0	1.015 ± 0.004	-0.12 ± 0.04	0.004
50.0	1.016 ± 0.005	-0.14 ± 0.04	0.007
20.0	1.015 ± 0.006	-0.12 ± 0.05	0.008

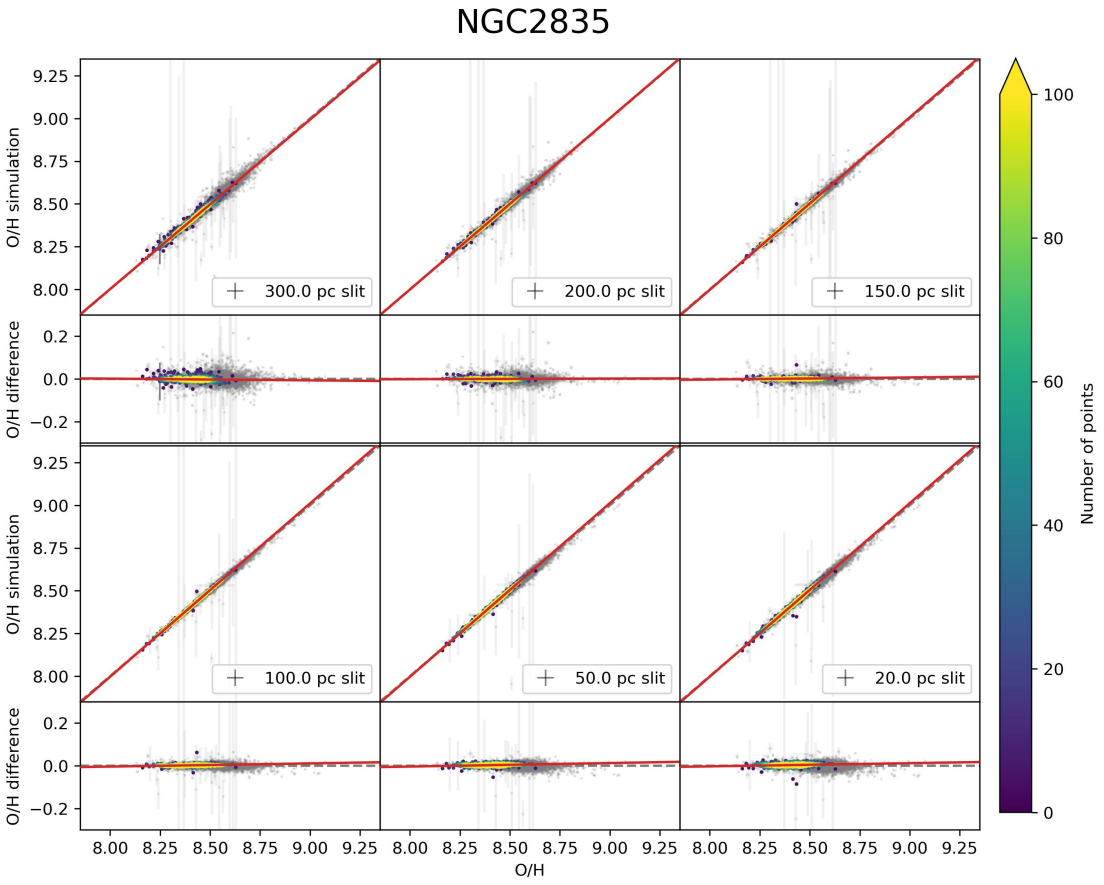

Figure B.20: As Figure 5.6 but for galaxy NGC2835. The sample includes 359 objects out of the 10,993 total. The full sample of data is plotted in gray for comparison. The red line is the linear fit of the sample (the coefficients are reported in Table B.20).

Table B.21: Coefficients of the linear fit ($y = Ax+B$) of the sample of data derived from the circular aperture restricted to the galaxy NGC3351, shown in Figure B.21, along with the weighted scattering of the data points with respect to the 1-to-1 diagonal, labelled σ.

Diameters pc	A	B dex	σ dex
300.0	0.93 ± 0.03	0.6 ± 0.3	0.068
200.0	0.95 ± 0.02	0.4 ± 0.1	0.021
150.0	1.05 ± 0.02	-0.5 ± 0.2	0.020
100.0	1.18 ± 0.03	-1.5 ± 0.3	0.017
50.0	1.17 ± 0.04	-1.5 ± 0.3	0.018
20.0	1.07 ± 0.04	-0.6 ± 0.4	0.060

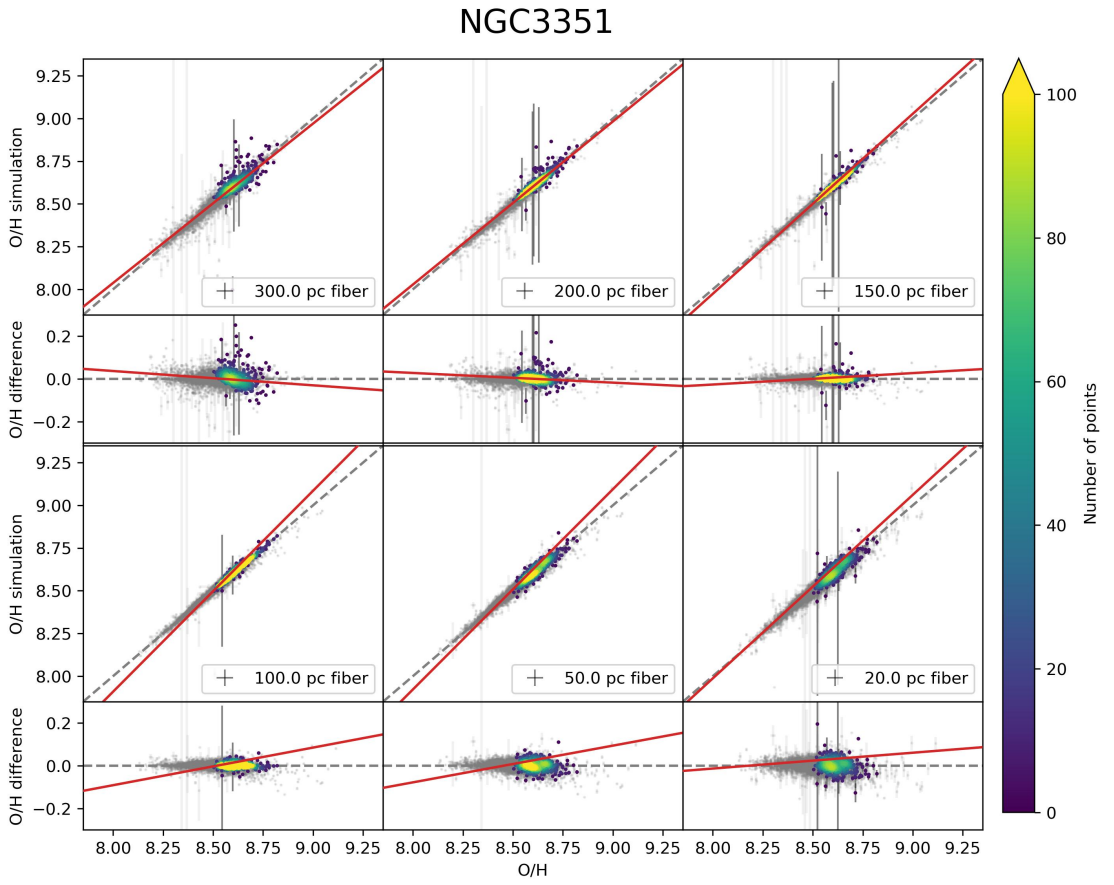

Figure B.21: As Figure 5.5 but for galaxy NGC3351. The sample includes 405 objects out of the 10,993 total. The full sample of data is plotted in gray for comparison. The red line is the linear fit of the sample (the coefficients are reported in Table B.21).

Table B.22: Coefficients of the linear fit ($y = Ax + B$) of the sample of data derived from the rectangular aperture restricted to the galaxy NGC3351, shown in Figure B.22, along with the weighted scattering of the data points with respect to the 1-to-1 diagonal, labelled σ.

Widths pc	A	B dex	σ dex
300.0	0.91 ± 0.02	0.8 ± 0.2	0.031
200.0	0.94 ± 0.02	0.5 ± 0.1	0.020
150.0	0.97 ± 0.02	0.3 ± 0.1	0.021
100.0	1.03 ± 0.02	−0.3 ± 0.1	0.025
50.0	1.10 ± 0.02	−0.8 ± 0.2	0.022
20.0	1.09 ± 0.02	−0.8 ± 0.2	0.021

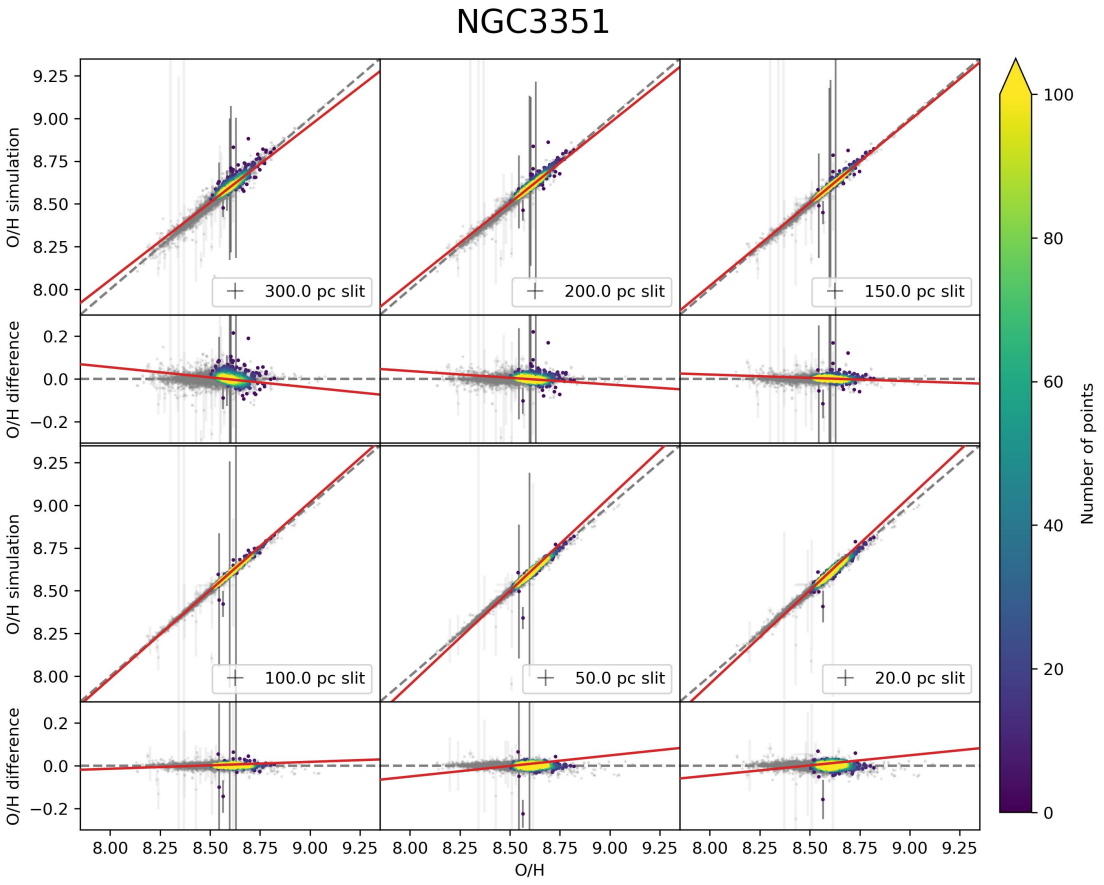

Figure B.22: As Figure 5.6 but for galaxy NGC3351. The sample includes 405 objects out of the 10,993 total. The full sample of data is plotted in gray for comparison. The red line is the linear fit of the sample (the coefficients are reported in Table B.22).

Table B.23: Coefficients of the linear fit ($y = Ax + B$) of the sample of data derived from the circular aperture restricted to the galaxy NGC3627, shown in Figure B.23, along with the weighted scattering of the data points with respect to the 1-to-1 diagonal, labelled σ.

Diameters pc	A	B dex	σ dex
300.0	0.89 ± 0.02	0.9 ± 0.1	0.019
200.0	1.02 ± 0.01	−0.15 ± 0.09	0.010
150.0	1.11 ± 0.01	−1.0 ± 0.1	0.006
100.0	1.21 ± 0.02	−1.8 ± 0.1	0.010
50.0	1.25 ± 0.02	−2.2 ± 0.2	0.018
20.0	1.24 ± 0.02	−2.1 ± 0.2	0.020

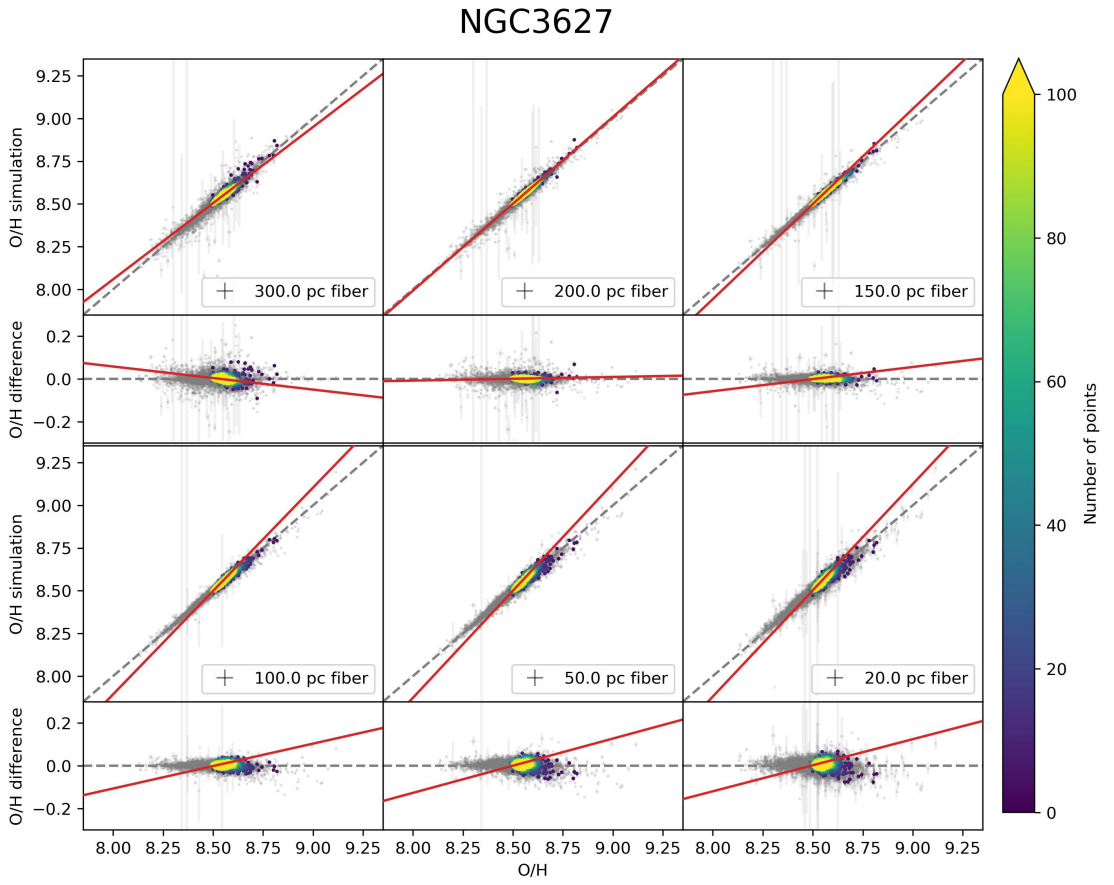

Figure B.23: As Figure 5.5 but for galaxy NGC3627. The sample includes 435 objects out of the 10,993 total. The full sample of data is plotted in gray for comparison. The red line is the linear fit of the sample (the coefficients are reported in Table B.23).

Table B.24: Coefficients of the linear fit ($y = Ax + B$) of the sample of data derived from the rectangular aperture restricted to the galaxy NGC3627, shown in Figure B.24, along with the weighted scattering of the data points with respect to the 1-to-1 diagonal, labelled σ.

Widths pc	A	B dex	σ dex
300.0	0.89 ± 0.01	0.9 ± 0.1	0.016
200.0	0.962 ± 0.009	0.33 ± 0.07	0.009
150.0	1.009 ± 0.008	-0.08 ± 0.07	0.006
100.0	1.071 ± 0.009	-0.60 ± 0.08	0.005
50.0	1.13 ± 0.01	-1.0 ± 0.1	0.008
20.0	1.13 ± 0.01	-1.1 ± 0.1	0.010

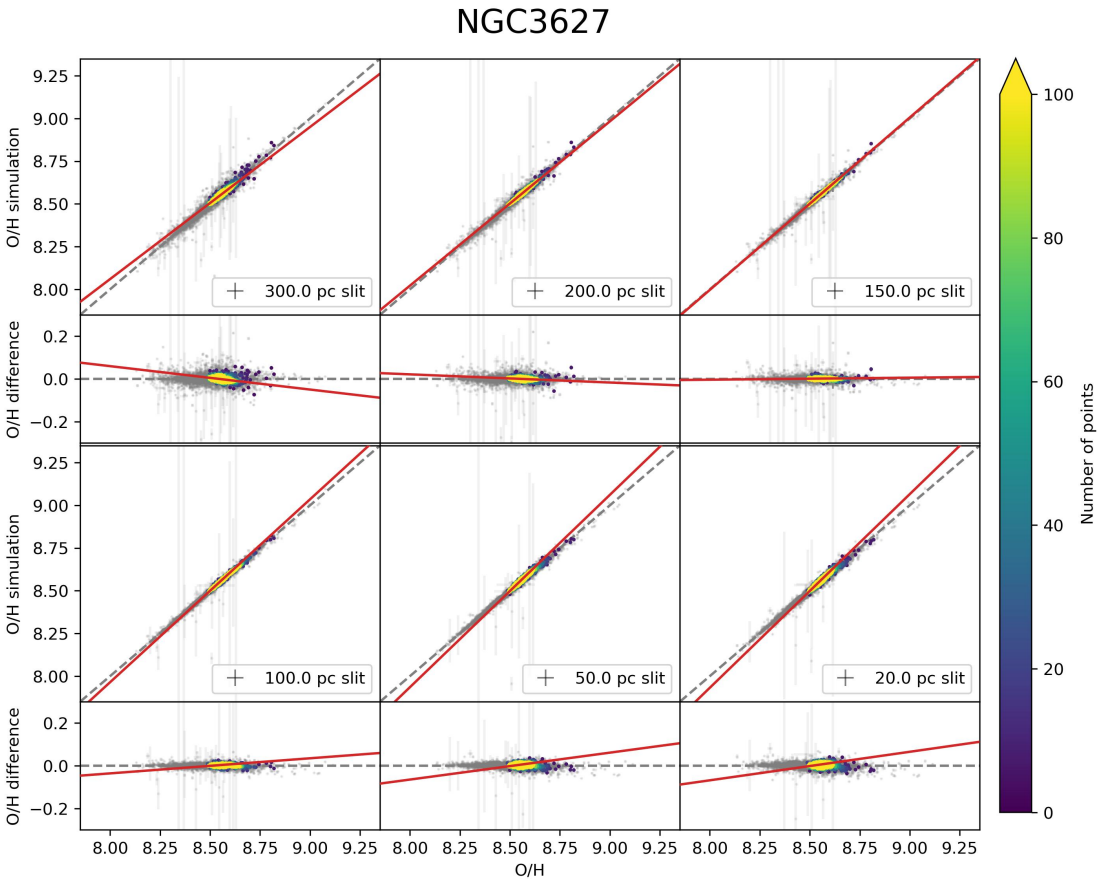

Figure B.24: As Figure 5.6 but for galaxy NGC3627. The sample includes 435 objects out of the 10,993 total. The full sample of data is plotted in gray for comparison. The red line is the linear fit of the sample (the coefficients are reported in Table B.24).

Table B.25: Coefficients of the linear fit ($y = Ax+B$) of the sample of data derived from the circular aperture restricted to the galaxy NGC4254, shown in Figure B.25, along with the weighted scattering of the data points with respect to the 1-to-1 diagonal, labelled σ.

Diameters pc	A	B dex	σ dex
300.0	0.951 ± 0.008	0.42 ± 0.07	0.013
200.0	1.006 ± 0.005	−0.05 ± 0.04	0.007
150.0	1.062 ± 0.005	−0.53 ± 0.04	0.005
100.0	1.136 ± 0.007	−1.15 ± 0.06	0.007
50.0	1.19 ± 0.01	−1.59 ± 0.09	0.013
20.0	1.19 ± 0.01	−1.60 ± 0.09	0.015

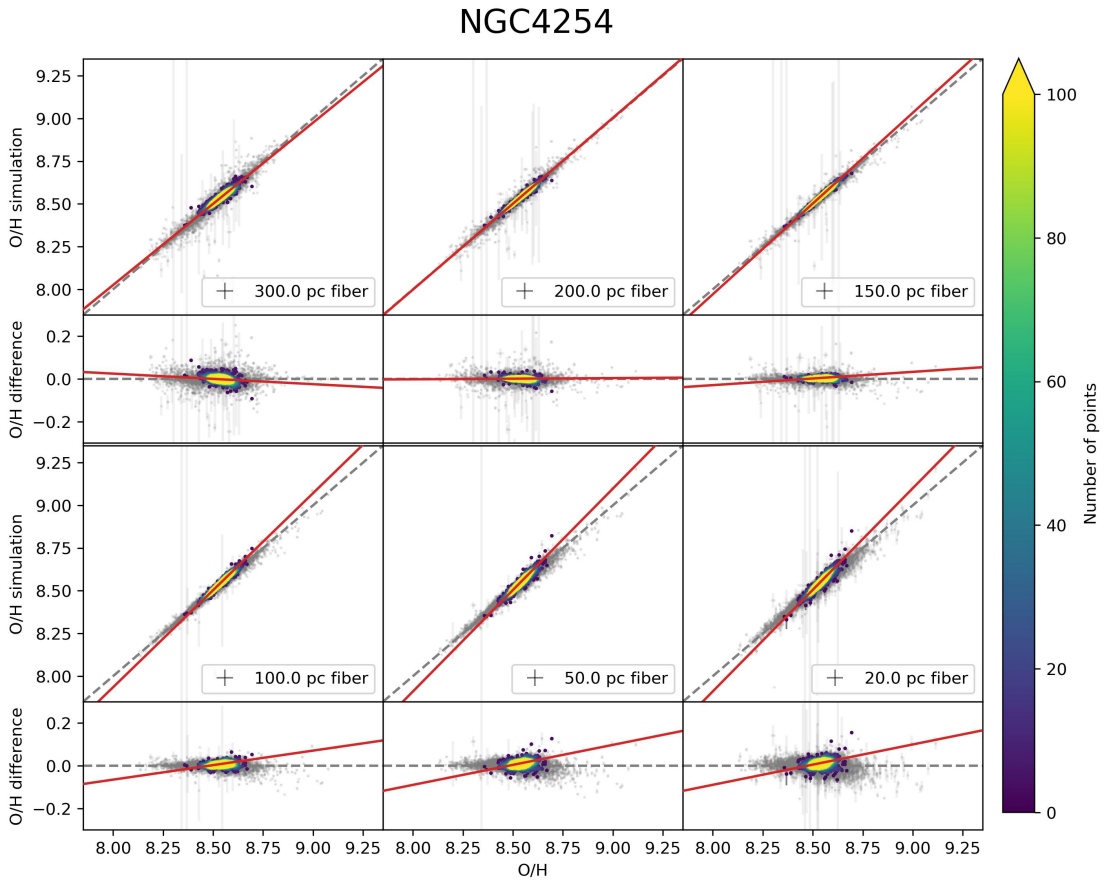

Figure B.25: As Figure 5.5 but for galaxy NGC4254. The sample includes 1159 objects out of the 10,993 total. The full sample of data is plotted in gray for comparison. The red line is the linear fit of the sample (the coefficients are reported in Table B.25).

Table B.26: Coefficients of the linear fit ($y = Ax + B$) of the sample of data derived from the rectangular aperture restricted to the galaxy NGC4254, shown in Figure B.26, along with the weighted scattering of the data points with respect to the 1-to-1 diagonal, labelled σ.

Widths pc	A	B dex	σ dex
300.0	0.951 ± 0.006	0.42 ± 0.05	0.010
200.0	0.984 ± 0.004	0.13 ± 0.04	0.006
150.0	1.014 ± 0.003	−0.11 ± 0.03	0.004
100.0	1.055 ± 0.004	−0.46 ± 0.03	0.003
50.0	1.096 ± 0.005	−0.82 ± 0.04	0.006
20.0	1.107 ± 0.006	−0.91 ± 0.05	0.008

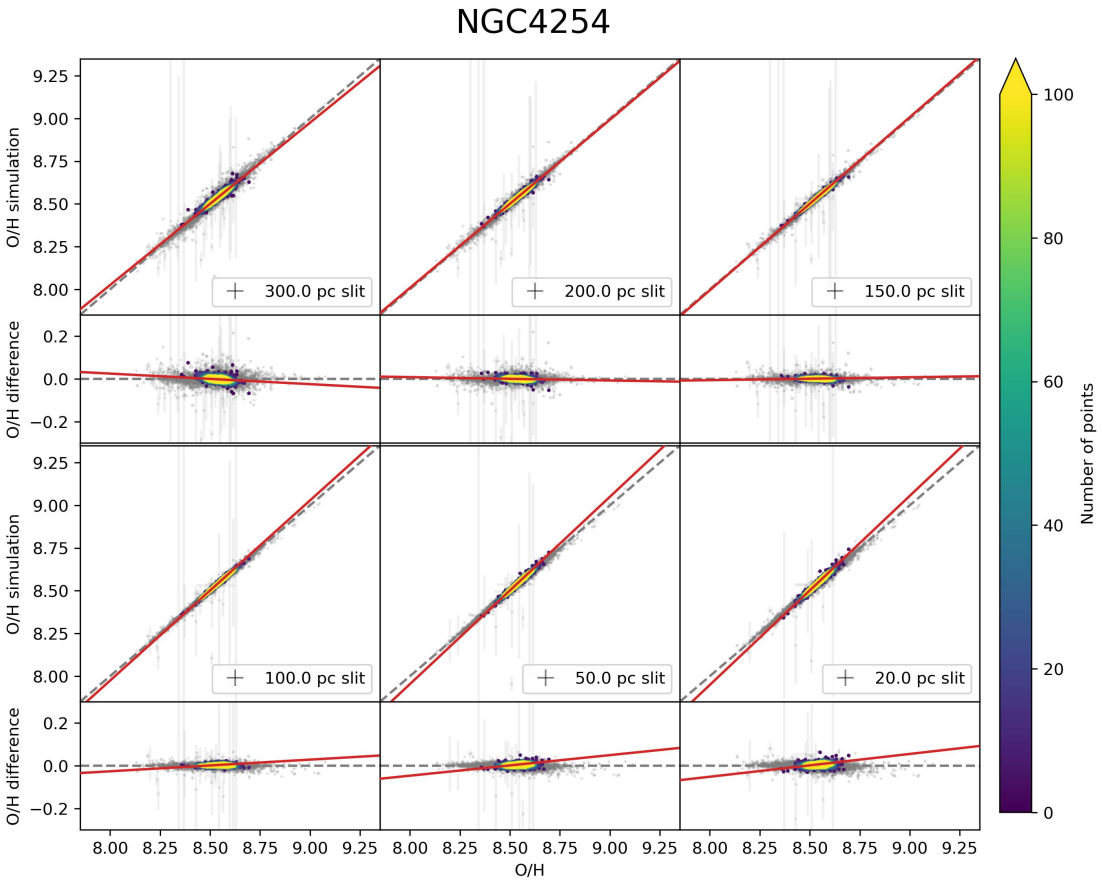

Figure B.26: As Figure 5.6 but for galaxy NGC4254. The sample includes 1159 objects out of the 10,993 total. The full sample of data is plotted in gray for comparison. The red line is the linear fit of the sample (the coefficients are reported in Table B.26).

Table B.27: Coefficients of the linear fit ($y = Ax + B$) of the sample of data derived from the circular aperture restricted to the galaxy NGC4303, shown in Figure B.27, along with the weighted scattering of the data points with respect to the 1-to-1 diagonal, labelled σ.

Diameters pc	A	B dex	σ dex
300.0	0.978 ± 0.008	0.19 ± 0.07	0.014
200.0	1.020 ± 0.006	−0.17 ± 0.05	0.010
150.0	1.062 ± 0.007	−0.53 ± 0.06	0.009
100.0	1.10 ± 0.01	−0.84 ± 0.09	0.009
50.0	1.11 ± 0.01	−0.9 ± 0.1	0.013
20.0	1.10 ± 0.01	−0.8 ± 0.1	0.016

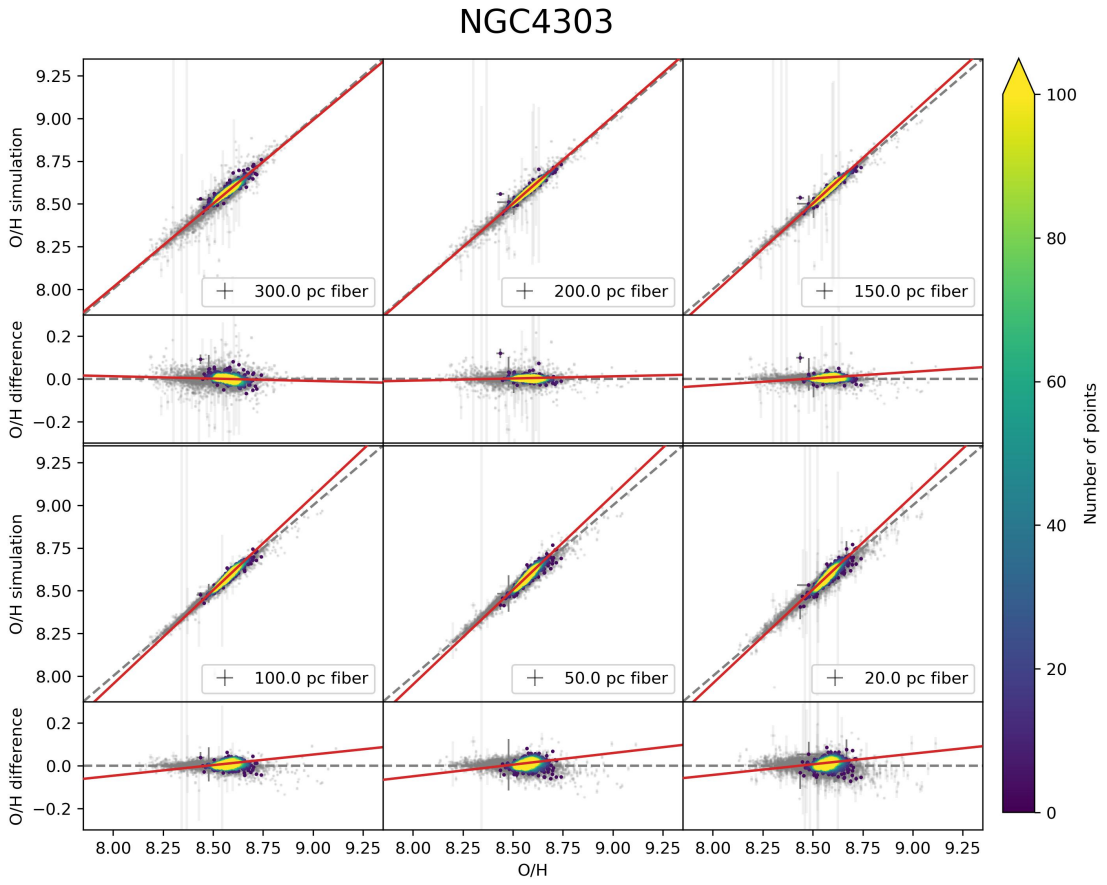

Figure B.27: As Figure 5.5 but for galaxy NGC4303. The sample includes 1011 objects out of the 10,993 total. The full sample of data is plotted in gray for comparison. The red line is the linear fit of the sample (the coefficients are reported in Table B.27).

Table B.28: Coefficients of the linear fit ($y = Ax + B$) of the sample of data derived from the rectangular aperture restricted to the galaxy NGC4303, shown in Figure B.28, along with the weighted scattering of the data points with respect to the 1-to-1 diagonal, labelled σ.

Widths pc	A	B dex	σ dex
300.0	0.989 ± 0.008	0.10 ± 0.07	0.011
200.0	1.003 ± 0.004	-0.02 ± 0.04	0.007
150.0	1.019 ± 0.004	-0.16 ± 0.04	0.005
100.0	1.039 ± 0.005	-0.33 ± 0.04	0.005
50.0	1.054 ± 0.007	-0.46 ± 0.06	0.007
20.0	1.052 ± 0.007	-0.44 ± 0.06	0.009

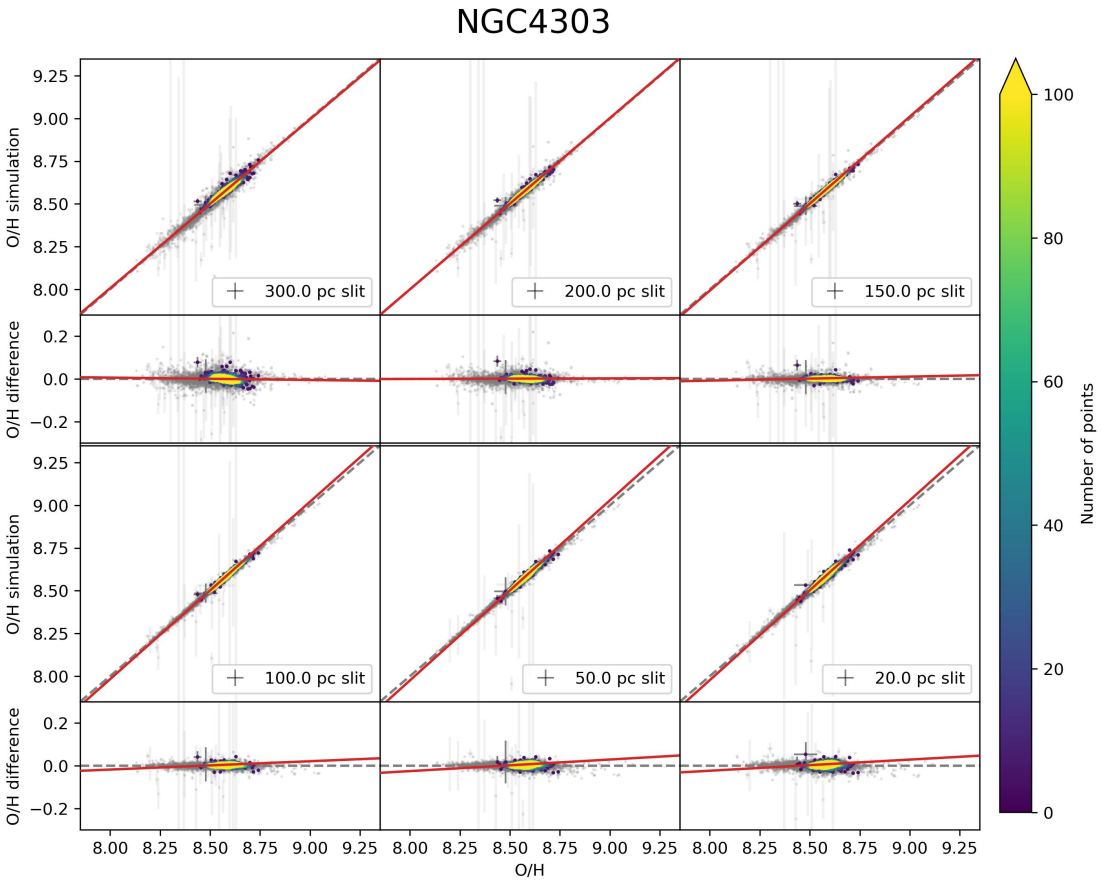

Figure B.28: As Figure 5.6 but for galaxy NGC4303. The sample includes 1011 objects out of the 10,993 total. The full sample of data is plotted in gray for comparison. The red line is the linear fit of the sample (the coefficients are reported in Table B.28).

Table B.29: Coefficients of the linear fit ($y = Ax+B$) of the sample of data derived from the circular aperture restricted to the galaxy NGC4321, shown in Figure B.29, along with the weighted scattering of the data points with respect to the 1-to-1 diagonal, labelled σ.

Diameters pc	A	B dex	σ dex
300.0	0.969 ± 0.008	0.27 ± 0.07	0.011
200.0	1.062 ± 0.009	−0.53 ± 0.08	0.005
150.0	1.11 ± 0.01	−0.9 ± 0.1	0.007
100.0	1.14 ± 0.01	−1.2 ± 0.1	0.012
50.0	1.14 ± 0.02	−1.2 ± 0.1	0.016
20.0	1.13 ± 0.02	−1.1 ± 0.1	0.018

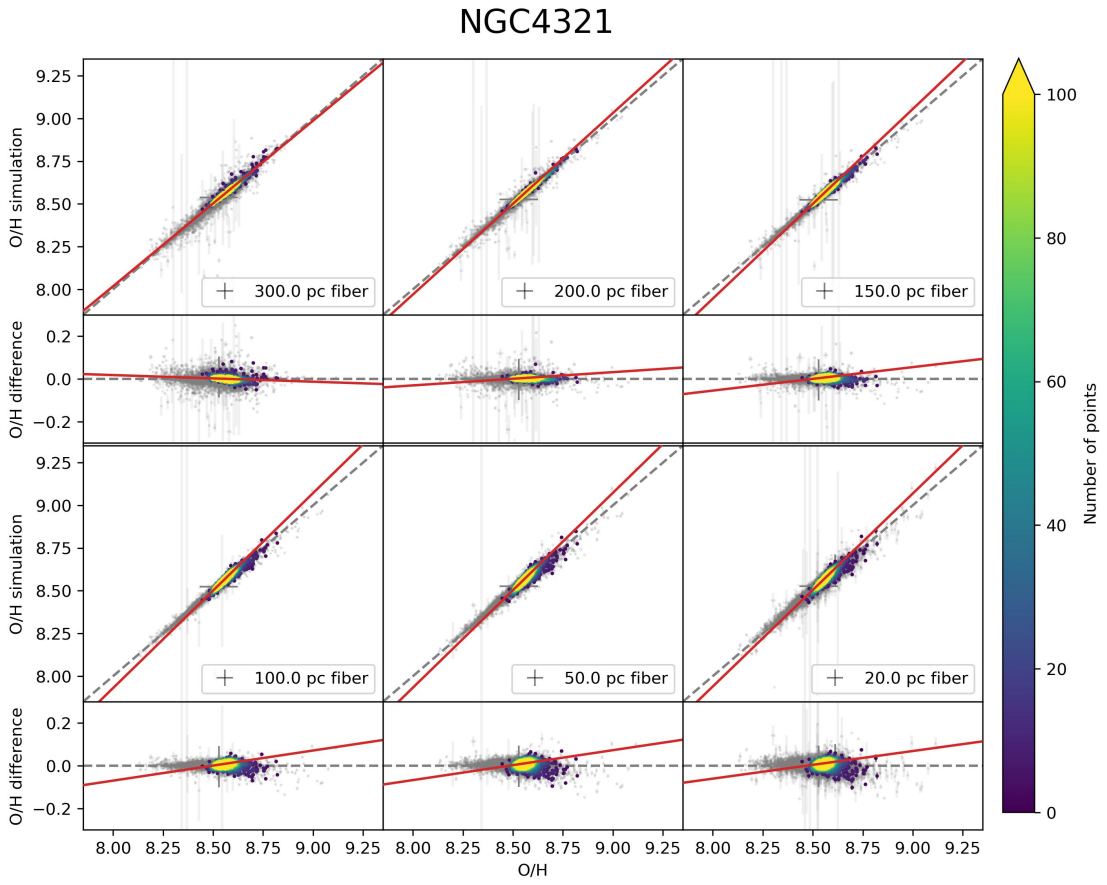

Figure B.29: As Figure 5.5 but for galaxy NGC4321. The sample includes 714 objects out of the 10,993 total. The full sample of data is plotted in gray for comparison. The red line is the linear fit of the sample (the coefficients are reported in Table B.29).

Table B.30: Coefficients of the linear fit ($y = Ax + B$) of the sample of data derived from the rectangular aperture restricted to the galaxy NGC4321, shown in Figure B.30, along with the weighted scattering of the data points with respect to the 1-to-1 diagonal, labelled σ.

Widths pc	A	B dex	σ dex
300.0	0.946 ± 0.007	0.46 ± 0.06	0.011
200.0	0.992 ± 0.005	0.07 ± 0.04	0.006
150.0	1.022 ± 0.006	−0.18 ± 0.05	0.004
100.0	1.048 ± 0.007	−0.41 ± 0.06	0.005
50.0	1.063 ± 0.009	−0.53 ± 0.08	0.008
20.0	1.060 ± 0.009	−0.51 ± 0.08	0.010

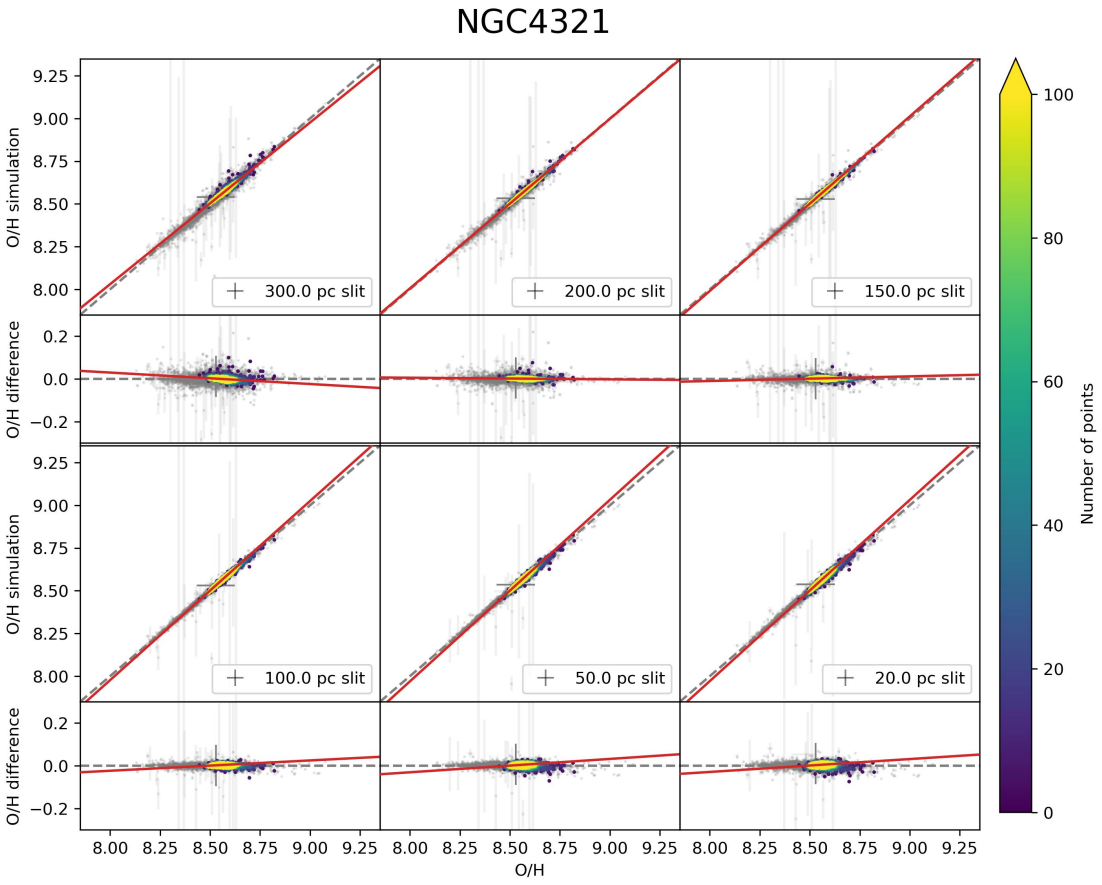

Figure B.30: As Figure 5.6 but for galaxy NGC4321. The sample includes 714 objects out of the 10,993 total. The full sample of data is plotted in gray for comparison. The red line is the linear fit of the sample (the coefficients are reported in Table B.30).

Table B.31: Coefficients of the linear fit ($y = Ax + B$) of the sample of data derived from the circular aperture restricted to the galaxy NGC4535, shown in Figure B.31, along with the weighted scattering of the data points with respect to the 1-to-1 diagonal, labelled σ.

Diameters pc	A	B dex	σ dex
300.0	0.93 ± 0.02	0.6 ± 0.2	0.039
200.0	0.99 ± 0.01	0.1 ± 0.1	0.020
150.0	1.032 ± 0.009	−0.27 ± 0.08	0.010
100.0	1.06 ± 0.01	−0.52 ± 0.09	0.007
50.0	1.07 ± 0.01	−0.6 ± 0.1	0.016
20.0	1.05 ± 0.02	−0.4 ± 0.1	0.020

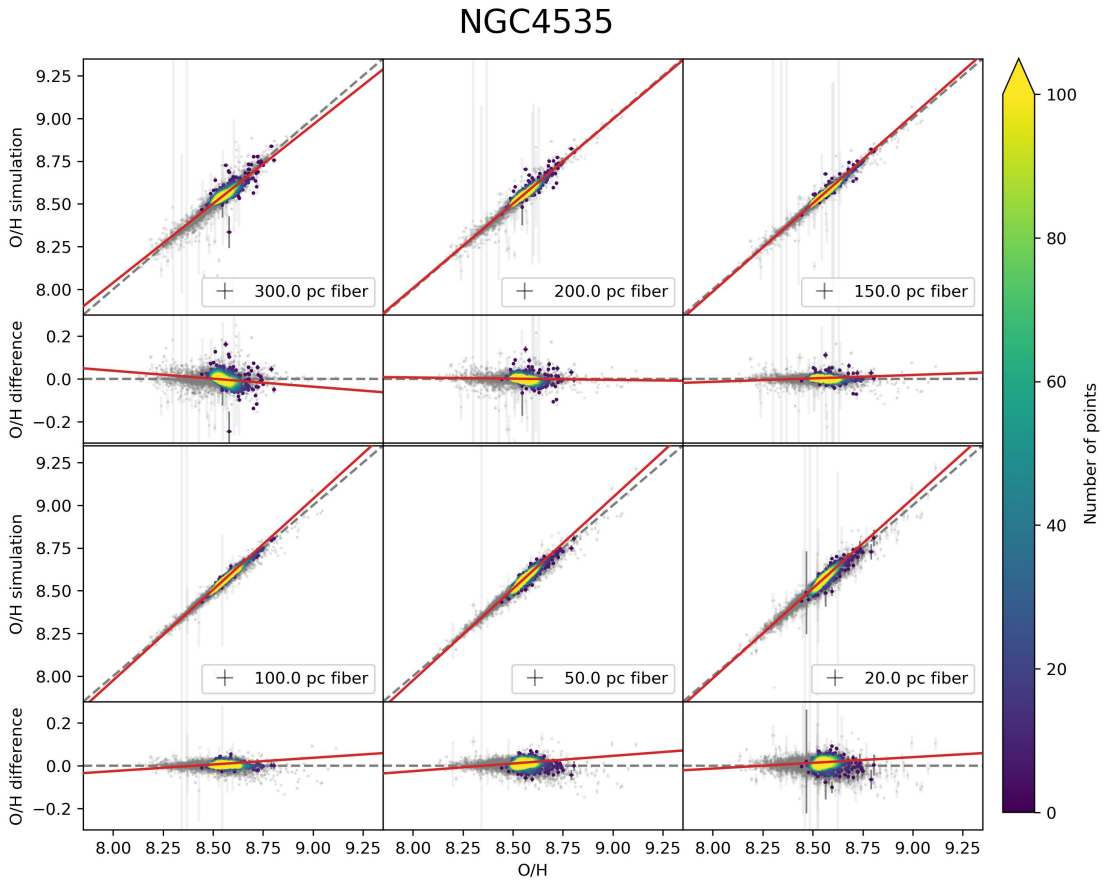

Figure B.31: As Figure 5.5 but for galaxy NGC4535. The sample includes 578 objects out of the 10,993 total. The full sample of data is plotted in gray for comparison. The red line is the linear fit of the sample (the coefficients are reported in Table B.31).

Table B.32: Coefficients of the linear fit ($y = Ax + B$) of the sample of data derived from the rectangular aperture restricted to the galaxy NGC4535, shown in Figure B.32, along with the weighted scattering of the data points with respect to the 1-to-1 diagonal, labelled σ.

Widths pc	A	B dex	σ dex
300.0	0.93 ± 0.01	0.6 ± 0.1	0.020
200.0	0.97 ± 0.01	0.27 ± 0.08	0.014
150.0	0.998 ± 0.007	0.02 ± 0.06	0.009
100.0	1.025 ± 0.005	−0.21 ± 0.05	0.005
50.0	1.043 ± 0.007	−0.36 ± 0.06	0.007
20.0	1.044 ± 0.009	−0.37 ± 0.07	0.010

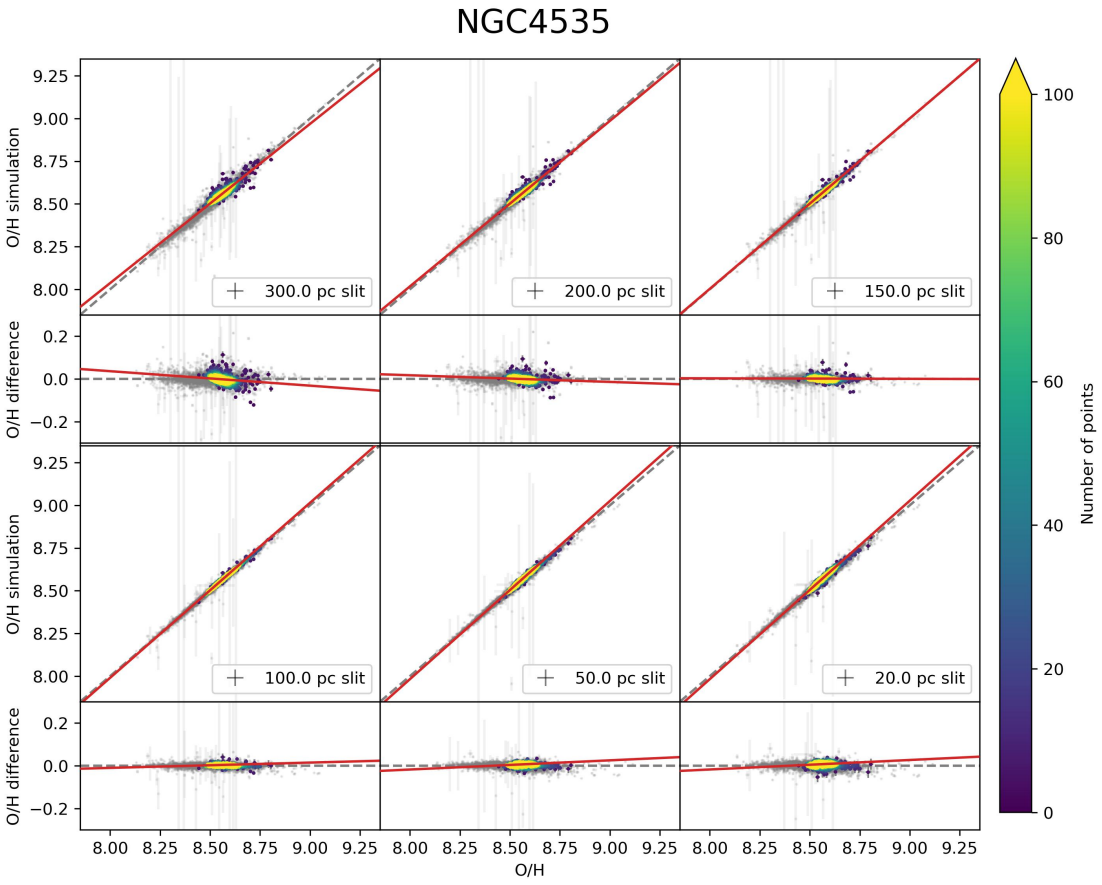

Figure B.32: As Figure 5.6 but for galaxy NGC4535. The sample includes 578 objects out of the 10,993 total. The full sample of data is plotted in gray for comparison. The red line is the linear fit of the sample (the coefficients are reported in Table B.32).

Table B.33: Coefficients of the linear fit ($y = Ax+B$) of the sample of data derived from the circular aperture restricted to the galaxy NGC5068, shown in Figure B.33, along with the weighted scattering of the data points with respect to the 1-to-1 diagonal, labelled σ.

Diameters pc	A	B dex	σ dex
300.0	0.97 ± 0.02	0.3 ± 0.2	0.038
200.0	1.00 ± 0.02	0.0 ± 0.2	0.026
150.0	0.99 ± 0.01	0.1 ± 0.1	0.024
100.0	1.002 ± 0.007	−0.02 ± 0.06	0.011
50.0	1.062 ± 0.007	−0.51 ± 0.06	0.008
20.0	1.17 ± 0.04	−1.4 ± 0.3	0.018

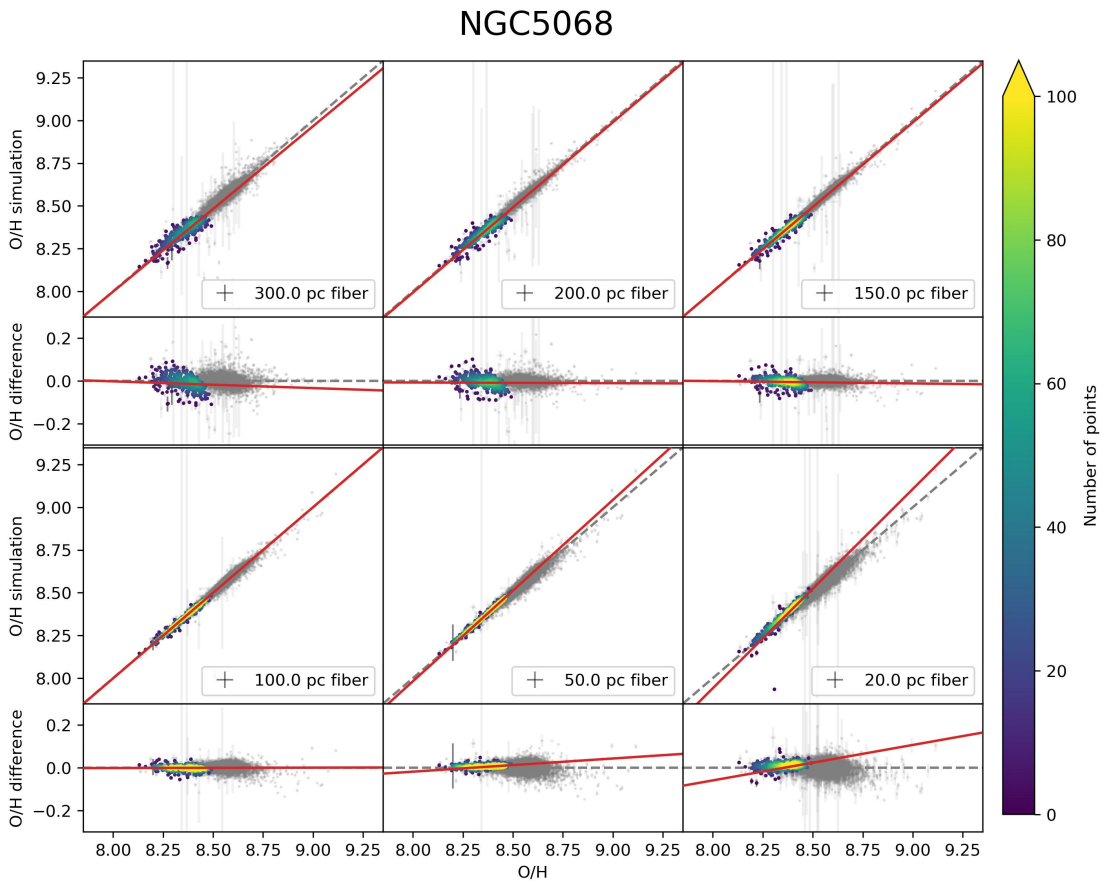

Figure B.33: As Figure 5.5 but for galaxy NGC5068. The sample includes 321 objects out of the 10,993 total. The full sample of data is plotted in gray for comparison. The red line is the linear fit of the sample (the coefficients are reported in Table B.33).

Table B.34: Coefficients of the linear fit ($y = Ax + B$) of the sample of data derived from the rectangular aperture restricted to the galaxy NGC5068, shown in Figure B.34, along with the weighted scattering of the data points with respect to the 1-to-1 diagonal, labelled σ.

Widths pc	A	B dex	σ dex
300.0	0.99 ± 0.02	0.1 ± 0.1	0.030
200.0	0.98 ± 0.01	0.1 ± 0.1	0.020
150.0	0.983 ± 0.009	0.13 ± 0.08	0.018
100.0	0.990 ± 0.005	0.08 ± 0.05	0.013
50.0	1.020 ± 0.004	−0.16 ± 0.03	0.006
20.0	1.028 ± 0.005	−0.23 ± 0.05	0.007

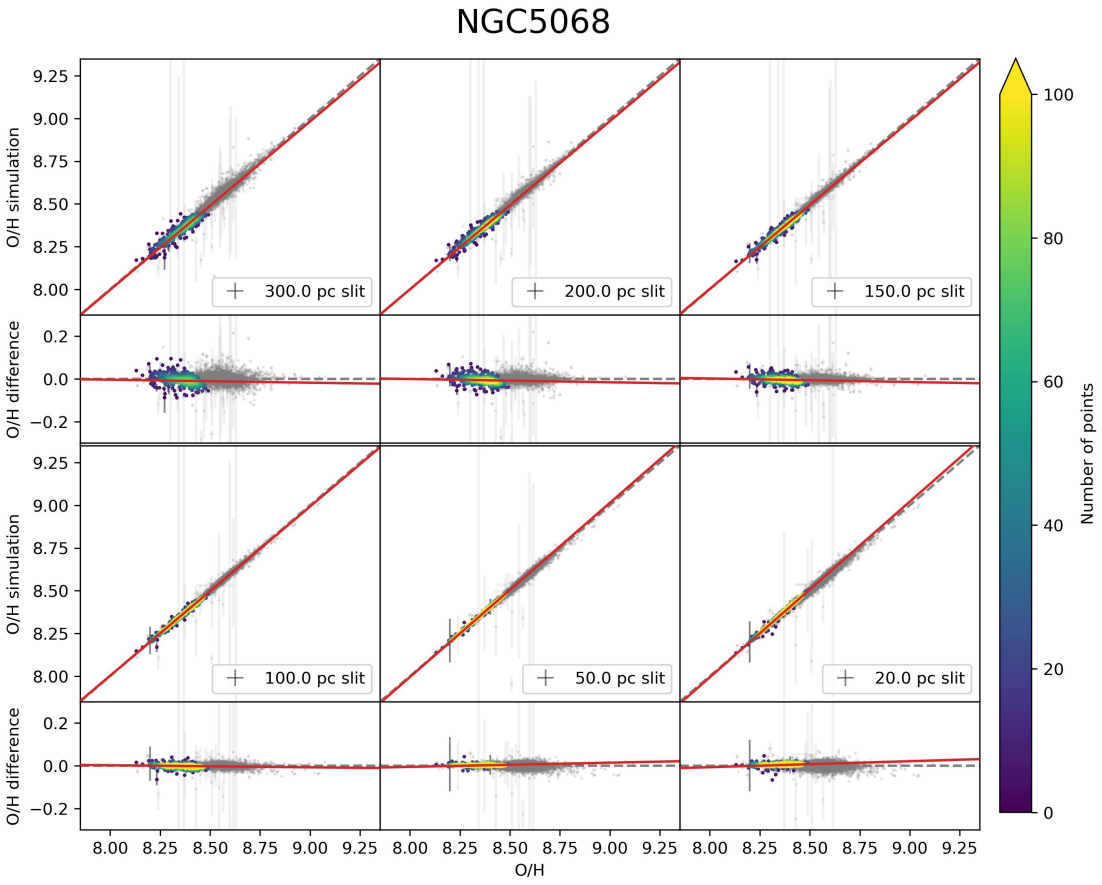

Figure B.34: As Figure 5.6 but for galaxy NGC5068. The sample includes 321 objects out of the 10,993 total. The full sample of data is plotted in gray for comparison. The red line is the linear fit of the sample (the coefficients are reported in Table B.34).

Table B.35: Coefficients of the linear fit ($y = Ax + B$) of the sample of data derived from the circular aperture restricted to the galaxy NGC7496, shown in Figure B.35, along with the weighted scattering of the data points with respect to the 1-to-1 diagonal, labelled σ.

Diameters pc	A	B dex	σ dex
300.0	0.98 ± 0.01	0.20 ± 0.08	0.029
200.0	1.021 ± 0.007	−0.18 ± 0.06	0.028
150.0	1.057 ± 0.008	−0.48 ± 0.07	0.022
100.0	1.09 ± 0.01	−0.76 ± 0.09	0.032
50.0	1.10 ± 0.01	−0.8 ± 0.1	0.013
20.0	1.10 ± 0.01	−0.8 ± 0.1	0.015

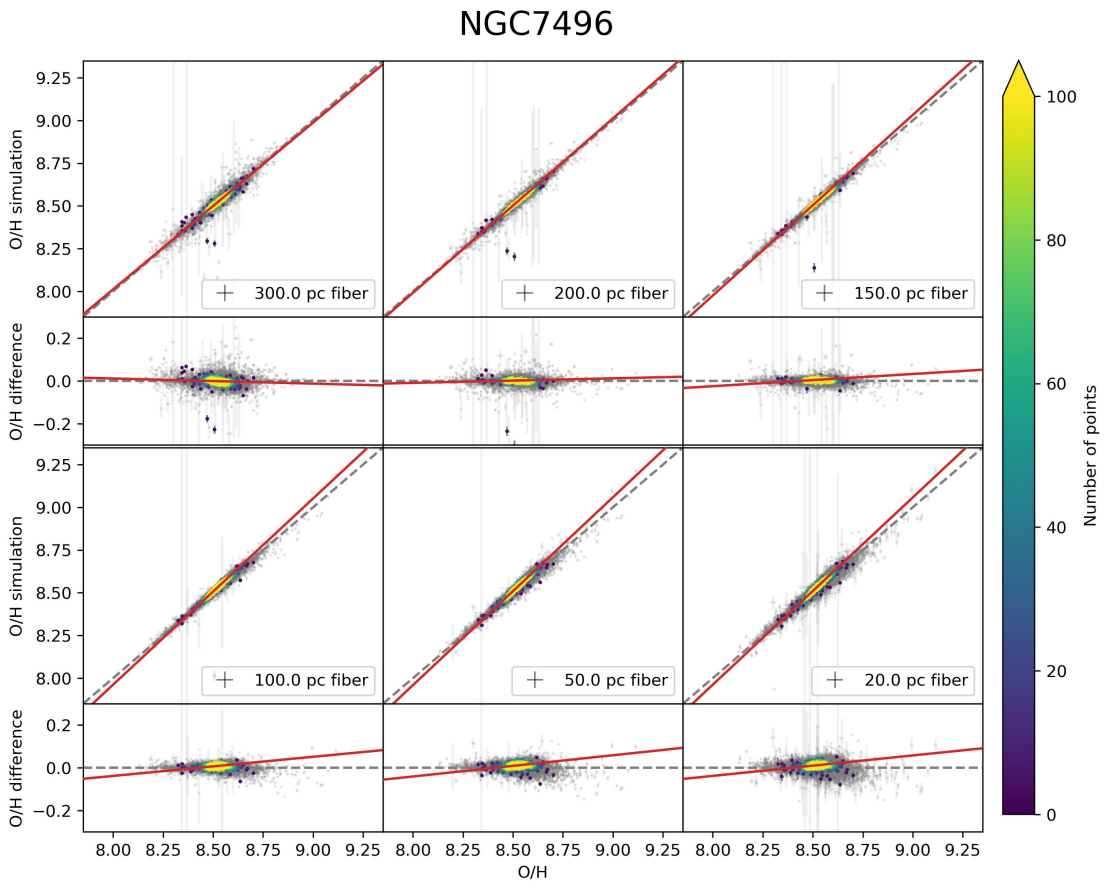

Figure B.35: As Figure 5.5 but for galaxy NGC7496. The sample includes 270 objects out of the 10,993 total. The full sample of data is plotted in gray for comparison. The red line is the linear fit of the sample (the coefficients are reported in Table B.35).

Table B.36: Coefficients of the linear fit ($y = Ax + B$) of the sample of data derived from the rectangular aperture restricted to the galaxy NGC7496, shown in Figure B.36, along with the weighted scattering of the data points with respect to the 1-to-1 diagonal, labelled σ.

Widths pc	A	B dex	σ dex
300.0	0.983 ± 0.009	0.15 ± 0.08	0.023
200.0	0.994 ± 0.005	0.05 ± 0.04	0.021
150.0	1.100 ± 0.005	−0.08 ± 0.04	0.021
100.0	1.028 ± 0.006	−0.23 ± 0.05	0.027
50.0	1.041 ± 0.007	−0.34 ± 0.06	0.038
20.0	1.044 ± 0.008	−0.37 ± 0.07	0.037

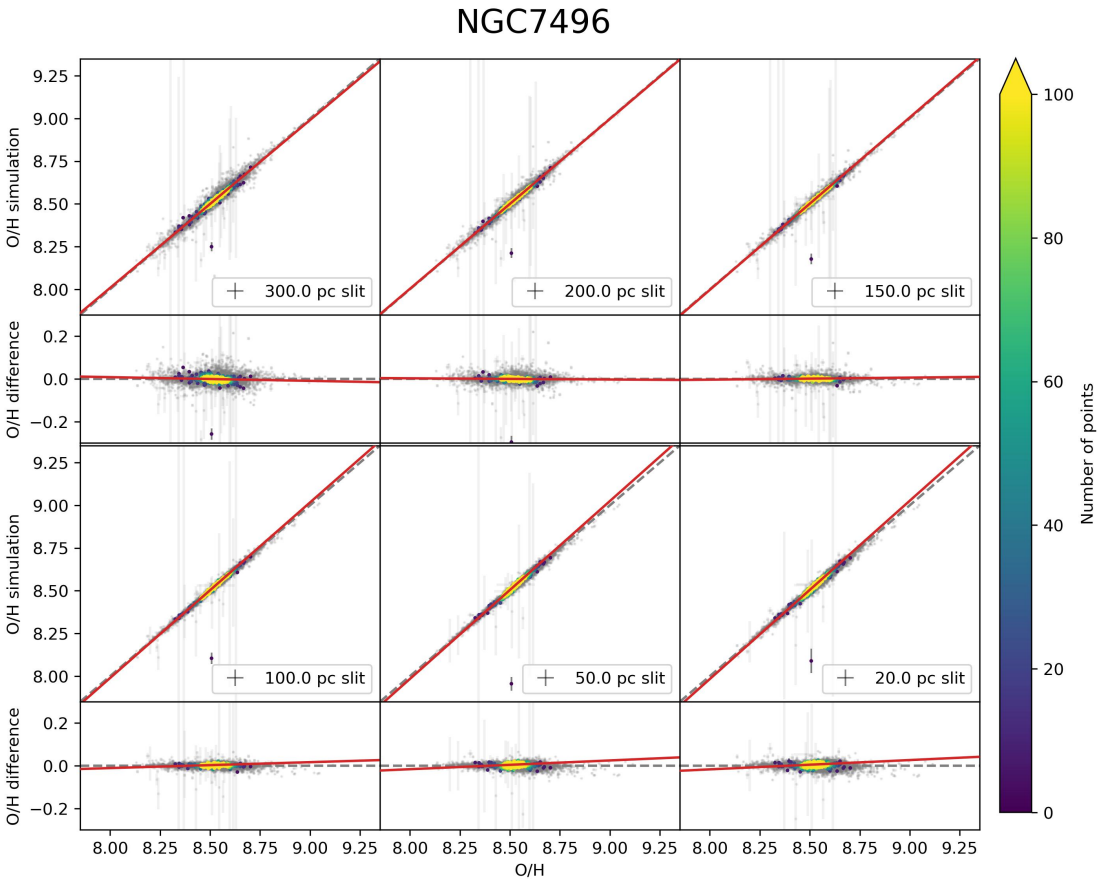

Figure B.36: As Figure 5.6 but for galaxy NGC7496. The sample includes 270 objects out of the 10,993 total. The full sample of data is plotted in gray for comparison. The red line is the linear fit of the sample (the coefficients are reported in Table B.36).

List of Figures

List of Tables

List of Acronyms

ADF Abundance Discrepancy Factor

AGB Asymptotic Giant Branch

AGN Active Galactic Nuclei

CELs "Collisionally Excited Lines"

CMM Cold Molecular Medium

CNM Cold Neutral Medium

DAP Data Analysis Pipeline

DIG diffuse ionezed gas

FIR far infrared

GMCs giant molecular clouds

HIM Hot Ionized Medium

ICFs Ionization Correction Factors

IFS Integral Field Spectroscopy

ISM Interstellar Medium

JWST James Webb Space Telescope

PNe Planetary Nebulae

PSF Point-Spread Function

RLs "Recombination Lines"

S/N Signal-to-Noise

SELs Strong Emission Lines

UV ultraviolet

WFM Wide-Field Mode

WIM Warm Ionized Medium

WNM Warm Neutral Medium

References

Alloin, D., Collin-Souffrin, S., Joly, M., & Vigroux, L. (1979). Nitrogen and oxygen abundances in galaxies., *78*, 200–216.

Amayo, A., Delgado-Inglada, G., & Stasińska, G. (2021). Ionization correction factors and dust depletion patterns in giant H II regions., *505*(2), 2361–2376. https://doi.org/10.1093/mnras/stab1467

Anand, G. S., Lee, J. C., Van Dyk, S. D., Leroy, A. K., Rosolowsky, E., Schinnerer, E., Larson, K., Kourkchi, E., Kreckel, K., Scheuermann, F., Rizzi, L., Thilker, D., Tully, R. B., Bigiel, F., Blanc, G. A., Boquien, M., Chandar, R., Dale, D., Emsellem, E., ... Whitmore, B. (2021). Distances to PHANGS galaxies: New tip of the red giant branch measurements and adopted distances., *501*(3), 3621–3639. https://doi.org/10.1093/mnras/staa3668

Asplund, M., Amarsi, A. M., & Grevesse, N. (2021). The chemical make-up of the Sun: A 2020 vision., *653*, Article A141, A141. https://doi.org/10.1051/0004-6361/202140445

Belfiore, F., Santoro, F., Groves, B., Schinnerer, E., Kreckel, K., Glover, S. C. O., Klessen, R. S., Emsellem, E., Blanc, G. A., Congiu, E., Barnes, A. T., Boquien, M., Chevance, M., Dale, D. A., Kruijssen, J. M. D., Leroy, A. K., Pan, H. .-., Pessa, I., Schruba, A., & Williams, T. G. (2022). A tale of two DIGs: The relative role of H II regions and low-mass hot evolved stars in powering the diffuse ionised gas (DIG) in PHANGS-MUSE galaxies., *659*, Article A26, A26. https://doi.org/10.1051/0004-6361/202141859

Bittner, A., Falcón-Barroso, J., Nedelchev, B., Dorta, A., Gadotti, D. A., Sarzi, M., Molaeinezhad, A., Iodice, E., Rosado-Belza, D., de Lorenzo-Cáceres, A., Fragkoudi, F., Galán-de Anta, P. M., Husemann, B., Méndez-Abreu, J., Neumann, J., Pinna, F., Querejeta, M., Sánchez-Blázquez, P., & Seidel, M. K. (2019). The GIST pipeline: A multi-purpose tool for the analysis

and visualisation of (integral-field) spectroscopic data., *628*, Article A117, A117. https://doi.org/10.1051/0004-6361/201935829

Blanc, G. A., Heiderman, A., Gebhardt, K., Evans, I., Neal J., & Adams, J. (2009). The Spatially Resolved Star Formation Law From Integral Field Spectroscopy: VIRUS-P Observations of NGC 5194., *704*(1), 842–862. https://doi.org/10.1088/0004-637X/704/1/842

Blanc, G. A., Kewley, L., Vogt, F. P. A., & Dopita, M. A. (2015). IZI: Inferring the Gas Phase Metallicity (Z) and Ionization Parameter (q) of Ionized Nebulae Using Bayesian Statistics., *798*(2), Article 99, 99. https://doi.org/10.1088/0004-637X/798/2/99

Bradley, L., Sipőcz, B., Robitaille, T., Tollerud, E., Vinícius, Z., Deil, C., Barbary, K., Wilson, T. J., Busko, I., Donath, A., Günther, H. M., Cara, M., Lim, P. L., Meßlinger, S., Burnett, Z., Conseil, S., Droettboom, M., Bostroem, A., Bray, E. M., . . . Perren, G. (2024, April). *Astropy/photutils: 1.12.0* (Version 1.12.0). Zenodo. https://doi.org/10.5281/zenodo.10967176

Bresolin, F., Gieren, W., Kudritzki, R.-P., Pietrzyński, G., Urbaneja, M. A., & Carraro, G. (2009). Extragalactic Chemical Abundances: Do H II Regions and Young Stars Tell the Same Story? The Case of the Spiral Galaxy NGC 300., *700*(1), 309–330. https://doi.org/10.1088/0004-637X/700/1/309

Cardelli, J. A., Clayton, G. C., & Mathis, J. S. (1989). The Relationship between Infrared, Optical, and Ultraviolet Extinction., *345*, 245. https://doi.org/10.1086/167900

Carilli, C. L., & Walter, F. (2013). Cool Gas in High-Redshift Galaxies., *51*(1), 105–161. https://doi.org/10.1146/annurev-astro-082812-140953

Churchwell, E. (2002). Ultra-Compact HII Regions and Massive Star Formation., *40*, 27–62. https://doi.org/10.1146/annurev.astro.40.060401.093845

Cioni, M. .-. L. (2009). The metallicity gradient as a tracer of history and structure: the Magellanic Clouds and M33 galaxies., *506*(3), 1137–1146. https://doi.org/10.1051/0004-6361/200912138

Congiu, E., Blanc, G. A., Belfiore, F., Santoro, F., Scheuermann, F., Kreckel, K., Emsellem, E., Groves, B., Pan, H.-A., Bigiel, F., Dale, D. A., Glover, S. C. O., Grasha, K., Egorov, O. V., Leroy, A., Schinnerer, E., Watkins, E. J., & Williams, T. G. (2023). PHANGS-MUSE: Detection and Bayesian classification of 40 000 ionised nebulae in nearby spiral galaxies., *672*, Article A148, A148. https://doi.org/10.1051/0004-6361/202245153

Curti, M., D'Eugenio, F., Carniani, S., Maiolino, R., Sandles, L., Witstok, J., Baker, W. M., Bennett, J. S., Piotrowska, J. M., Tacchella, S., Charlot, S., Nakajima, K., Maheson, G., Mannucci, F., Amiri, A., Arribas, S., Belfiore, F., Bonaventura, N. R., Bunker, A. J., ... Wallace, I. E. B. (2023). The chemical enrichment in the early Universe as probed by JWST via direct metallicity measurements at z ∼ 8., *518*(1), 425–438. https://doi.org/10.1093/mnras/stac2737

Curti, M., Maiolino, R., Curtis-Lake, E., Chevallard, J., Carniani, S., D'Eugenio, F., Looser, T. J., Scholtz, J., Charlot, S., Cameron, A., Übler, H., Witstok, J., Boyett, K., Laseter, I., Sandles, L., Arribas, S., Bunker, A., Giardino, G., Maseda, M. V., ... Sun, F. (2024). JADES: Insights into the low-mass end of the mass-metallicity-SFR relation at 3 < z < 10 from deep JWST/NIRSpec spectroscopy., *684*, Article A75, A75. https://doi.org/10.1051/0004-6361/202346698

Dalcanton, J. J. (2007). The Metallicity of Galaxy Disks: Infall versus Outflow., *658*(2), 941–959. https://doi.org/10.1086/508913

Dalcanton, J. J., Yoachim, P., & Bernstein, R. A. (2004). The Formation of Dust Lanes: Implications for Galaxy Evolution., *608*(1), 189–207. https://doi.org/10.1086/386358

Dale, J. E. (2015). The modelling of feedback in star formation simulations., *68*, 1–33. https://doi.org/10.1016/j.newar.2015.06.001

Delgado-Inglada, G., Medina-Amayo, A., & Stasińska, G. (2019). Ionization correction factors for ionized nebulae. *arXiv e-prints*, Article arXiv:1905.01191, arXiv:1905.01191. https://doi.org/10.48550/arXiv.1905.01191

Denicoló, G., Terlevich, R., & Terlevich, E. (2002). New light on the search for low-metallicity galaxies - I. The N2 calibrator., *330*(1), 69–74. https://doi.org/10.1046/j.1365-8711.2002.05041.x

Díaz, A. I., & Pérez-Montero, E. (2000). An empirical calibration of nebular abundances based on the sulphur emission lines., *312*(1), 130–138. https://doi.org/10.1046/j.1365-8711.2000.03117.x

Dopita, M. A., & Evans, I. N. (1986). Theoretical Models for H II Regions. II. The Extragalactic H II Region Abundance Sequence., *307*, 431. https://doi.org/10.1086/164432

Dors, O. L., Pérez-Montero, E., Hägele, G. F., Cardaci, M. V., & Krabbe, A. C. (2016). Sulphur abundance determinations in star-forming regions - I.

Ionization correction factor., *456*(4), 4407–4424. https://doi.org/10.1093/mnras/stv2995

Draine, B. T. (2011). *Physics of the Interstellar and Intergalactic Medium*. Princeton University Press.

Dufour, R. J., Talbot, J., R. J., Jensen, E. B., & Shields, G. A. (1980). M 83 II: spectral characteristics and chemical abundances of HII regions., *236*, 119–134. https://doi.org/10.1086/157725

Edmunds, M. G., & Pagel, B. E. J. (1984). On the composition of H II regions in southern galaxies. III. NGC 2997 and 7793., *211*, 507–519. https://doi.org/10.1093/mnras/211.3.507

Emsellem, E., Schinnerer, E., Santoro, F., Belfiore, F., Pessa, I., McElroy, R., Blanc, G. A., Congiu, E., Groves, B., Ho, I. .-., Kreckel, K., Razza, A., Sanchez-Blazquez, P., Egorov, O., Faesi, C., Klessen, R. S., Leroy, A. K., Meidt, S., Querejeta, M., ... Williams, T. G. (2022). The PHANGS-MUSE survey. Probing the chemo-dynamical evolution of disc galaxies., *659*, Article A191, A191. https://doi.org/10.1051/0004-6361/202141727

Ferrière, K. M. (2001). The interstellar environment of our galaxy. *Reviews of Modern Physics*, *73*(4), 1031–1066. https://doi.org/10.1103/RevModPhys.73.1031

Finlator, K., & Davé, R. (2008). The origin of the galaxy mass-metallicity relation and implications for galactic outflows., *385*(4), 2181–2204. https://doi.org/10.1111/j.1365-2966.2008.12991.x

Garay, G., & Lizano, S. (1999). Massive Stars: Their Environment and Formation., *111*(763), 1049–1087. https://doi.org/10.1086/316416

García-Rojas, J., & Esteban, C. (2007). On the Abundance Discrepancy Problem in H II Regions., *670*(1), 457–470. https://doi.org/10.1086/521871

Goldberg, L., Muller, E. A., & Aller, L. H. (1960). The Abundances of the Elements in the Solar Atmosphere., *5*, 1. https://doi.org/10.1086/190053

Groves, B., Kreckel, K., Santoro, F., Belfiore, F., Zavodnik, E., Congiu, E., Egorov, O. V., Emsellem, E., Grasha, K., Leroy, A., Scheuermann, F., Schinnerer, E., Watkins, E. J., Barnes, A. T., Bigiel, F., Dale, D. A., Glover, S. C. O., Pessa, I., Sanchez-Blazquez, P., & Williams, T. G. (2023). The PHANGS-MUSE nebular catalogue., *520*(4), 4902–4952. https://doi.org/10.1093/mnras/stad114

Gruenwald, R. B., & Viegas, S. M. (1992). Line-of-Sight Results from H II Region Models., *78*, 153. https://doi.org/10.1086/191623

Haffner, L. M., Dettmar, R. .-., Beckman, J. E., Wood, K., Slavin, J. D., Giammanco, C., Madsen, G. J., Zurita, A., & Reynolds, R. J. (2009). The warm ionized medium in spiral galaxies. *Reviews of Modern Physics*, *81*(3), 969–997. https://doi.org/10.1103/RevModPhys.81.969

Haschke, R., Grebel, E. K., Duffau, S., & Jin, S. (2012). Metallicity Distribution Functions of the Old Populations of the Magellanic Clouds from RR Lyrae Stars., *143*(2), Article 48, 48. https://doi.org/10.1088/0004-6256/143/2/48

Herbst, E. (1995). Chemistry in the Interstellar Medium. *Annual Review of Physical Chemistry*, *46*, 27–54. https://doi.org/10.1146/annurev.pc.46.100195.000331

Ho, I. .-., Meidt, S. E., Kudritzki, R.-P., Groves, B. A., Seibert, M., Madore, B. F., Schinnerer, E., Rich, J. A., Kobayashi, C., & Kewley, L. J. (2018). Azimuthal variations of gas-phase oxygen abundance in NGC 2997., *618*, Article A64, A64. https://doi.org/10.1051/0004-6361/201833262

Ho, I. .-., Seibert, M., Meidt, S. E., Kudritzki, R.-P., Kobayashi, C., Groves, B. A., Kewley, L. J., Madore, B. F., Rich, J. A., Schinnerer, E., D'Agostino, J., & Poetrodjojo, H. (2017). The Chemical Evolution Carousel of Spiral Galaxies: Azimuthal Variations of Oxygen Abundance in NGC1365., *846*(1), Article 39, 39. https://doi.org/10.3847/1538-4357/aa8460

Izotov, Y. I., Stasińska, G., Meynet, G., Guseva, N. G., & Thuan, T. X. (2006). The chemical composition of metal-poor emission-line galaxies in the Data Release 3 of the Sloan Digital Sky Survey., *448*(3), 955–970. https://doi.org/10.1051/0004-6361:20053763

Kewley, L. J., & Dopita, M. A. (2002). Using Strong Lines to Estimate Abundances in Extragalactic H II Regions and Starburst Galaxies., *142*(1), 35–52. https://doi.org/10.1086/341326

Kewley, L. J., & Ellison, S. L. (2008). Metallicity Calibrations and the Mass-Metallicity Relation for Star-forming Galaxies., *681*(2), 1183–1204. https://doi.org/10.1086/587500

Kobulnicky, H. A., & Kewley, L. J. (2004). Metallicities of 0.3<z<1.0 Galaxies in the GOODS-North Field., *617*(1), 240–261. https://doi.org/10.1086/425299

Köppen, J., Weidner, C., & Kroupa, P. (2007). A possible origin of the mass-metallicity relation of galaxies., *375*(2), 673–684. https://doi.org/10.1111/j.1365-2966.2006.11328.x

Kreckel, K., Ho, I. .-., Blanc, G. A., Groves, B., Santoro, F., Schinnerer, E., Bigiel, F., Chevance, M., Congiu, E., Emsellem, E., Faesi, C., Glover, S. C. O., Grasha, K., Kruijssen, J. M. D., Lang, P., Leroy, A. K., Meidt, S. E., McElroy, R., Pety, J., ... Schruba, A. (2019). Mapping Metallicity Variations across Nearby Galaxy Disks., *887*(1), Article 80, 80. https://doi.org/10.3847/1538-4357/ab5115

Lang, P., Meidt, S. E., Rosolowsky, E., Nofech, J., Schinnerer, E., Leroy, A. K., Emsellem, E., Pessa, I., Glover, S. C. O., Groves, B., Hughes, A., Kruijssen, J. M. D., Querejeta, M., Schruba, A., Bigiel, F., Blanc, G. A., Chevance, M., Colombo, D., Faesi, C., ... Usero, A. (2020). PHANGS CO Kinematics: Disk Orientations and Rotation Curves at 150 pc Resolution., *897*(2), Article 122, 122. https://doi.org/10.3847/1538-4357/ab9953

Larson, R. B. (1974). Effects of supernovae on the early evolution of galaxies., *169*, 229–246. https://doi.org/10.1093/mnras/169.2.229

Lequeux, J., Peimbert, M., Rayo, J. F., Serrano, A., & Torres-Peimbert, S. (1979). Chemical Composition and Evolution of Irregular and Blue Compact Galaxies., *80*, 155.

Leroy, A. K., Schinnerer, E., Hughes, A., Rosolowsky, E., Pety, J., Schruba, A., Usero, A., Blanc, G. A., Chevance, M., Emsellem, E., Faesi, C. M., Herrera, C. N., Liu, D., Meidt, S. E., Querejeta, M., Saito, T., Sandstrom, K. M., Sun, J., Williams, T. G., ... Whitmore, B. (2021). PHANGS-ALMA: Arcsecond CO(2-1) Imaging of Nearby Star-forming Galaxies., *257*(2), Article 43, 43. https://doi.org/10.3847/1538-4365/ac17f3

Liu, X. .-. (2002, February). Optical Recombination Lines and Temperature Fluctuations. In W. J. Henney, J. Franco, & M. Martos (Eds.), *Revista mexicana de astronomia y astrofisica conference series* (pp. 70–76, Vol. 12).

Liu, X. .-., Storey, P. J., Barlow, M. J., Danziger, I. J., Cohen, M., & Bryce, M. (2000). NGC 6153: a super-metal-rich planetary nebula?, *312*(3), 585–628. https://doi.org/10.1046/j.1365-8711.2000.03167.x

López-Sánchez, Á. R., Dopita, M. A., Kewley, L. J., Zahid, H. J., Nicholls, D. C., & Scharwächter, J. (2012). Eliminating error in the chemical abundance scale for extragalactic H II regions., *426*(4), 2630–2651. https://doi.org/10.1111/j.1365-2966.2012.21145.x

López-Sánchez, Á. R., & Esteban, C. (2010). Massive star formation in Wolf-Rayet galaxies. IV. Colours, chemical-composition analysis and metallicity-luminosity

relations., *517*, Article A85, A85. https://doi.org/10.1051/0004-6361/201014156

Luridiana, V., Morisset, C., & Shaw, R. A. (2015). PyNeb: a new tool for analyzing emission lines. I. Code description and validation of results., *573*, Article A42, A42. https://doi.org/10.1051/0004-6361/201323152

Makarov, D., Prugniel, P., Terekhova, N., Courtois, H., & Vauglin, I. (2014). HyperLEDA. III. The catalogue of extragalactic distances., *570*, Article A13, A13. https://doi.org/10.1051/0004-6361/201423496

Marino, R. A., Rosales-Ortega, F. F., Sánchez, S. F., Gil de Paz, A., Vílchez, J., Miralles-Caballero, D., Kehrig, C., Pérez-Montero, E., Stanishev, V., Iglesias-Páramo, J., Díaz, A. I., Castillo-Morales, A., Kennicutt, R., López-Sánchez, A. R., Galbany, L., García-Benito, R., Mast, D., Mendez-Abreu, J., Monreal-Ibero, A., ... CALIFA Team. (2013). The O3N2 and N2 abundance indicators revisited: improved calibrations based on CALIFA and T_e-based literature data., *559*, Article A114, A114. https://doi.org/10.1051/0004-6361/201321956

Mathis, J. S., & Rosa, M. R. (1991). Ionization correction factors and compositions of HII regions., *245*, 625.

Mathis, J. S., Torres-Peimbert, S., & Peimbert, M. (1998). Temperature and Density Fluctuations in Planetary Nebulae., *495*(1), 328–336. https://doi.org/10.1086/305254

McCall, M. L., Rybski, P. M., & Shields, G. A. (1985). The chemistry of galaxies. I. The nature of giant extragalactic H II regions., *57*, 1–62. https://doi.org/10.1086/190994

McGaugh, S. S. (1991). H II Region Abundances: Model Oxygen Line Ratios., *380*, 140. https://doi.org/10.1086/170569

McKee, C. F., & Ostriker, J. P. (1977). A theory of the interstellar medium: three components regulated by supernova explosions in an inhomogeneous substrate., *218*, 148–169. https://doi.org/10.1086/155667

McKee, C. F., & Ostriker, E. C. (2007). Theory of Star Formation., *45*(1), 565–687. https://doi.org/10.1146/annurev.astro.45.051806.110602

Méndez-Delgado, J. E., Esteban, C., García-Rojas, J., Kreckel, K., & Peimbert, M. (2023a). Temperature inhomogeneities cause the abundance discrepancy in H II regions., *618*(7964), 249–251. https://doi.org/10.1038/s41586-023-05956-2

Méndez-Delgado, J. E., Esteban, C., García-Rojas, J., Kreckel, K., & Peimbert, M. (2023b). Temperature inhomogeneities cause the abundance discrepancy in H II regions., *618*(7964), 249–251. https://doi.org/10.1038/s41586-023-05956-2

Morales-Luis, A. B., Pérez-Montero, E., Sánchez Almeida, J., & Muñoz-Tuñón, C. (2014). On the Use of the Index N2 to Derive the Metallicity in Metal-poor Galaxies., *797*(2), Article 81, 81. https://doi.org/10.1088/0004-637X/797/2/81

Moustakas, J., Kennicutt, J., Robert C., Tremonti, C. A., Dale, D. A., Smith, J.-D. T., & Calzetti, D. (2010). Optical Spectroscopy and Nebular Oxygen Abundances of the Spitzer/SINGS Galaxies., *190*(2), 233–266. https://doi.org/10.1088/0067-0049/190/2/233

Oey, M. S., Meurer, G. R., Yelda, S., Furst, E. J., Caballero-Nieves, S. M., Hanish, D. J., Levesque, E. M., Thilker, D. A., Walth, G. L., Bland-Hawthorn, J., Dopita, M. A., Ferguson, H. C., Heckman, T. M., Doyle, M. T., Drinkwater, M. J., Freeman, K. C., Kennicutt, J., R. C., Kilborn, V. A., Knezek, P. M., ... Zwaan, M. A. (2007). The Survey for Ionization in Neutral Gas Galaxies. III. Diffuse, Warm Ionized Medium and Escape of Ionizing Radiation., *661*(2), 801–814. https://doi.org/10.1086/517867

Osterbrock, D. E., & Ferland, G. J. (2006). *Astrophysics of gaseous nebulae and active galactic nuclei*. University Science Books.

Pagel, B. E. J., Edmunds, M. G., Blackwell, D. E., Chun, M. S., & Smith, G. (1979). On the composition of H II regions in southern galaxies - I. NGC 300 and 1365., *189*, 95–113. https://doi.org/10.1093/mnras/189.1.95

Peimbert, M., & Costero, R. (1969). Chemical Abundances in Galactic HII Regions. *Boletin de los Observatorios Tonantzintla y Tacubaya*, *5*, 3–22.

Peimbert, M. (1967). Temperature Determinations of H II Regions., *150*, 825. https://doi.org/10.1086/149385

Péquignot, D., Amara, M., Liu, X. .-., Barlow, M. J., Storey, P. J., Morisset, C., Torres-Peimbert, S., & Peimbert, M. (2002, February). Photoionization Models for Planetary Nebulae with Inhomogeneous Chemical Composition. In W. J. Henney, J. Franco, & M. Martos (Eds.), *Revista mexicana de astronomia y astrofisica conference series* (pp. 142–143, Vol. 12).

Peters, T., Banerjee, R., Klessen, R. S., Mac Low, M.-M., Galván-Madrid, R., & Keto, E. R. (2010). H II Regions: Witnesses to Massive Star Formation., *711*(2), 1017–1028. https://doi.org/10.1088/0004-637X/711/2/1017

Pettini, M., & Pagel, B. E. J. (2004). [OIII]/[NII] as an abundance indicator at high redshift., *348*(3), L59–L63. https://doi.org/10.1111/j.1365-2966.2004.07591.x

Pilyugin, L. S. (2000). On the oxygen abundance determination in H bt II regions. The problem of the line intensities - oxygen abundance calibration., *362*, 325–332. https://doi.org/10.48550/arXiv.astro-ph/0004032

Pilyugin, L. S. (2001). On the oxygen abundance determination in HII regions. High-metallicity regions., *369*, 594–604. https://doi.org/10.1051/0004-6361:20010079

Pilyugin, L. S., & Grebel, E. K. (2016). New calibrations for abundance determinations in H II regions., *457*(4), 3678–3692. https://doi.org/10.1093/mnras/stw238

Pilyugin, L. S., Grebel, E. K., & Kniazev, A. Y. (2014). The Abundance Properties of Nearby Late-type Galaxies. I. The Data., *147*(6), Article 131, 131. https://doi.org/10.1088/0004-6256/147/6/131

Pilyugin, L. S., Grebel, E. K., & Mattsson, L. (2012). 'Counterpart' method for abundance determinations in H II regions., *424*(3), 2316–2329. https://doi.org/10.1111/j.1365-2966.2012.21398.x

Pilyugin, L. S., Grebel, E. K., & Zinchenko, I. A. (2015). On the radial abundance gradients in discs of irregular galaxies., *450*(3), 3254–3263. https://doi.org/10.1093/mnras/stv932

Pilyugin, L. S., & Mattsson, L. (2011). Abundance determination in H II regions from spectra without the [O II]λ3727+λ3729 line., *412*(2), 1145–1150. https://doi.org/10.1111/j.1365-2966.2010.17970.x

Pilyugin, L. S., Vílchez, J. M., & Contini, T. (2004). Oxygen and nitrogen abundances in nearby galaxies. Correlations between oxygen abundance and macroscopic properties., *425*, 849–869. https://doi.org/10.1051/0004-6361:20034522

Pilyugin, L. S., & Thuan, T. X. (2005). Oxygen Abundance Determination in H II Regions: The Strong Line Intensities-Abundance Calibration Revisited., *631*(1), 231–243. https://doi.org/10.1086/432408

Sánchez-Menguiano, L., Sánchez, S. F., Kawata, D., Chemin, L., Pérez, I., Ruiz-Lara, T., Sánchez-Blázquez, P., Galbany, L., Anderson, J. P., Grand, R. J. J., Minchev, I., & Gómez, F. A. (2016). Evidence of Ongoing Radial Migration in NGC 6754: Azimuthal Variations of the Gas Properties., *830*(2), Article L40, L40. https://doi.org/10.3847/2041-8205/830/2/L40

Searle, L. (1971). Evidence for Composition Gradients across the Disks of Spiral Galaxies., *168*, 327. https://doi.org/10.1086/151090

Shields, G. A., & Searle, L. (1978). The composition gradient across M101., *222*, 821–832. https://doi.org/10.1086/156201

Spitzer, L. (1978). *Physical processes in the interstellar medium*. A Wiley-Interscience Publication, New York: Wiley. https://doi.org/10.1002/9783527617722

Stasińska, G. (2006). [Ar III]/[O III] and [S III]/[O III]: well-behaved oxygen abundance indicators for HII regions and star forming galaxies., *454*(3), L127–L130. https://doi.org/10.1051/0004-6361:20065516

Stasińska, G. (1998, January). How Reliable Are Abundances from Nebular Spectra? In D. Friedli, M. Edmunds, C. Robert, & L. Drissen (Eds.), *Abundance profiles: Diagnostic tools for galaxy history* (p. 142, Vol. 147).

Stasińska, G. (2004, January). Abundance determinations in H II regions and planetary nebulae. In C. Esteban, R. García López, A. Herrero, & F. Sánchez (Eds.), *Cosmochemistry. the melting pot of the elements* (pp. 115–170).

Thilker, D. A., Walterbos, R. A. M., Braun, R., & Hoopes, C. G. (2002). H II Regions and Diffuse Ionized Gas in 11 Nearby Spiral Galaxies., *124*(6), 3118–3134. https://doi.org/10.1086/344303

Tremonti, C. A., Heckman, T. M., Kauffmann, G., Brinchmann, J., Charlot, S., White, S. D. M., Seibert, M., Peng, E. W., Schlegel, D. J., Uomoto, A., Fukugita, M., & Brinkmann, J. (2004). The Origin of the Mass-Metallicity Relation: Insights from 53,000 Star-forming Galaxies in the Sloan Digital Sky Survey., *613*(2), 898–913. https://doi.org/10.1086/423264

Véron-Cetty, M. .-., & Véron, P. (2010). A catalogue of quasars and active nuclei: 13th edition., *518*, Article A10, A10. https://doi.org/10.1051/0004-6361/201014188

Vilchez, J. M., & Esteban, C. (1996). The chemical composition of HII regions in the outer Galaxy., *280*(3), 720–734. https://doi.org/10.1093/mnras/280.3.720

Vogt, F. P. A., Pérez, E., Dopita, M. A., Verdes-Montenegro, L., & Borthakur, S. (2017). Evidence for azimuthal variations of the oxygen-abundance gradient tracing the spiral structure of the galaxy HCG 91c., *601*, Article A61, A61. https://doi.org/10.1051/0004-6361/201629853

Weilbacher, P. M., Palsa, R., Streicher, O., Bacon, R., Urrutia, T., Wisotzki, L., Conseil, S., Husemann, B., Jarno, A., Kelz, A., Pécontal-Rousset, A., Richard, J.,

Roth, M. M., Selman, F., & Vernet, J. (2020). The data processing pipeline for the MUSE instrument., *641*, Article A28, A28. https://doi.org/10.1051/0004-6361/202037855

Williams, J. P., de Geus, E. J., & Blitz, L. (1994). Determining Structure in Molecular Clouds., *428*, 693. https://doi.org/10.1086/174279

Zahid, H. J., Dima, G. I., Kudritzki, R.-P., Kewley, L. J., Geller, M. J., Hwang, H. S., Silverman, J. D., & Kashino, D. (2014). The Universal Relation of Galactic Chemical Evolution: The Origin of the Mass-Metallicity Relation., *791*(2), Article 130, 130. https://doi.org/10.1088/0004-637X/791/2/130

Zinchenko, I. A., Pilyugin, L. S., Grebel, E. K., Sánchez, S. F., & Vílchez, J. M. (2016). Oxygen abundance maps of CALIFA galaxies., *462*(3), 2715–2733. https://doi.org/10.1093/mnras/stw1857

Zurita, A., Florido, E., Bresolin, F., Pérez-Montero, E., & Pérez, I. (2021). Bar effect on gas-phase abundance gradients. I. Data sample and chemical abundances., *500*(2), 2359–2379. https://doi.org/10.1093/mnras/staa2246